Exploring Lipid Droplet Dynamics and Heterogeneity Through Functional Genomic Screening

By

Alyssa Mathiowetz

A dissertation submitted in partial satisfaction of the

requirements for the degree of

Doctor of Philosophy

in

Metabolic Biology

in the

Graduate Division

of the

University of California, Berkeley

Committee in charge:

Professor James Olzmann, Chair
Professor Elçin Ünal
Professor Denis Titov
Professor Anders Näär

Summer 2024

Abstract

Exploring Lipid Droplet Dynamics and Heterogeneity
Through Functional Genomic Screening

by

Alyssa Mathiowetz

Doctor of Philosophy in Metabolic Biology

University of California, Berkeley

Professor James Olzmann, Chair

Lipid droplets (LDs) are endoplasmic reticulum-derived neutral lipid storage organelles that consist of a core of neutral lipids bounded by a phospholipid monolayer decorated with associated proteins. The canonical role of LDs is to function as a lipid storage depot, and the accumulation of enlarged LDs is the pathological hallmark of numerous prevalent metabolic diseases, such as obesity and metabolic dysfunction-associated steatotic liver disease (MASLD). Recent findings also implicate LDs in a growing number of surprising cellular roles such as preventing lipotoxicity in neurons, increasing the bioactivation of hydrophobic drugs, and suppressing bacterial invasion as part of a protective innate immune response. Despite these important cellular functions, many details surrounding LD biogenesis and breakdown are incompletely understood. Furthermore, while it is appreciated that the regulation and function of LDs must drastically change under starvation, overnutrition, inflammation, and other altered environments, the pathways that govern these responses remain mostly unexplored.

To address this gap in knowledge, we performed a series of CRISPR-Cas9 screens under different metabolic states to uncover mechanisms of hepatic neutral lipid flux. Clustering of chemical-genetic interactions identified CLIC-like chloride channel 1 (CLCC1) as a critical regulator of neutral lipid storage and secretion. Loss of CLCC1 resulted in the buildup of large LDs in hepatoma cells and knockout in mice caused liver steatosis. Remarkably, the LDs are in the lumen of the ER and exhibit properties of lipoproteins, indicating a profound shift in neutral lipid flux. Finally, remote homology searches identified a domain in CLCC1 that is homologous to yeast Brl1p and Brr6p, factors that promote the fusion of the inner and outer nuclear envelopes during nuclear pore complex assembly. Loss of CLCC1 lead to extensive nuclear membrane herniations, consistent with impaired nuclear pore complex assembly. Thus, we identify CLCC1 as the human Brl1p/Brr6p homolog and propose that CLCC1-mediated membrane remodeling promotes hepatic neutral lipid flux and nuclear pore complex assembly.

One of the other novel genes from these screens is the interleukin IL32, a secreted pro-inflammatory cytokine that the Olzmann Lab unexpectedly identified as an LD protein

using proximity labeling proteomics. Our data demonstrate that endogenous IL32 localizes to a subset of LDs following the induction of host defense signaling pathways, suggesting that IL32 may be a key host factor that acts to regulate LDs during an immune response. These findings not only lay a groundwork for elucidating the IL32-mediated mechanisms of LD-bacteria interactions, creating a foundation for an understanding of how targeting lipid storage can be exploited to halt infectious disease pathogenesis, but also highlight the importance of LD heterogeneity in a variety of cellular functions. Together, these studies provide an extensive compendium of lipid storage modulators and provide rich mechanistic insights into lipid droplet flux and LD heterogeneity in the liver.

Dedication and Acknowledgments

It's bittersweet, to look back at graduate school and see not just the moments in lab but the moments in life. The past six years have been marked by early mornings—to run a Western blot, to drive four hours to Tahoe—and late nights—to finish sorting cells, to watch a scary movie or paint or talk. There were many days where took a nap upright at my desk, sometimes because of stress but many times because of fun, enjoying friendships and the richness of life in Berkeley. So the people are what have made my experience special, not one of whom is out of place in this story.

The Olzmann Lab has been unequivocally the best environment I could ask for in graduate school, which I credit to the kind-hearted leadership of James. Both as a professional mentor and "vacation James" (think baseball cap and flip-flops), you have pushed forward and held back when you needed, guiding a project and a scientist to their full potential. I am forever grateful to my lab, too, for the long conversations in Morgan Hall and Li Ka Shing, talking about our projects or the universe or the state of our welfare system or backpacking trips. I cannot thank Cody, Mel, Z, Joe, Clark, Mike, Kirandeep, Sean, Amalia, Alex, Abby, Gergey, Emily, Syd, Irene, Stephany, Emily, Anna, Collin, Barbara, and Rene enough.

One of my favorite moments during my PhD was our 90s-themed "NST Prom", which included chintzy posters tacked up around the Morgan Lounge, cheese puffs, and glitter stickers. Our department is full of wonderful people who encourage when things are good and support when things are tough, who laugh and barbecue and go on adventures. I am thankful for Megan, Nick, Amandine, Cassie, Naveed, Edna, Pete, Kevin, Sophia, Leo, Viana, Lulu, Annie, Jinse, and Alec. And thank you to the community in Li Ka Shing, our second home, for happy hours and sharing ideas and resources: Jordan, Regina, Abrar, Chris, Ellie, Laura, Hannah, and Zhi.

This work would not be nearly where it is today without the help of incredible faculty and staff not just at UC Berkeley but around the world. These people have taken time out of their busy schedules to provide enormous amounts of guidance. They are people I strive to be like. To Ana and Güneş, thank you for always opening the door when I run to your lab, for readily giving advice. To Saswata, Yingjiang, Danielle, Reena, Misun, Denise, and David, I am grateful for your quick responses to email and long conversations at the bench. And to my thesis committee and the wonderful lipid droplet community, thank you.

And this research is only a counterpart to my desire to see communities thrive, to deepen our understanding of nutrition and metabolism from a scientific standpoint in order to impact people and choices. Mount Tamalpais College, the Science Policy Group, and Science for Africa have made radical differences in how I interact with the Bay Area and global communities, and for that, I thank you.

My roommates asked me once what my creative outlet is, what overflows from my heart. Biology can do that, it is exciting and artistic, inherently full of *life*. And *full of life* is what I have felt for so long: road trips, snowboarding, hiking, weddings, marathons, trips to India,

trips to Europe, cooking, singing on couches or in hammocks or in hot tubs. My roommates Lauren, Rebekah, Emily, Marissa, Nick, and Shyam have danced late into the night, gardened, and cooked meals together. And my friends Emma, Dara, Julie, Susie, Kaleigh, and Shikha have called or gone on walks and laughed and prayed and cried. To Solano Church, too, where I have friendships that will last a lifetime—we have all experienced something beautiful and creative together, and I love you all.

Finally, the people who have been there for me the most are of course the ones I grew up with in Connecticut, Massachusetts, California, and Minnesota. It's hard to put into words what you mean to me. Thank you for supporting me and loving me unconditionally. I'm thankful to Mom, Dad, Bri, Kayla, Cody, Pepper, Figgy, Grandma Betty, Barb, Dave, Jim, Mike, Cait, Kristy, Jesse, Nate, McKenna, Zach, John, Sonja, Camille, Grandma Aleda, Denise, Brad, Sharyn, Josh, Sam, and Jess.

This dissertation is dedicated to all of you.

Table of Contents

List of Figures

Chapter 1: Lipid droplets and cellular lipid flux

Contents in this chapter are modified from the previously published review article:

Mathiowetz, A. J. & Olzmann, J. A. Lipid droplets and cellular lipid flux. *Nat. Cell Biol.* 26, 331–345 (2024).

1.1 Introduction

Lipid droplets (LDs) are neutral lipid-filled, endoplasmic reticulum (ER)-derived organelles bound by a single phospholipid monolayer[1,2]. Although the interior of the LD is devoid of proteins, integral and peripheral proteins associate with the LD phospholipid monolayer and regulate activities such as integration of nutrient signaling cascades, contacts with other organelles, synthesis and breakdown of stored lipids, and LD transport[1,2].

LDs regulate the flux of lipids to and from other organelles to meet cellular demands for energy and the synthesis of membrane and signaling lipids derived from fatty acid (FA) precursors[1,2]. Because excess free FAs can act as membrane detergents or cause organelle dysfunction, LDs act as a critical lipid buffering system by sequestering potentially toxic lipids[1]. As a cellular hub of lipid metabolism, LDs maintain contact with many organelles, facilitating lipid transfer[1]. Nearly every eukaryotic cell type can synthesize LDs, reflecting their conserved role in maintaining cellular lipid homeostasis. LDs have been implicated in a range of metabolic diseases associated with altered lipid metabolism, and targeting LD formation or breakdown has been proposed as a therapeutic strategy[3]. LDs have also been connected to the pathogenesis of cancer[4], degenerative diseases (such as neurodegeneration)[5], host–pathogen interactions[6], and cellular stress responses and health/life span[7,8].

Here, we provide a critical review of the mechanisms of LD biogenesis and turnover, lipid composition and dynamics within LDs, lipid transfer between LDs and other organelles, and LDs in regulating membrane lipid damage and cell death.

1.2 Lipid droplet biogenesis

1.2.1 Neutral lipid synthesis at the endoplasmic reticulum

The LD core is composed primarily of neutral lipids such as triacylglycerols (TAGs) and steryl esters (SEs), and possibly other hydrophobic molecules such as acylceramides, squalene, waxes, and fat-soluble drugs and vitamins[9]. The lipid composition of LDs differs depending on the cell type and metabolic demands. A high ratio of SE to TAG can result in SE phase transitions into smectic liquid crystalline phases, potentially having important consequences for LD metabolism[10–13] (Figure 1-1A). Nearly all lipids are synthesized in the ER, including neutral lipids, phospholipids, sterols and sphingolipids. Phospholipids and TAG are synthesized via the Kennedy pathway[2] (Figure 1-2A). The acyl CoA:diacylglycerol acyltransferase (DGAT) enzymes, DGAT1 and DGAT2, mediate the final and rate-limiting esterification reaction at the *sn*-3 position to generate TAG, which is deposited into the hydrophobic phase of the ER bilayer[2]. Although recent structures have provided important insights into the mechanism of DGAT1[14,15]. the mechanism of DGAT2 is less well understood[2]. We lack a complete understanding of how either enzyme accesses diacylglycerol (DAG) and deposits TAG in the membrane[2].

An alternative pathway for the synthesis of TAG from DAG was recently discovered and involves the acyltransferase DGAT1/2-independent enzyme synthesizing storage lipids (DIESL, also known as TMEM68)[16]. DIESL is a multi-pass transmembrane ER protein.

Its activity is suppressed by TMX1, and loss of TMX1 leads to increased TAG synthesis, potentially by employing a phospholipid as an acyl donor[16]. During nutrient deprivation, DIESL has an important role in the generation of TAG, providing a supply of FAs for mitochondrial breakdown at the expense of membrane phospholipids[16]. The emerging data suggest unique roles for DGATs and DIESL in TAG synthesis from distinct pools of FAs, but their interplay under different metabolic conditions or across cell types is unclear.

1.2.2 Lipid phase separation and lipid droplet biogenesis

At low concentrations, neutral lipids deposited into the ER freely diffuse between the phospholipid acyl chains within the hydrophobic phase of the ER membrane[17]. Above a critical concentration, neutral lipids in a membrane will spontaneously phase separate in vitro, demixing from the surrounding phospholipids and coalescing into a neutral lipid lens[17] (Figure 1-2A) Although lipid lens formation can be driven solely by high concentrations of neutral lipids, in cells this early step in LD biogenesis is regulated by homo-oligomers of the conserved ER-resident integral membrane protein seipin and its interacting partners[18] (Figure 1-2A) Loss of seipin does not eliminate LD biogenesis, but instead results in dysregulated LD biogenesis and growth (for example, supersized LDs)[19,20]. Seipin marks sites of LD biogenesis and each cytoplasmic LD is generally associated with at least one seipin focus[19,20]; whether this is always the case, such as in cell types with low expression of seipin, is unknown.

Recent seipin structures[21–24] and molecular dynamics simulations[25–27] provide exceptional insights into the mechanism of seipin in LD biogenesis (Figure 1-2A-C). In the emerging model[18], interactions of TAG with hydrophobic transmembrane segments and the hydrophobic helix within the cage-like seipin oligomeric ring complex promote TAG aggregation and phase separation at low TAG concentrations[25–27] facilitating the formation of neutral lipid lenses at defined sites and preventing spontaneous coalescence at random sites throughout the ER. The neutral lipid lens grows due to Ostwald ripening, a process that can be observed in vitro in droplet-embedded vesicles[20]. The flexibility of the seipin transmembrane domains allows it to adopt an open conformation that favors LD emergence from the cytosolic leaflet of the ER[23,24]. The embedded lumenal domain of seipin may anchor it to the site of LD biogenesis while cytosolic terminal amphipathic helices of seipin associate with the emerging LD. The putative dynamics of the seipin structure and the role of seipin's various domains (that is, the transmembrane regions, lumenal region, and cytosolic amphipathic helices) remain incompletely understood. In addition to the actions of seipin, asymmetric membrane surface tension and phospholipid composition may also contribute to the directional emergence of LDs[1,28,29]. ER scramblases[30–34] and phospholipid synthesis[28,29] impact LD biogenesis, potentially acting to maintain a sufficient amount of phospholipids in the outer leaflet of the ER for LD cytosolic emergence.

The actions of seipin are supported by interacting proteins, such as LDAF1 (also known as promethin)[35,36]. LDAF1 increases the association of seipin with TAG, promotes membrane bending in an LDAF1–seipin complex, and has a key role in determining the site and efficiency of LD biogenesis[35,36]. High-resolution structures of seipin complexes containing LDAF1 remain to be resolved. LDAF1 transfers from the ER to LDs during LD

maturation, whereas seipin remains ER-anchored during LD growth, indicating that there are conformational changes in the LDAF1–seipin complex that remain to be understood[18,35,36]. MCTP1 and MCTP2 also function in concert with seipin during LD biogenesis[37,38]. Interestingly, the reticulon domain of the yeast orthologue of MCTP1/2 (that is, PEX30) not only is required for its localization to ER tubules and promotion of ER tubule formation, but also its role in LD biogenesis[39]. Indeed, highly curved membranes in ER tubules lower the energy barrier for neutral lipid phase separation, and seipin localizes preferentially to curved membranes[40].

Although the majority of LD research has focused on the biogenesis of TAG-rich LDs, yeast seipin also regulates the formation of SE-rich LDs[10,41]. However, some LDs form irrespective of seipin and other known protein regulators, such as LDs made purely of retinyl esters in hepatic stellate cells and engineered yeast[42] and nuclear LDs in hepatocytes[43]. Although seipin may not directly promote SE phase separation, the ability of seipin to cluster TAG indirectly promotes SE nucleation and flux into LDs in cells[10].

1.2.3 Liquid crystalline phase transitions and lipid heterogeneity within lipid droplets

The core of LDs is generally an amorphous mixture of neutral lipids present as a disordered liquid phase. Under certain metabolic conditions, the interior neutral lipids are structurally reorganized due to the inherent property of SEs to undergo phase transitions into smectic liquid crystalline phases at high concentrations[10,11,12] (Figure 1-1A), which can be visualized by electron microscopy as onion-like layers underneath the LD phospholipid monolayer and by polarized light microscopy due to the distinctive light emission in the shape of a Maltese cross[10–12]. High concentrations of SEs favor demixing from TAGs and liquid crystalline phase transitions, yet how and when SE liquid crystalline phase transitions occur in cells is mostly unknown. The SE:TAG ratio is influenced by the metabolic state of the cell and LD metabolism can drive SE phase transitions. For example, a higher SE:TAG ratio driven by TAG lipolysis leads to SE liquid crystalline phase transition in cells under mitotic arrest and during nutrient starvation[10–12]. The concentrations of SEs and TAG varies greatly between cell types. For instance, foamy macrophages and cells of the adrenal cortex have high amounts of SEs, but whether these cell types generally exhibit this intra-LD neutral lipid organization is unknown. Liquid crystalline phases have been observed in LDs in hepatocytes in mouse models of MASLD using polarized light[44]. The organization and phase of SEs may impact phospholipid packing and protein association with the LD. However, the regulation and physiological consequences of SE liquid crystalline phase transitions in LDs remain open questions.

1.2.4 Lipid droplet fusion

A key mechanism of LD growth is LD–LD fusion (Figure 1-1C). This process involves the CIDE proteins—CIDEA, CIDEB, and CIDEC (also known as FSP27)—which enrich at LD–LD contact sites and form a channel for directional neutral lipid (for example, TAG) transfer from the smaller LD to the larger LD through Ostwald ripening[45]. Recent findings propose that CIDEC undergoes membrane-constrained liquid–liquid phase separation, forming a gel-like protein condensate that is lipid permeable[46]. Rab8, Plin1 and CLSTN3β also control LD fusion activity through their interactions with CIDEC[45,47].

1.3 Lipid droplet protein trafficking

LD proteins are classified into two groups based on the pathways that they employ to traffic to LDs: class I LD proteins (also denoted as ER-to-LD, or ERTOLD) and class II LD proteins (also denoted as cytoplasm-to-LD, or CYTOLD)[9,48] (Figure 1-2A).

1.3.1 Class I and Class II protein targeting to the LD surface

Class I LD proteins typically contain a hydrophobic hairpin domain that inserts into the ER. These proteins laterally diffuse from the ER into forming LDs or into mature LDs via membrane continuities between the ER and LDs[9,48,49]. Examples of class I LD proteins include ACSL3, GPAT4, UBXD8, LDAH and HSD17B11[50]. Whether class I LD proteins generally use the Sec61 translocon for ER insertion or use alternative pathways, such as the Pex19/Pex3 pathway employed by the ER–LD protein UBXD8[51] remains under-explored. Although their membranes are continuous, the ER and LDs maintain unique proteomes, and the mechanisms that determine protein trafficking from the ER into LDs are an area of high interest. The ER–LD membrane junction serves as a semi-permeable protein diffusion barrier that is permissive to the trafficking of proteins with specific topologies (Figure 1-2A). Monotopic proteins that associate primarily with the outer phospholipid leaflet of the ER membrane, such as those containing hydrophobic hairpin domains, traffic from the ER to LDs. The trafficking of proteins with permissive topologies to LDs is also influenced by their interactions with ER transmembrane proteins, which are ER restricted and may serve as ER anchors to prevent their trafficking to LDs[50,52] (Figure 1-2). Some proteins adopt distinct conformations in bilayer and monolayer membranes, and the more energetically favorable conformation can drive enrichment in a particular membrane environment (for example, in LDs)[48]. However, the structures that LD proteins adopt in bilayer and monolayer membranes remain poorly understood, and more studies are needed before general rules regarding LD protein partitioning between the ER and LDs can be defined. Finally, seipin serves as a gatekeeper at the ER–LD membrane junction that restricts trafficking to a specific set of class I LD proteins[50]. Whether it influences the movement of specific lipids, other than neutral lipids, between the ER and LDs has not been addressed. Other class I LD proteins localize to LDs at later time points by trafficking across a distinct membrane bridge (that is, a hemi-fusion of the LD monolayer and outer leaflet of the ER membrane) that is formed through the actions of a set of membrane fusion machinery, including SNARE proteins and a tether, at ER exit sites[50]. Many questions remain regarding the regulation, formation, and structures of these membrane bridges.

Class II LD proteins, such as LSD1, CGI-58 and CCT1, are synthesized on cytosolic ribosomes and insert directly into LDs by recognizing characteristic phospholipid packing defects and the exposed neutral lipids present in the LD phospholipid monolayer[9,48] (Figure 1-2A). Class II LD proteins do not contain a canonical organelle-targeting signal sequence but typically contain an amphipathic helix that is important for insertion into the LD membrane packing defects[9,48]. Membrane insertion may stabilize the helix structure and retain the protein on LDs. However, research into the targeting mechanisms used by class II LD proteins that lack obvious amphipathic helices is needed. For example, the solution state NMR structure of an LD-targeting peptide of CGI-58 revealed a compact

hydrophobic, tryptophan-rich LD anchor that contains two prolines that prohibit extended helix formation[53]. Some LD proteins are covalently modified by Fas, such as the myristoylation of FSP1, palmitoylation of ELMOD2, SNAP23 and Arf1, and prenylation of ALDH3B2[9]. While these FA modifications serve as membrane anchors that are necessary for their localization to LDs, they are unlikely to be sufficient for selective LD targeting.

1.3.2 Phospholipid packing defects and TAG dynamics of the monolayer surface

LD phospholipid monolayers are predicted to have larger and more persistent packing defects than phospholipid bilayers[54] (Figure 1-1B). This unique aspect of the LD membrane mediates the preferential targeting of LDs by class II LD proteins[48]. The identity of the exposed neutral lipids may influence protein binding and recruitment, since amphipathic helices from class II LD proteins exhibit distinct binding preferences to artificial LDs generated with different neutral lipids[55] and proteins with different amphipathic helices can bind to separate subpopulations of LDs[56]. Three types of phospholipid packing defect have been described in molecular dynamics simulations: defects that involve the exposure of phospholipid acyl chains, of TAG acyl chains, and of the TAG glycerol backbone[57]. SURF-TAGs are the subset of TAGs that are stably at the surface and ordered like phospholipids, with the glycerol backbone oriented towards the cytosol and the acyl chains towards the core of the LD[57]. When the amount of surface coverage by phospholipids is low, SURF-TAGs may function as an additional membrane component and reduce surface tension[57]. The TAG deeper in the core of the LD (CORE-TAG) is disordered, although they may intercalate with the phospholipid acyl chains and impact phospholipid packing and acyl chain order[57]. An intriguing possibility is that the distinct molecular properties of the different packing defects impact LD protein association.

1.4 Accessing the lipids stored in lipid droplets through lipolysis and lipophagy

To meet cellular needs for energy and provide precursors for signaling and membrane lipids, cells access FAs stored as TAGs in LDs through: (1) lipolysis, the hydrolysis of TAGs by lipases that associate with the LD monolayer, and (2) lipophagy, the delivery of LDs or a portion of the LD to lysosomes for hydrolysis by lysosomal acid lipase (LAL)[58,59] (Figure 1-2).

1.4.1 Lipolytic degradation of LDs by cytosolic lipases

Lipolysis is primarily mediated by three lipases that associate with LDs and function in sequence to hydrolyze stored TAGs[59] (Figure 1-3A). Adipose triglyceride lipase (ATGL, also known as PNPLA2) mediates the first and rate-limiting reaction in the pathway, converting TAG into DAG with the release of a free FA[59]. Hormone-sensitive lipase (HSL) and monoacylglycerol lipase (MGL) mediate the subsequent FA hydrolysis steps, with HSL converting DAG to monoacylglycerol (MAG) and MGL converting MAG to glycerol[59]. The preference of these enzymes for particular lipids and specific FAs is well characterized[59]. Lipolytically released FAs can be re-esterified and incorporated into newly synthesized TAG, and cycles of lipolysis and re-esterification have been proposed to contribute to the remodeling of TAG FA composition in adipocytes (Figure 1-1D).

ATGL consists of an N-terminal patatin domain, containing the catalytic dyad with an active-site serine and an aspartate, and a C-terminal domain that embeds into LDs[59]. Although the C terminus of ATGL is dispensable for its lipase activity in vitro, it is required for the localization of ATGL to LDs and for the lipolytic breakdown of LDs in cells[59]. How the ATGL patatin domain interacts with a buried hydrophobic substrate (that is, TAG) to enable access to the active site for FA hydrolysis is unclear. One possibility is that ATGL preferentially associates with surface TAGs (SURF-TAGs) that are exposed at packing defects between phospholipid head groups (Figure 1-1B). ATGL traffics to LDs from a proximal ER-Golgi intermediate compartment and through SAR1–COPII and GBF1–ARF1–COPI[60–62]. ATGL may traffic via the pathway for late class I LD proteins across membrane bridges[63].

As the rate-limiting enzyme in lipolysis, ATGL is subject to regulatory mechanisms that control its lipolytic activity[63] (Figure 1-3A). The ATGL binding partner CGI-58 (also known as ABHD5) is an ATGL activator, increasing the TAG hydrolase activity of ATGL by up to 20-fold[64]. The regulation of the ATGL and CGI-58 interaction is a major target of multiple mechanisms of lipolysis regulation[63]. For example, in the canonical pathway of hormone-stimulated lipolysis in adipocytes, hormone activation of the β_3-adrenergic receptor leads to adenylate cyclase activation, increased cyclic AMP, and the activation of protein kinase A (PKA). PKA phosphorylates multiple sites on the LD-associated PLIN1, disrupting the PLIN1–CGI-58 interaction and promoting the association of CGI-58 and ATGL[63,65]. In addition, PKA phosphorylates multiple sites on HSL, increasing its lipolytic activity and association with LDs[63,65]. PLIN5 inhibits lipolysis by binding independently to ATGL and CGI-58 in a mutually exclusive manner, reducing the association of ATGL and CGI-58[66]. Interestingly, the PNPLA3(I148M) variant, which is associated with high risk for metabolic dysfunction-associated steatotic liver disease (MASLD), increases the affinity of PNPLA3 for CGI-58[67]. This interaction prevents the association of CGI-58 with ATGL, leading to reduced lipolysis and potentially promoting the progression of steatotic liver disease[67,68]. Consistent with these emerging data, synthetic ligands that disrupt the interaction of CGI-58 with PLIN1 and PLIN5 are sufficient to trigger lipolysis in the absence of PKA activation[69]. Disrupting the PNPLA3–CGI-58 interaction may be therapeutically valuable as an approach to treat MASLD. In addition to the mechanisms targeting the ATGL–CGI-58 interaction, ATGL activity is non-competitively inhibited by direct binding of G0S2[70] and HILPDA[71]. Recent computational modelling and mutational analyses have provided important insights into ATGL interactions[72–74]. However, obtaining high-resolution structures of the lipolytic complexes remains of utmost importance for understanding the regulation of lipolysis and for the rational development of therapeutics targeting these factors. The utility of small molecules targeting this pathway is exemplified by the development of inhibitors for mouse ATGL (ATGListatin[75]) and human ATGL (NG-497[75]). Finally, in addition to its canonical role in lipolysis, ATGL has a less appreciated role as an acyltransferase in anabolic lipid pathways.

1.4.2 Lipid cycling and FA remodeling in lipid droplets

Re-esterification of lipolytically released FAs primarily occurs in the ER, and either leads to TAG deposition in new LDs or trafficking to existing LDs (presumably via an ER–LD

membrane continuity; Figure 1-1D). Some portion of re-esterification may also occur at the LD surface through LD-localized lipid metabolic enzymes[49]. The process of lipolysis and re-esterification is sometimes referred to as the glyceride–FA futile cycle, since the cycle is energetically costly through consumption of ATP accompanied by no net change in the concentration of TAG or FAs[76,77]. Mass-spectrometry-based tracking of the fate of labelled FAs in cultured adipocytes indicated that an FA has an approximately 4-hour half-life within a TAG molecule and that TAG exchanges all FA chains within around 24 hours[76]. Interestingly, the released FAs were desaturated and elongated, leading to remodeling of the TAG composition over time[76]. Although the purpose for this lipid cycling is unclear, it may provide a pool of accessible glycerol and FAs for rapid generation of lipid signaling molecules or phospholipids as well as a mechanism to generate diversity in stored FAs. Unknowns include whether this happens similarly in vivo, how much cycling occurs in non-adipocyte cells and the contribution of the glyceride–FA futile cycle to basal metabolic rate.

1.4.3 Anabolic roles for ATGL

The ATGL transacylase activity is necessary for the biosynthesis of branched FA esters of hydroxy FAs (FAHFAs), some of which have anti-inflammatory and anti-diabetic roles[78,79]. ATGL esterification of a hydroxy FA with an FA derived from either TAG or DAG (that is, a transacylation reaction), generates a FAHFA[78]. Knockout of *ATGL* in adipose tissue decreases the amount of FAHFAs and FAHFA–TAGs[78]. These data indicate an important role for the transacylase activity of ATGL in the generation of a disease-modifying signaling lipid. The presence of FAHFA–TAGs raises the question as to whether there are mechanisms to selectively target the hydrolysis of specific TAGs with distinct compositions to enable the release of specific FAs for signaling (such as FAHFAs) or for use in other biosynthetic processes. In addition to this transacylase activity, ATGL has been found to synthesize TAGs from DAGs and DAGs from MAGs through acyl-CoA independent transacylation in vitro[80]. The importance of the ATGL acyltransferase activity for DAG and TAG synthesis in cells remains poorly understood.

1.4.4 Lipid droplet degradation by autophagy

Lipophagy is the selective delivery of LDs or portions of LDs to the lysosome where LAL mediates all hydrolysis steps, breaking TAG down into glycerol and its free FA constituents[58] Lipophagy can be separated into two distinct pathways, macrolipophagy and microlipophagy[58] (Figure 1-3B).

In macrolipophagy, the LD is engulfed within an autophagosome, which fuses with the lysosome to form an autolysosome and facilitate LD degradation[58]. Macrolipophagy preferentially mediates the clearance of smaller LDs, perhaps indicating a size limit for the autophagosomal engulfment of LDs[81]. Lipolysis and chaperone-mediated autophagy (CMA) cooperate to reduce the size of LDs to promote more efficient macrolipophagy. During periods of nutrient deprivation, the energy sensor AMP-activated protein kinase (AMPK) induces CMA-dependent degradation of PLIN2 and PLIN3, promoting lipase recruitment and the lipolytic degradation of LDs[1]. Lipolysis may reduce the size of existing LDs or result in the re-esterification of TAG and packaging into nascent LDs of a size that is conducive for macrolipophagy[81]. Macrolipophagy involves receptors and adaptors that

link autophagosomal membranes to the target cargo directly or by binding to ubiquitinated proteins associated with the cargo[81]. For example, the canonical ubiquitin-binding soluble autophagosome receptors SQSTM1 (also known as p62), optineurin and NBR1 promote lipophagy[81], but it is not clear which LD proteins are ubiquitinated or which E3 ubiquitin–protein ligases mediate the ubiquitination. Spartin, which was previously suggested to recruit E3 ubiquitin ligases to the LD surface[9], directly recruits LC3A- and LC3C-decorated autophagic membranes via a LC3-interacting region (LIR) and promotes lipophagy[82]. Spartin is mutated in a form of spastic paraplegia, and spartin-dependent lipophagy has important roles in neurons[82]. Whether spartin has similar roles in other tissues and the mechanisms that regulate spartin-driven lipophagy remain to be determined. The identification and characterization of selective lipophagy receptors continues to be important for dissecting the contribution of lipophagy to LD regulation and lipid homeostasis. The autophagic membrane is extended and sealed to fully envelope the LD (or portion of the LD) through a process involving microtubule motors and membrane deforming proteins as well as small Rab GTPases, some of which may be selective to lipophagy (for example, Rab10–EHBP1–EHD2 complex)[58]. As an alternative to macrolipophagy, microlipophagy involves the direct transmission of TAGs or portions of the LD into the lysosome, independent of an autophagosome (Figure 1-2B).

1.4.5 Microlipophagy and direct delivery of lipids to the lysosome

A non-canonical form of lipophagy involves the direct recruitment of ATG3 to large LDs in cultured 3T3-L1 differentiated adipocytes and Huh7 hepatoma cells[149] On LDs, ATG3 mediates LC3B lipidation, conjugating LC3B to LD phosphatidylethanolamine, subsequently recruiting LC3B-decorated membranes to LDs[83]. The LC3B-decorated membranes are acidified without the LD being fully engulfed[83]. LC3 can undergo trans-homodimerization, and it is possible that LD-lipidated LC3B interactions with LC3B on autophagic membranes mediate the observed recruitment and tethering. This type of lipophagy may facilitate the direct targeting of large LDs by overcoming the requirement for reducing their size to enable encapsulation in an autophagosome. The functional importance of this non-canonical form of lipophagy in mediating TAG hydrolysis is unclear and requires further study.

Although microlipophagy has been studied in yeast for many years, microlipophagy was only recently demonstrated to occur in cultured hepatocytes[58,84]. Time-lapse imaging revealed ‘kiss-and-run’ type encounters between LDs and lysosomes (~30–60 seconds) that involve the transfer of lipids and proteins from the LD to the lysosome[84]. In some cases, the entire LD was engulfed and consumed by the lysosome, but often only a portion was transferred[84]. Electron microscopy confirmed this relationship and revealed an apparent injection of lipid from the LD into the lysosome1[84]. Key to this process is the small GTPase ARL8B, which promotes LD-lysosomal MCS generation through the formation of heterotypic complexes with its GDP-bound state associating with LDs and GTP-bound state associating with lysosomes[85]. The role of ARL8B in LD turnover appears to be particularly important in macrophages, where this is the primary pathway of LD catabolism[85]. Given the piece-meal engulfment of portions of LDs by lysosomes or the injection of lipid into lysosomes, significant force generation to achieve such

membrane deformations is likely required (for example, via actomyosin cytoskeletal machinery or ESCRT proteins).

1.5 Lipid droplet contacts sites and inter-organelle lipid transfer

LDs form contacts with nearly all organelles[86] (Figure 1-4). By definition, the membranes at membrane contact sites (MCSs) are held in close proximity (< 30 nm) but are not fused, allowing lipid transfer across small gaps[87]. This contrasts with the membrane continuities that connect the ER to LDs during biogenesis (for example, ER–LD bridges) (Figure 1-2) and potentially at cell death-inducing DFFA-like effector (CIDE)-mediated LD–LD contacts (Figure 1-1), which allow for direct inter-organelle neutral lipid transfer. At MCSs, lipid transfer proteins (LTPs) have a key role in overcoming the energetic barrier of lipid desorption by providing a hydrophobic cavity that shields lipids during transport[88,89]. The enrichment of LTPs at MCSs may increase the efficiency and selectivity of lipid transport between two organelles (Figure 1-4). LTPs can be grouped into two classes, shuttle and bridge LTPs[88,89]. Shuttle LTPs bind and transfer lipids one at a time from a donor to acceptor membrane, enabling the remodeling of organelle membrane composition and function, the formation of lipid microdomains, and the regulation of lipid signalling[89]. By contrast, bridge LTPs bind many lipids simultaneously along an extended hydrophobic groove, potentially allowing them to have more substantial roles in bulk lipid transfer for organelle biogenesis and expansion[88]. Both types of LTP have been observed at LD MCSs and selected examples are discussed below. In many cases, the tethering proteins and functions of LD MCSs remain to be defined.

1.5.1 Lipid droplet–endoplasmic reticulum contact sites

Several tethering proteins and LTPs have been identified at ER–LD MCSs (Figure 1-4), including the shuttle-type LTPs oxysterol binding related proteins 5 and 8 (ORP5 and ORP8)[90,91]. ORP5 and ORP8 are single-pass ER transmembrane proteins that have a canonical role at ER–plasma membrane contacts where they use a lipid counter-transport mechanism to transfer their specific lipid ligands up their concentration gradient (for example, PS to the plasma membrane) by coupling their transport with the movement of phosphatidylinositol-4-phosphate (PtdIns4P) down its concentration gradient[89]. ORP5 may have a similar role on LDs, since LDs in ORP5-deficient cells exhibit reduced PS and increased PtdIns4P[90]. ORP5-deficient cells exhibit enhanced neutral lipid synthesis and enlarged LDs[90]. ORP5 and ORP8 also form a complex and are involved in the biogenesis of LDs at ER–mitochondria MCSs, known as mitochondrial associated membranes (MAMs), that are enriched in phosphatidic acid[91]. ORP5/8 interact with seipin, and ORP5/8-promotion of LD biogenesis may involve recruitment of seipin to MAMs[91]. Questions remain regarding the lipids that ORP5 and ORP8 transfer at these sites, the role of these lipids in LD regulation, and the purpose for the tripartite LD, ER and mitochondria MCS. In addition to ORP5 and ORP8, ORP2 also localizes to LDs[92]. ORP2 is a soluble LTP that contains a FFAT motif that facilitates its interaction with VAP at ER–LD contact sites[92]. ORP2 regulates TAG synthesis and turnover, as well as SE synthesis[92]. The mechanism of ORP2 regulation of lipolysis may involve its interaction with COPB1 to promote ATGL trafficking to LDs[93]. The lipid-binding and lipid-transfer functions of ORP2 in regulating LDs are unclear.

ATG2 is a bridge-type LTP that localizes to LDs[94–96]. Depletion of ATG2 results in the accumulation of large, clustered LDs[94]. Purified ATG2 transfers phospholipids between a bilayer liposome and the monolayer of an artificial LD in vitro[95]. Mutations that are predicted to inhibit lipid channeling along the protein, but not binding and shuttle-type transfer activities, block lipid transfer in vitro and are unable to rescue LD phenotypes in *ATG2* knockout cells[95]. These data support a model in which ATG2 mediates phospholipid transfer between membranes, presumably the ER and the monolayer membrane of LDs. The proposed lipid transfer involves the lateral diffusion of lipids along the hydrophobic groove of the protein, although this model remains to be proven. Two of the VSP13 family of bridge-type LTPs, VPS13A and VPS13C, have been observed at ER–LD MCSs and found to influence LD amounts[97–99]; VPS13A depletion seems to have context-specific effects on LD abundance and changes in ATGL recruitment and lipolysis may explain some of these effects[97,99]. In vitro studies demonstrating the ability of VPS13A/C to transfer lipids to or from LDs and mutational studies analyzing the importance of lipid-binding and bridge-type LTP structure are lacking.

Coupling of bridge LTPs with scramblases serves to maintain bilayer integrity and may promote lipid transfer by preserving lipid concentration gradients[88,100]. For example, ATG2 associates with the ER scramblases VMP1 and TMEM41B and with the autophagosome-localized scramblase ATG9 to mediate phospholipid transfer during autophagosome biogenesis[100–102]. Depletion of VMP1 and TMEM41B leads to enlarged LDs, and in hepatocytes the loss of VMP1 and TMEM41B is associated with the accumulation of ER lumenal LDs and disruptions in lipoprotein secretion, suggesting that the altered ER membrane composition disrupts neutral lipid flux and lipoprotein biogenesis[30–33]. Interestingly, loss of the autophagosome scramblase ATG9 also results in LD accumulation, potentially due to reduced lipid channeling to autophagosomes and increased lipid storage in LDs[34]. Thus, multiple scramblases present in different organelles coordinate with bridge-type LTPs, such as ATG2, to regulate LDs and intracellular lipid homeostasis.

Many questions regarding the role of bridge-type LTPs in LD regulation remain, including the lipids that are transferred, the direction of lipid transfer, whether the different bridge-type LTPs have redundant roles, and the mechanism by which bridge-type LTPs regulate LDs[88]. The mechanisms that enable directional lipid transfer along bridge-type LTPs remain poorly understood, although organelle expansion or lipid metabolism could feasibly maintain a concentration gradient to drive directionality[88]. It is tempting to speculate that bridge-type LTPs transfer phospholipids to LDs that act as surfactants to enable LD expansion or fusion. A requirement for phospholipid transfer proteins during this step may imply that phospholipid diffusion at ER–LD continuities is limiting for growth. It is equally possible that phospholipids may flow from LDs to the ER during the lipolytic breakdown of LDs or as a mechanism to regulate the number of packing defects in the LD monolayer. Why existing ER–LD membrane continuities, which would presumably allow for phospholipid diffusion, would not be sufficient for ER–LD phospholipid transfer is not clear. A benefit of LTPs is that they may enable the transfer of specific lipids and LTPs may be more amenable to regulation.

1.5.2 Lipid droplet–mitochondria contact sites

LD–mitochondria MCSs have been implicated in both the breakdown and biogenesis of LDs, likely reflecting cell-type-specific and metabolic state-dependent roles of these sites (Figure 1-4). PLIN5, which is primarily expressed in oxidative tissues, was the first LD–mitochondria tethering protein to be identified, and early data demonstrated that PLIN5 is sufficient to trigger mitochondria recruitment to LDs[103]. PLIN5 consists of an LD-inserted N-terminal domain and a C-terminal domain that mediates mitochondria tethering through interactions with the acyl-CoA synthetase FATP4[104]. In a myoblast cell line, the PLIN5–FATP4 interaction facilitates the rapid esterification of FAs released during stimulated lipolysis and their uptake into mitochondria for β-oxidation[104]. Positioning of acyl-CoA synthetases at MCSs may be a general mechanism to facilitate the local generation of activated FAs for channeling into specific pathways, such as Mdm1 recruitment of the acyl-CoA synthetase Faa1 to ER–LD–vacuole contacts in yeast[105] and an ACSL1 association with SNAP23 in hepatocytes at LD–mitochondria contacts[105]. PLIN5 interacts with other proteins that promote the formation of LD–mitochondria MCSs such as the AMPK-stimulated interaction with Rab8a, which promotes FA transfer and β-oxidation in a myoblast cell line[106]. PLIN5 binds FAs[104,107], but the importance of PLIN5 FA binding at LD–mitochondria MCSs is not known. Additional proteins localize to LD–mitochondria MCSs and promote lipid transfer from LDs to mitochondria during nutrient deprivation, such as TSG101 and the bridge-type LTP VPS13D94, which potentially act through a mechanism involving ESCRT remodeling of LDs.

In contrast with what was observed in myoblasts and some non-adipocyte cell lines[104,106,108,109], LD MCSs in adipocytes have primarily been associated with the biogenesis of LDs rather than their breakdown[110,111]. In brown adipocytes, two mitochondrial populations were observed, one associated with LDs (that is, peri-droplet mitochondria) and one that was not (that is, cytosolic mitochondria)[110]. Perhaps surprisingly, the peri-droplet mitochondria exhibit low amounts of FA oxidation compared with the cytosolic mitochondria. Cold-induced thermogenesis reduces mitochondria–LD contacts, increasing FA oxidation and the pool of cytosolic mitochondria[110]. The peri-droplet mitochondria exhibit higher amounts of ATP synthesis and generation of tricarboxylic acid intermediates such as citrate, potentially fueling de novo FA synthesis and LD growth[110]. Similarly, peri-droplet mitochondria support LD growth and cytosolic mitochondria mediate FA oxidation in hepatocytes[112]. Consistent with this model, PLIN5 overexpression in brown adipocytes increases mitochondria–LD MCSs and results in large LDs[110]. However, in other studies, PLIN5 depletion in cultured brown fat cells was associated with reduced mitochondrial respiration and PLIN5 promoted brown adipose tissue uptake and oxidation of FAs in mouse models, potentially driven in part by altered thermogenic gene expression[113,114]. The different effects may reflect distinct roles of PLIN5 in promoting LD–mitochondria contacts and regulating thermogenic transcriptional programs.

Although white adipocytes exhibit LD–mitochondria MCSs, they either do not express PLIN5 or express it at very low levels. White adipocytes have the outer mitochondrial protein MIGA2 that contains an LD-binding amphipathic helix that mediates LD tethering and an FFAT motif that promotes ER tethering through interactions with VAP-A and VAP-

B[111]. MIGA2 enhances the conversion of glucose into TAG, suggesting that the role of MIGA2 organelle tethering is to promote TAG synthesis from non-lipid precursors and the expansion of LDs[111]. Interestingly, a hydrophobic cavity in MIGA2 is capable of accommodating two lipids, including phospholipids and FAs[115,116]. MIGA2 can transfer phospholipids between membranes in vitro, which is important for MIGA2 cellular functions[115,116]. However, whether MIGA2 transfers phospholipids or FAs at these sites, as well as the purpose for lipid transfer, has not been established.

While emerging findings provide exciting insights into the factors and protein complexes that mediate LD–mitochondria MCSs, they also highlight the many questions that remain regarding the regulation of these contacts as well as their cell type-specific and context-dependent roles in regulating lipid and energy metabolism.

1.6 Emerging roles for lipid droplets in lipotoxicity

1.6.1 Lipid droplets suppress FA-induced ER stress and mitochondrial dysfunction

High levels of saturated FAs, such as palmitate, trigger cell death[117]. Palmitate is associated with the production of di-saturated glycerolipids and the upregulation of ER stress signaling, which induces apoptosis via IRE1 activation of JNK kinase and the cleavage of caspases[118,119]. Inhibition of glycerolipid synthesis by depletion of GPAT4 strongly suppresses palmitate toxicity[118–120], consistent with the role for the di-glycerolipids as the toxic lipid species. Both PERK and IRE1, two important transducers of ER stress, sense membrane fluidity and initiate signaling responses[121,122]. The fluidity of the membrane is determined in part by the ratio of conjugated saturated and unsaturated FAs in membrane lipids, which can induce allosteric changes in the IRE1 and PERK transmembrane domains that influence their oligomerization and signalling[121,122]. The relative contribution of different di-saturated glycerolipids species (that is, phosphatidic acid, DAG or specific phospholipids) to palmitate toxicity is unclear.

LDs suppress palmitate-induced toxicity by sequestering palmitate within TAG that is stored in LDs, reducing its incorporation into membrane glycerolipids[117,119,123] (Figure 1-5). This protective activity can be enhanced by SCD1-dependent conversion of saturated FAs into unsaturated FAs, which are not only less toxic but are also superior substrates for TAG synthesis and can facilitate palmitate incorporation into TAG. Interestingly, the E3 ligase RNF213 inhibits SCD1 activity, and depletion of RNF213 ameliorates palmitate toxicity[119]. RNF213 is a unique E3 ligase that was recently found to ubiquitinate the lipid lipopolysaccharide, rather than a protein, during bacteria infection[124]. RNF213 localizes to LDs and influences lipolysis[125]. Whether the effects of RNF213 on SCD1 and palmitate toxicity are direct or indirect and whether the localization of RNF213 to LDs or its unique lipid ubiquitination activity are important for its roles in lipotoxicity are unknown. Similar to the effect of exogenous palmitate treatment, ER stress induction and upregulation of inflammation have been observed in adipocytes when TAG synthesis is blocked by DGAT1 inhibition during stimulated lipolysis[123]. Whether saturated FAs and di-saturated glycerolipids are the culprit toxic species under this complex scenario in which many FAs of different length and saturation are released from TAG is not known.

Lipotoxicity resulting from the inhibition of LDs is not always associated with ER stress induction. For example, nutrient deprivation induces high autophagic flux to recycle cellular components, providing substrates for energy and building blocks for important macromolecules. During the breakdown of organelles, membranes are degraded, and lipids are released[108,109]. The mechanisms that govern trafficking of released FAs into different organelles and pathways is poorly understood, but may involve MCSs and coupling to metabolic enzymes such as acyl-CoA synthetases (for example, PLIN5–FATP4 at LD–mitochondria MCSs[104]). In response to the released lipids, DGAT1-dependent LDs are formed to mitigate lipotoxicity[108] (Fig 1-5). Under these conditions, DGAT1 inhibition results in the accumulation of high amounts of acylcarnitines, and a subsequent loss of the mitochondrial membrane potential and reduction in mitochondrial respiration[108]. Blocking acylcarnitine synthesis reduces the toxicity, suggesting a direct role for acylcarnitines in altering mitochondrial function[108]. Indeed, acylcarnitines can disrupt mitochondrial membrane integrity in vitro[108], but whether this is the toxic mechanism in cells is unclear.

The emerging theme is that TAG synthesis and storage in LDs suppresses the flux of FAs, and likely other lipids (for example, ceramides[126]), into toxic species in a context-dependent manner. Why DGAT1 has been observed to have a larger role in lipotoxicity than DGAT2 is not immediately clear, although it is possible that this reflects differences in DGAT1 and DGAT2 substrate preferences, their distinct localizations and roles in LD biogenesis and growth, or their relative expression patterns in different cell types.

1.6.2 LDs have context-specific roles in oxidative lipid damage and ferroptosis

A universal feature in the execution of ferroptosis is a failure in lipid quality control and an overwhelming accumulation of oxidatively damaged phospholipid hydroperoxides[127,128]. The primary cellular defense against ferroptosis is mediated by the glutathione-dependent peroxidase GPX4, which uses glutathione as a co-factor to convert toxic lipid peroxides into more benign lipid alcohols[129]. A parallel pathway that prevents ferroptosis involves the NAD(P)H-dependent oxidoreductase FSP1, which generates the reduced antioxidant form of quinone radical trapping antioxidants (for example, coenzyme Q10[130,131] and vitamin K[132,133]) that prevent the propagation of lipid peroxidation. Ferroptosis sensitivity is also determined by a complex interplay between iron metabolism, lipid metabolism, and the generation of damaging radicals[127,128].

Polyunsaturated FAs (PUFAs) are highly prone to oxidation, and the PUFA:MUFA ratio in membranes has emerged as a major determinant of cellular sensitivity to ferroptosis[134]. For example, depleting membranes of oxidizable PUFAs by inhibiting the PUFA-preferring acyl-CoA synthetase ACSL4[135] or by the addition of monounsaturated fatty acids (MUFAs)[136], which compete with PUFAs for incorporation into phospholipids, suppresses ferroptosis induced by GPX4 inhibition. By contrast, increasing the amount of oxidizable PUFAs in membrane lipids by the exogenous addition of PUFAs sensitizes cancer cells to ferroptosis[80]. In most cases, LDs have a protective role by sequestering PUFAs that would otherwise be channeled into membrane phospholipids (Figure 1-5). For example, under acidic conditions that mimic the tumor microenvironment, cultured cancer cells upregulate FA uptake and exhibit higher amounts of LDs[80]. Addition of

PUFAs to these cancer cells sensitizes them to ferroptosis induction, but the effect of the PUFAs is reduced due to their incorporation into TAGs stored in LDs[80]. DGAT1 and DGAT2 inhibition blocks the incorporation of the added PUFAs into LDs, leading to increased PUFAs channeling into phospholipids and a greater sensitivity to ferroptosis induction[80]. Remarkably, a PUFA-rich diet triggers ferroptosis and suppresses tumor growth in a mouse xenograft model, and the effects are even greater when DGAT inhibitors are injected to promote PUFA flux into phospholipids rather than TAGs[137]. Consistent with the protective role of LDs in sequestering PUFAs, the loss of *CDKN2A* in glioblastoma reduces PUFA-containing TAGs and LDs, leading to increased lipid peroxidation and ferroptosis sensitivity[138]. In addition to these cell-autonomous mechanisms, storage of PUFAs in glial LDs prevents lipid peroxidation in neurons[137,139]. In some cases, this may involve active FA efflux and transfer from neurons to astrocytes, where the FAs are sequestered in LDs and degraded[5,137,140]. Neurons form LDs but the amounts of LDs in neurons are typically low, and the supporting role of astrocytes in storing FAs and regulating the lipid composition of neurons may be important for determining their propensity to undergo ferroptosis and degeneration.

It has been proposed that PUFAs stored as TAGs in LDs are protected from oxidative damage. However, oxidized TAG has been detected by lipidomics[141], potentially indicating oxidative damage to existing TAG or TAG esterification with oxidized FAs. Molecular dynamics simulations indicate increased partitioning of oxidized TAG into the LD phospholipid monolayer due to increased affinity of the hydrophobic acyl chains for the polar aqueous phase[141]. However, whether lipids within LDs are less prone to oxidation than other lipids and the mechanisms that regulate TAG oxidation are poorly understood. FSP1 localizes to LDs[131,132], and it is possible that FSP1 regenerates an LD-localized antioxidant molecule to protect TAGs (similar to its role at the plasma membrane[130,131]), but this hypothesis has not been explored. It is also possible that CORE-TAGs buried in the center of LDs are less susceptible to radical interactions and peroxidation due to the reduced proximity to cytosolic radical species, and preferential interactions of radicals with the LD monolayer phospholipids could lead to reduced TAG interaction and oxidation.

LDs do not always protect against ferroptosis. Simultaneous inhibition of cystine uptake (that is, with a system x_c^- inhibitor), which is required for glutathione synthesis, and treatment with dehydroascorbic acid (that is, oxidized vitamin C) trigger ferroptosis that involves the oxidation of LDs[142]. Under these conditions, inhibition of DGAT1 lowers ferroptosis sensitivity[142]. A ferroptosis-promoting role was also found for the ATGL inhibitor HILPDA in clear cell renal cell carcinoma cells[143]. Whether TAG oxidation contributes to the propagation of ferroptosis is an open question. It is possible that the release of PUFAs from LDs promotes the formation of oxidation-prone PUFA-containing phospholipids, or if TAGs are oxidized, the release of oxidized PUFAs or their breakdown products may promote the spread of lipid peroxidation to other membranes (Figure 1-5). LD MCSs may influence the channeling of released PUFAs towards particular fates, such as β-oxidation or incorporation into membrane phospholipids, but this has not been explored in the context of ferroptosis. The context-dependent roles of LDs in ferroptosis likely reflect a combination of factors, including the intrinsic propensity of a cell type to

form LDs, the FA composition of TAG stored in LDs and the expression of factors that govern MUFA- and PUFA-channeling into membrane phospholipids and TAGs.

1.7 Conclusion

LDs are dynamic lipid storage organelles that have a crucial involvement in cellular lipid homeostasis; yet many outstanding questions remain. These include defining the mechanisms that govern the unique compositions and functions of LD subpopulations, the importance of LD lipid phase transitions and their regulation, the full inventory of tethering proteins and LTPs and their roles in MCSs, and the numerous roles of LDs in regulating lipid flux and toxicity. Recent genetic screens highlight the expansive network of factors that mediate cell type and metabolic state-dependent regulation of LDs[144,145], emphasizing the importance of considering cellular context. It is likely that many important cell-type- and metabolic-state-dependent mechanisms of regulation and cellular roles for LDs remain to be discovered. Data portals such as CRISPRlipid[144] and the Lipid Droplet Knowledge Portal[146] provide access to large datasets and comparative tools that are useful for uncovering mechanisms of LD regulation and function. Although advances in chemical biology approaches are providing tools to study lipid movement and metabolism, many challenges remain related to the quantitative analysis of lipid trafficking from organelle to organelle and to studying lipid flux in vivo. The coming years are bound to be an exciting time in this field, with emerging technologies providing requisite approaches to define the mechanisms, functions and regulation of LDs and lipid flux.

1.8 Figures

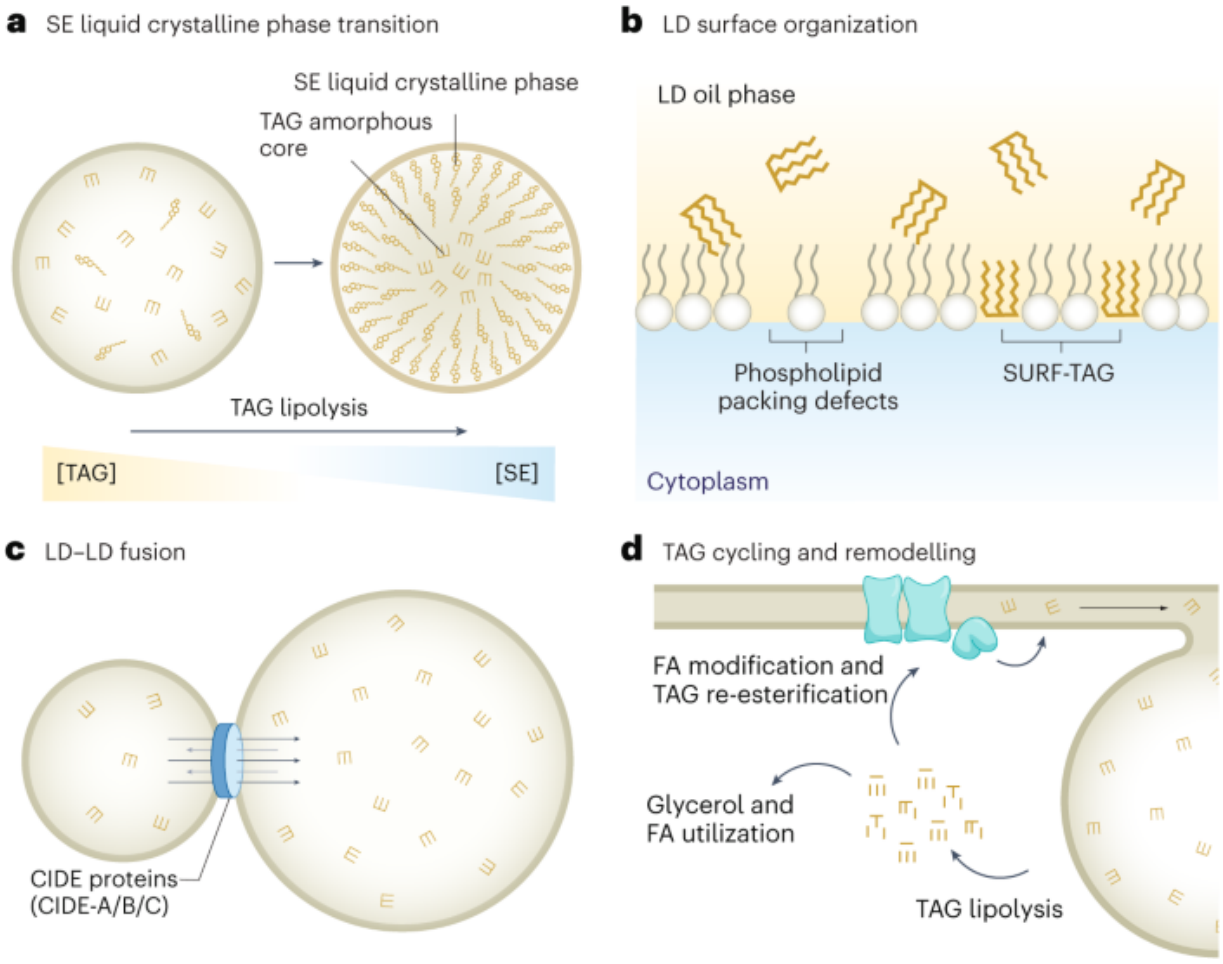

Figure 1-1: Lipid dynamics in and between lipid droplets.
A) SE lipid phase transition under high SE to TAG ratios. B) Phospholipid packing defects and SURF-TAGs. C) LD–LD fusion via CIDE-mediated TAG transfer driven by Ostwald ripening. D) FA modifications and remodeling of TAG composition during cycles of TAG breakdown and FA re-esterification.

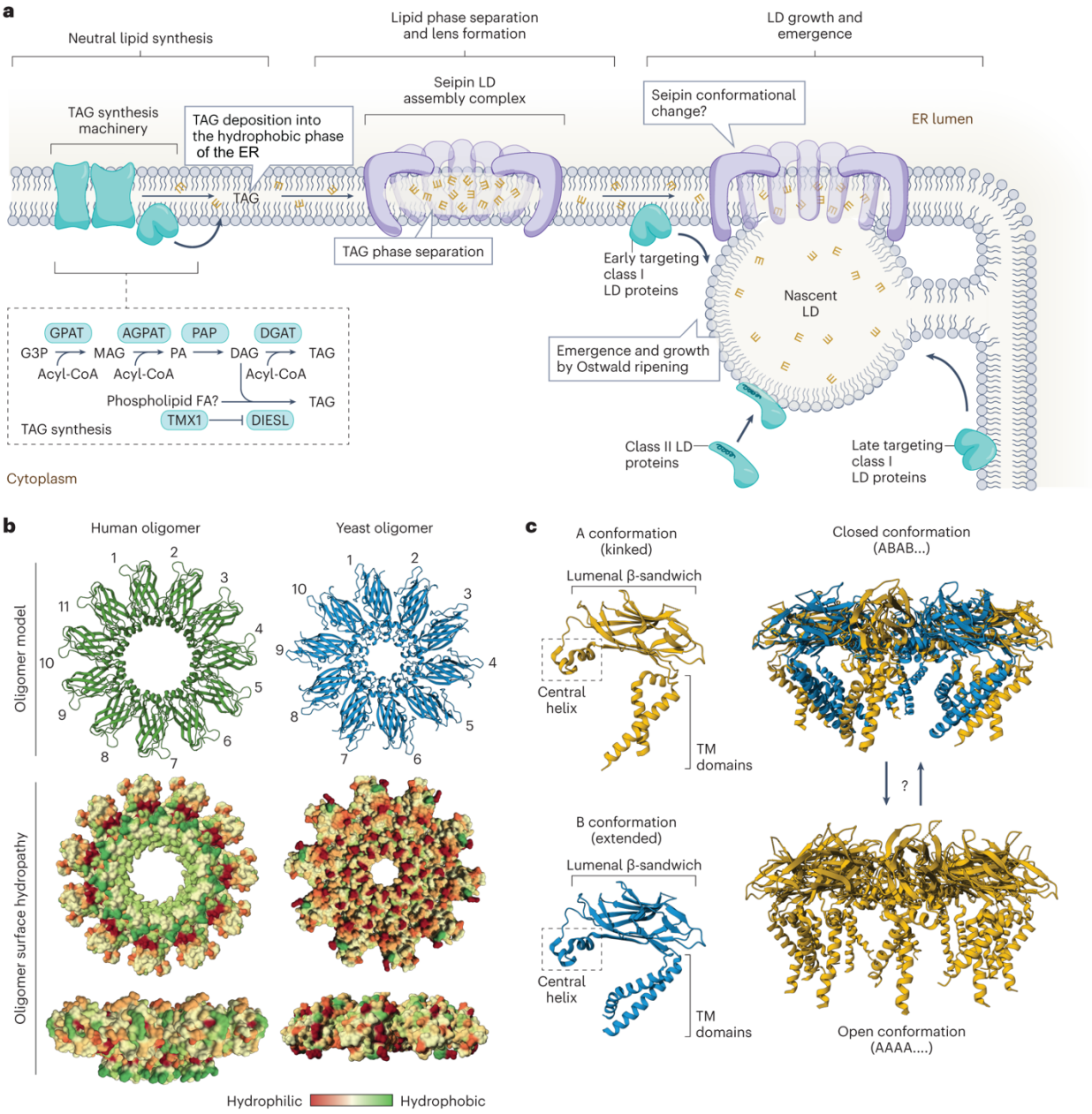

Figure 1-2: ER neutral lipid flux and LD biogenesis.
A) LD biogenesis occurs through a series of steps involving (1) the deposition of neutral lipids (for example, TAG) within the ER bilayer, (2) seipin-regulated TAG phase separation into neutral lipid lenses and (3) the emergence of the LD from the cytosolic leaflet and LD growth by Ostwald ripening. Class I LD proteins insert into the ER and traffic to LDs through lateral diffusion along membrane continuities. Early class I LD proteins traffic to nascent LDs at sites of LD biogenesis marked by the seipin LD assembly complex. Late class I LD proteins are excluded by seipin from trafficking to nascent LDs, and instead traffic across separate membrane bridges that form at specialized ER exit sites. Class II LD proteins are synthesized on cytosolic ribosomes and insert post-translationally into LDs. These proteins typically contain an amphipathic helix that is

important for recognizing and inserting into unique phospholipid packing defects in the bounding LD monolayer. B) Human and yeast seipin organize into homo-oligomeric ring structures with 11 and 10 subunits, respectively. Human seipin contains a lumenal β-sandwich domain with a hydrophobic helix that extends towards the center of the ring and likely embeds into the membrane. Molecular dynamics simulations indicate that the lumenal ring of human seipin is sufficient to promote TAG aggregation. C) Yeast seipin structures containing the transmembrane domains indicate two conformations, a kinked (A) and extended (B) conformation, and suggest that seipin functions as a flexible cage-like structure that opens towards the cytosol during LD biogenesis. The complex consisting of the alternating kinked and extended conformation (ABAB…) forms a closed conformation that may be involved in the initial phase separation of the nascent lipid lens. The complex consisting uniformly of the kinked conformation (AAAA…) forms an open conformation that may be involved in LD emergence and growth. AGPAT, acyl CoA:acylglycerol phosphate acyltransferases; G3P, glycerol-3-phosphate; PA, phosphatidic acid; PAP, phosphatidic acid phosphatase. This figure was generated using the following Protein Data Bank (PDB) entries: CryoEM human seipin (6DS5); CryoEM yeast seipin (7OXP); CryoEM yeast seipin (7RSL).

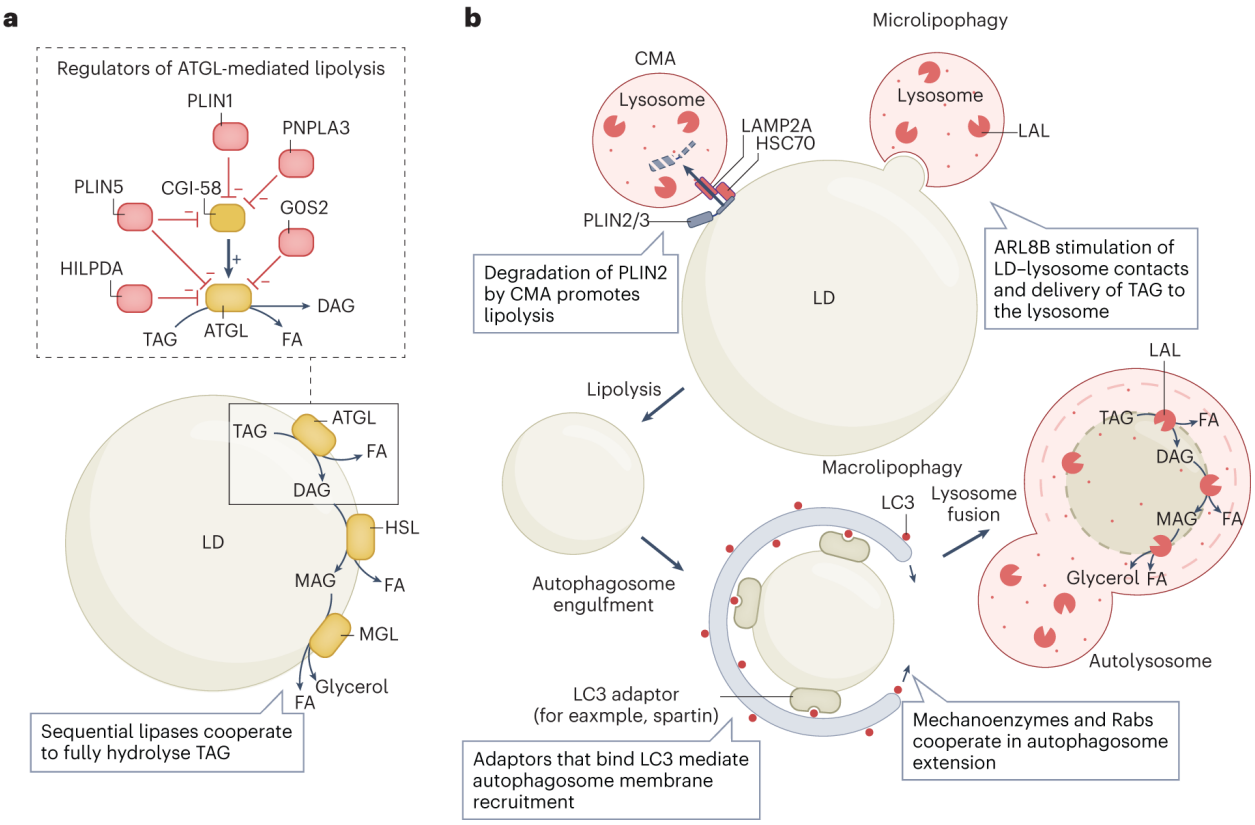

Figure 1-3: Accessing stored lipids: lipolysis and lipophagy. A) Lipolytic breakdown of TAGs stored in LDs occurs through the sequential actions of LD-localized lipases—ATGL, HSL and MGL. ATGL is the rate-limiting enzyme in this pathway and is subject to several mechanisms of regulation (shown in the inset box). CGI-58 is an ATGL binding partner that increases ATGL activity. The association of CGI-58 is governed by multiple regulatory proteins. The positive or negative regulatory effect is indicated, including direct ATGL inhibitors (G0S2 and HILPDA) and inhibitors that act by preventing the interaction of ATGL and CGI-58 (PLIN1, PLIN2 and PNPLA3). B) Macrolipophagy and microlipophagy provide two pathways to deliver LDs, or portions of LDs, to lysosomes for breakdown. LAL mediates the hydrolysis of lipids, including both TAGs and SEs. In macrolipophagy, CMA degradation of PLIN2 and PLIN3 promotes lipolysis, reducing the size of LDs. Autophagy receptors mediate the recruitment to LDs of LC3-decorated autophagic membranes, which are subsequently extended to fully envelope the LD. The autophagosome fuses with lysosomes to generate an autolysosome and enable the degradation of the LD. By contrast, microlipophagy mediates the direct delivery of a portion of the LD to the lysosome for degradation, independent of canonical autophagy machinery.

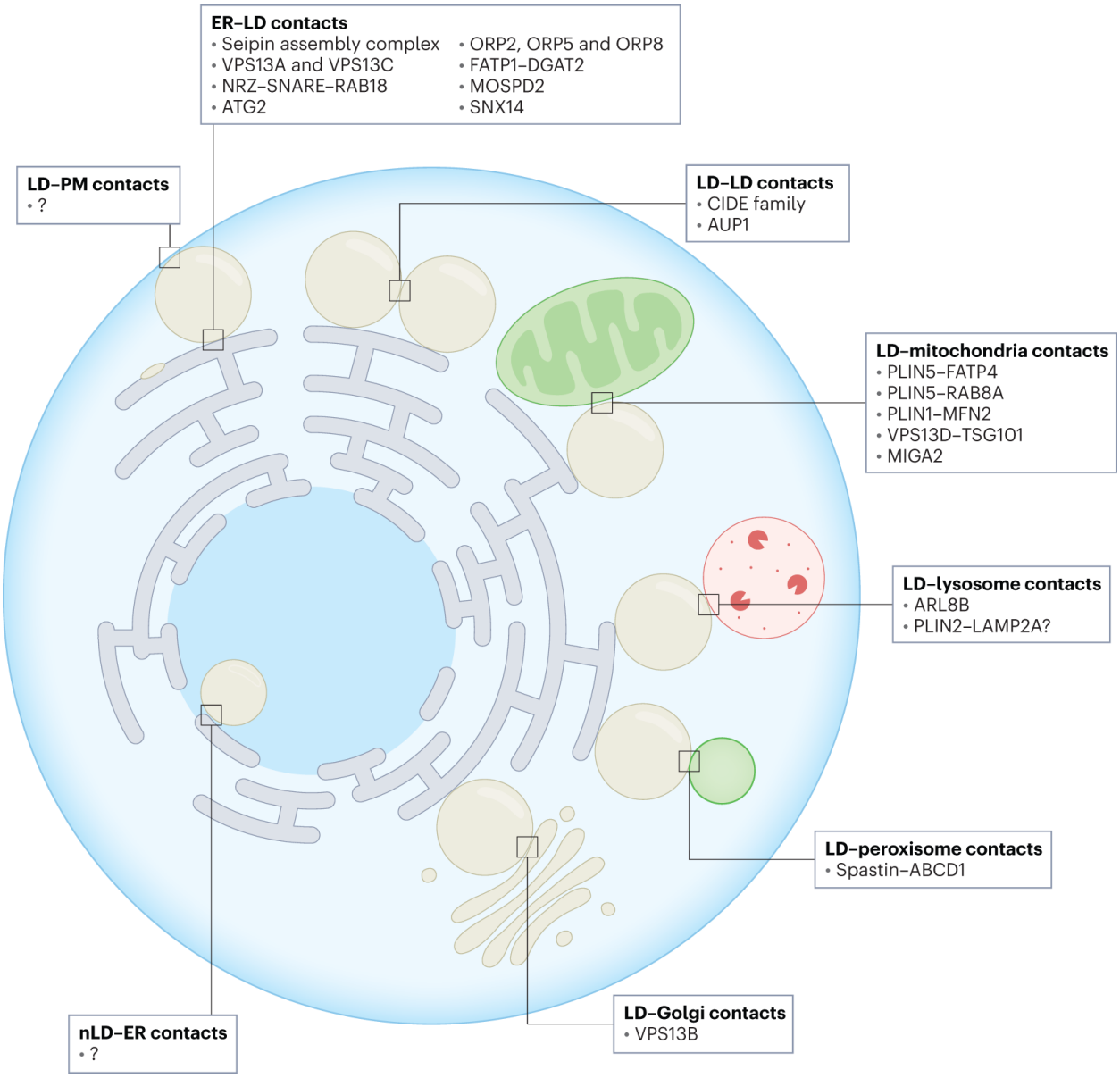

Figure 1-4: Tethers and lipid transfer proteins at LD membrane contact sites.
LDs form MCSs with virtually all organelles in the cell, providing sites for the organization of protein complexes and the transfer of lipids by LTPs. The membranes at these sites are held in close apposition by protein tethers. Tether and LTPs present at different LD MCSs are listed. Although LDs have been observed to make contacts with the plasma membrane (PM), the proteins present in these contact sites are not known. In Drosophila, snazarus localizes to LD–plasma membrane contacts and it is possible that snazarus orthologues may have similar roles in mammalian cells. Nuclear LDs (nLDs) are present in some cell types, but little is known about their membrane contact sites.

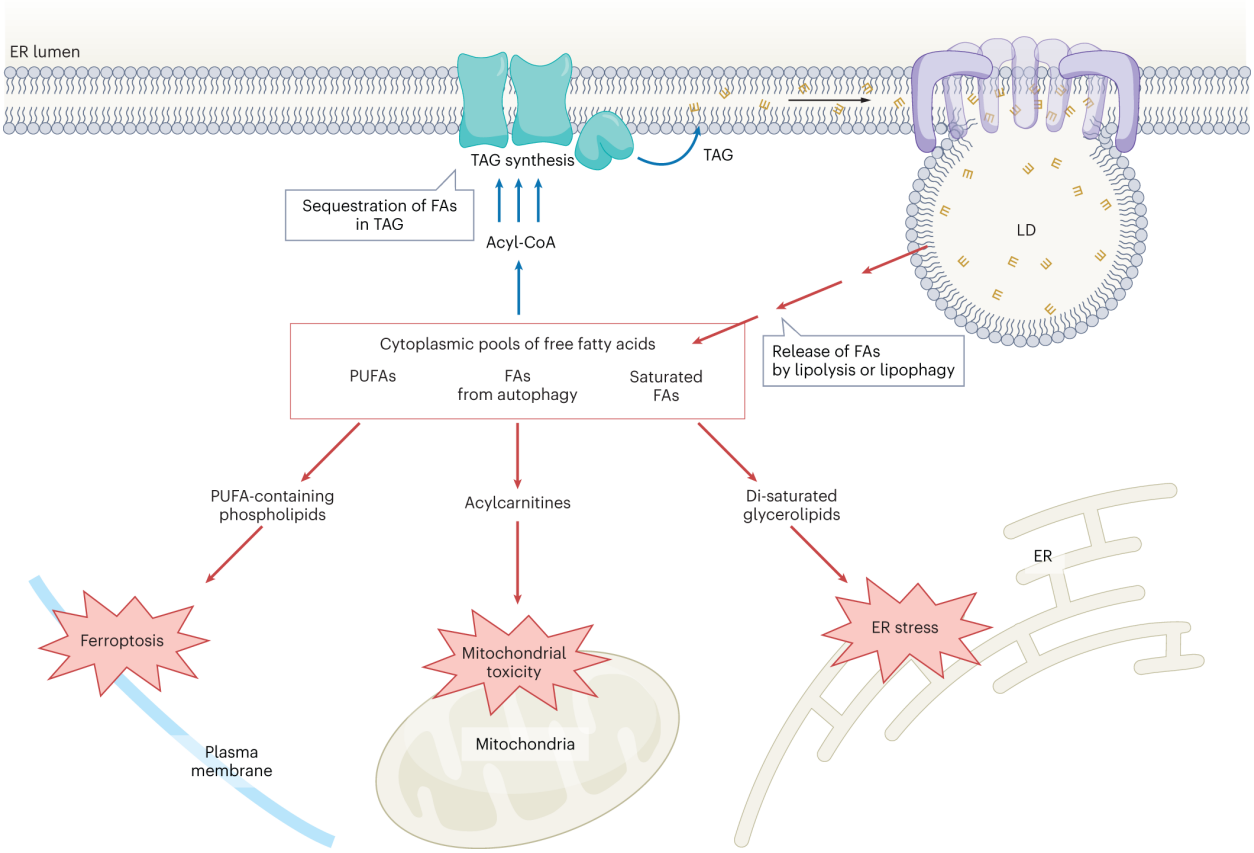

Figure 1-5: Lipid flux and lipotoxicity.
In addition to their canonical role in cellular energy homeostasis, LDs act as a lipid buffering system that prevents lipotoxicity. Various types of FA can be esterified and safely stored as TAGs within LDs. Excessively high amounts of FAs can elicit different manifestations of lipotoxicity, either by acting as direct membrane detergents or by being incorporated into specific lipids that cause dysfunction at high amounts. PUFA-containing phospholipids are prone to oxidation and sensitize cells to lipid peroxidation and ferroptosis. The incorporation of saturated FAs (such as palmitate) into glycerolipids can lead to high amounts of di-saturated glycerolipids that may alter membrane fluidity, inducing ER stress and apoptosis. FAs released during the autophagic breakdown of membranous organelles, such as during nutrient deprivation, can accumulate as acylcarnitine and induce mitochondrial dysfunction. Under certain conditions, lipolysis or lipophagy could lead to excessive free FAs that contribute to lipotoxicity.

Chapter 2: CLCC1 promotes hepatic neutral lipid flux and nuclear pore complex assembly

Contents in this chapter are modified from the following manuscript (under revision):

Mathiowetz, A. M., Meymand, E. S., Deol, K. K., Parlakgül, G., Lange, M., Pang, S. P., Roberts, M. A., Torres, E. F., Jorgens, D. M., Zalpuri, R., Kang, M., Boone, C., Zhang, Y., Morgens, D. W., Tso, E., Zhou, Y., Talukdar, S., Levine, T. P., Ku, G., Arruda, A. P., & Olzmann, J. A. CLCC1 promotes hepatic neutral lipid flux and nuclear pore complex biogenesis. *BioRxiv* (2024). doi:10.1101/2024.06.07.597858.

2.1 Introduction

Lipid droplets (LDs) are the primary lipid storage organelle in cells[1,147]. LDs are derived from the endoplasmic reticulum (ER) through a process involving neutral lipid synthesis and deposition between the leaflets of the ER bilayer, neutral lipid phase separation facilitated by LD assembly complexes, and LD emergence into the cytoplasm from the outer leaflet of the ER bilayer[1,147]. Mature LDs consist of a neutral lipid core that is encircled by a phospholipid monolayer decorated with integral and peripheral proteins[1,147]. LDs act as a dynamic cellular repository of lipids that can be formed *de novo* and that can be rapidly broken down to release stored lipids[1,147]. LD degradation provides substrates for b-oxidation and the generation of energy or macromolecular building blocks for the biosynthesis of membranes and lipid signaling molecules[1,147]. LDs also suppress lipotoxicity by sequestering lipids and preventing their flux into damaging species[1,147], such as di- saturated glycerolipids that cause ER stress[119] or polyunsaturated fatty acid-containing phospholipids that are prone to oxidation[80,134]. LD dysregulation has been implicated in the pathogenesis of a wide variety of diseases, ranging from metabolic diseases to cancer and neurodegeneration[3–5].

In addition, the functions, composition, and regulation of LDs differ depending on the cell and tissue type, metabolic conditions, and fluctuations in the cellular need for lipids and energy[1,144]. The liver is a central site of lipid metabolism[3,148]. Fatty acids in liver hepatocytes may be used to generate triacylglycerol (TAG) that is stored in cytoplasmic LDs or packaged into very low-density lipoproteins (VLDLs) for secretion into circulation[3,148,149]. Altered storage and secretion of lipids can lead to the persistent buildup of hepatocyte LDs, a pathological hallmark of Metabolic dysfunction-associated fatty liver disease (MAFLD)[3,150]. An estimated 20-30% of the general population and 75-92% of morbidly obese individuals exhibit hepatic steatosis[150], and MAFLD is a risk factor for metabolic dysfunction-associated steatohepatitis (MASH), cirrhosis, and hepatocellular carcinoma[3,150]. The mechanisms that govern the storage of neutral lipids in hepatocyte LDs remain incompletely understood, and addressing this gap in knowledge is paramount to the development of new therapeutic strategies.

In the current study, we performed a series of over 20 CRISPR-Cas9 genetic screens in Huh7 hepatoma cells under different metabolic conditions, providing a compendium of genetic modifiers of lipid storage and insights into the mechanisms that govern hepatic neutral lipid flux and cellular membrane homeostasis. Analyses of the resulting chemical-genetic interactions identify CLCC1 as a strong regulator of hepatic neutral lipid storage. We further discover that CLCC1 is the human homolog of yeast Brl1p / Brr6p, two proteins implicated in membrane remodeling and fusion during nuclear pore complex assembly[151–156]. Indeed, loss of CLCC1 results in defects in nuclear pore complex assembly and in altered neutral lipid flux, leading to hepatic steatosis due to enlarged lipoproteins that fail to be secreted and accumulate in the ER lumen at the expense of cytosolic LDs. Our results demonstrate the importance of CLCC1 for the fusion of the inner and outer nuclear envelopes during nuclear pore complex assembly and neutral lipid flux in hepatocytes.

2.2 Results

2.2.1 CRISPR-Cas9 screens identify a compendium of neutral lipid storage genetic modifiers

The fluorescent dye BODIPY 493/503 concentrates in the LD neutral lipid core, enabling quantification of changes in neutral lipids sequestered in LDs by fluorescence imaging and flow cytometry (Figure 2-1A and Figure 2-S1A). To systematically identify genes involved in lipid storage, we performed a genome-wide fluorescence-activated cell sorting (FACS)-based CRISPR-Cas9 screen in Huh7 hepatoma cells using BODIPY 493/503 fluorescence as a reporter of neutral lipid storage (Figure 2-1B). Duplicate batch retest screens were subsequently performed using a custom Validation of Lipid Droplet & Metabolism (VLDM) sgRNA library (Figure 2-S1B) to increase confidence and reduce false positives and negatives (Figure 2-1C and Figure 2-S1C). These data identified 244 high confidence candidate regulators of neutral lipid storage – 192 positive and 52 negative regulators. As anticipated, the screen was enriched in genes associated with glycerolipid metabolism, including factors involved in neutral lipid synthesis (e.g., *ACSL3*, *SCD*, *CHP1*, *ACACA*, *DGAT2*, *AGPAT6*) and lipolysis (e.g., *ABHD5*, *PNPLA2*, *HILPDA*) (Figure 2-1C-D and Figure 2-S1D), consistent with the overall quality of the screens. Genes involved in other functional categories were also identified, such as the secretory pathway and protein trafficking, ubiquitination and ERAD, the mevalonate pathway, SREBP pathway, and additional processes that influence lipid metabolism (Figure 2-1C-D and Figure 2-S1D).

Most of our understanding of LD regulation is based upon studies in unperturbed and oleate-treated cells. However, the functions of LDs are influenced by diverse conditions and certain regulators are metabolic state specific[144]. To provide insights into the genetic modifiers of neutral lipid storage under different metabolic states, we performed duplicate FACS-based screens using our VLDM sgRNA library under 11 different metabolic conditions, including nutrient starvation, nutrient excess, and cell stress conditions (Figure 2-1E). Importantly, this series of 22 genetic screens generated extensive chemical-genetic interaction data that can be used to cluster genes with similar functional profiles in an unbiased manner, thereby facilitating functional predictions for novel candidate regulators (Figure 2-1F). The findings highlight the key importance of the glycerolipid metabolic pathways and identify differences in the utilization of members of enzyme families, such as the use of different *AGPAT*, *LIPN*, and *DGAT* enzymes under different conditions (Figure 2-S2A). Unbiased clustering revealed metabolic state-specific as well as core positive and negative regulators that generally reduced LDs and increased LDs, respectively, when the gene was depleted (Figure 2-1F and Figure 2-S2B-K). Genes that are known to play similar roles were often observed to cluster together, such as *BSCL2* (also known as *seipin*) and its binding partner *TMEM159* (also known as *LDAF1* and *promethin*) (Figure 2-S2D) which participate in LD nucleation and emergence from the ER[18]. The clustered core positive regulators included genes with roles in promoting neutral lipid synthesis (e.g., *ACSL3*, *DGAT2*, *CHP1*, *AGPAT6*, *SCD*), sterol ester synthesis (e.g., *SOAT1*), SREBP signaling (e.g., *SCAP*, *MBTPS2*), and LD stabilization (e.g., *PLIN2*) (Figure 2-S1F). Conversely, the clustered core negative regulators included genes with roles in neutral lipid breakdown (e.g., *ABHD5*, *PNPLA2*), cholesterol ester

breakdown (e.g., *NCEH1*), ER-associated degradation (ERAD) (e.g., *MARCH6*, *UBE2J2*), and lipoprotein secretion (e.g., *apoB*) (Figure 2-1F). These data establish a phenotypic-rich compendium of genetic modifiers of neutral lipid storage under multiple metabolic conditions. To promote accessibility and analysis, the data from these screens will be deposited in CRISPRlipid[144], an online community driven data commons for functional genomics data related to lipid biology.

2.2.2 Enlarged lipid droplets accumulate in cells lacking CLCC1

Many candidate regulators with no known roles in lipid metabolism and LD biology were identified (Figure 2-1F). CLIC-like chloride channel 1 (CLCC1) emerged as a priority candidate for characterization because: *1*) it clustered strongly with well-known lipolysis regulators *ABHD5* and *PNPLA2* (Figure 2-1F and Figure 2-2A), *2*) genetic variants in *CLCC1* in humans are associated with alterations in serum lipids (Figure 2-S3), and *3*) it was one of the most enriched genes among the core negative regulators with strong enrichment of multiple sgRNAs targeting *CLCC1* across several conditions (Figure 2-1F and Figure 2-S4A). *CLCC1* Huh7 knockout ($CLCC1^{KO}$) cells generated with two independent sgRNAs increased lipid storage under multiple conditions (Figure 2-S4B). LDs in the $CLCC1^{KO}$ cells were larger in size and they were stable following treatment with the acyl-CoA synthetase inhibitor triacsin C, which triggers the lipolytic consumption of LDs in control cells (Figure 2-2B-D). We also observed larger LDs in the $CLCC1^{KO}$ cells by transmission electron microscopy (TEM) (Figure 2-2E). The $CLCC1^{KO}$ cells had a ~1.5-2-fold increase in TAG by thin layer chromatography (TLC), but no significant change in cholesterol esters (CE) (Figure 2-2F). Employing a pulse chase assay that uses a fluorescently labeled fatty acid[109,144], we found that loss of CLCC1 increased TAG biosynthesis and decreased TAG breakdown (Figure 2-S4C-D), suggesting that alterations of multiple aspects of neutral lipid metabolism contribute to the buildup of enlarged LDs in $CLCC1^{KO}$ cells.

2.2.3 Deletion of *Clcc1* in mouse liver causes steatosis

Clcc1 deletion is embryonic lethal in mice[157]. A spontaneous recessive mutation in *Clcc1* that disrupts the mouse *Clcc1* gene causes ER stress and cerebellar degeneration[158] and the conditional knockout of mouse *Clcc1* in motor neurons also leads to ER stress and neurodegeneration[159]. However, the role of *Clcc1* in most tissues is unknown. To determine the physiological importance of liver *Clcc1*, floxed *Clcc1* mice were injected with either AAV8-Cre to knockout *Clcc1* in hepatocytes ($Clcc1^{HepKO}$) or with AAV8-GFP as a control. Four weeks after the injection, we confirmed depletion of Clcc1 protein by immunoblotting (Figure 2-2G). $Clcc1^{HepKO}$ mice had a ~2-fold increase in liver weight/body weight ratio compared to control mice (Figure 2-2H), but no change in overall body weight (Figure 2-2I). Gross analysis of liver pathology revealed enlarged, whitened livers in the $Clcc1^{HepKO}$ mice (Figure 2-2J), indicative of lipid accumulation and hepatic steatosis. Indeed, TLC indicated a dramatic increase in TAG (Figure 2-2K) and CE (Figure 2-2L), and neutral lipid accumulation in the $Clcc1^{HepKO}$ livers was evident based on H&E and oil red O staining (Figure 2-2M). EM provided additional evidence indicating the accumulation of enlarged LDs in the $Clcc1^{HepKO}$ mice (Figure 2-2N). Finally, analysis of plasma indicated a reduction in TAG and HDL in the $Clcc1^{HepKO}$ mice (Figure 2-2O), indicating a defect in hepatic lipid secretion. Despite the loss of Clcc1 for only four weeks

and the lack of a nutritional challenge (e.g., high fat diet), an increase in AST, a marker of liver damage, was observed in the Clcc1^{HepKO} mice (Figure 2-2O). ALT was also measured, but there was no significant change (Figure 2-S4E). These findings demonstrate that Clcc1 plays an important role in regulating hepatic lipid storage and protecting hepatocytes from lipotoxicity.

Interestingly, *Clcc1* depletion also changes the abundance of many lipid species in the liver and plasma (Figure 2-S5C-E). Though *Clcc1* was only partially knocked down in this experiment (Figure 2-S5A), there was high significance and correlation between experiments (Figure 2-S5B). Many triglyceride and phosphatidylcholine species were upregulated in Clcc1^{HepKD} mouse liver, especially highly unsaturated triglycerides (Figure 2-S5C-D). Surprisingly, WT mice on a high fat and high sugar (GAN) diet accumulated lowly saturated triglycerides such as oleate (Figure 2-S5C-D), indicating a specificity for PUFAs that is Clcc1-specific (Figure 2-S5C-D). Though overall TAG levels were decreased in Clcc1^{HepKD} plasma (Figure 2-2O), this appears to be relegated to lowly unsaturated fatty acids, and highly saturated TAGs were present at a similar abundance to WT mice (Figure 2-S5C,E). There was no such fatty acid specificity in phospholipids (Figure 2-S5C-D).

2.2.4 Lipid droplets in hepatocytes lacking CLCC1 are trapped within the ER lumen

As a first step towards understanding the mechanistic basis for LD accumulation in CLCC1^{KO} cells, we performed a pairwise comparison of our previously published PLIN2-GFP[144] and current BODIPY 493/503 batch retest screens using the focused LD and metabolism-targeted sgRNA libraries (Figure 2-3A). As anticipated, there was a strong positive correlation in genetic modifiers identified in these two screens[144,160]. However, CLCC1 was an outlier, with CLCC1 sgRNAs associated with an increase in neutral lipids, but a counter intuitive decrease in PLIN2-GFP (Figure 2-3A). This was surprising because the perilipin family of LD “coat” proteins are constitutively present on LDs and the levels of PLIN2 generally correlate with LD abundance[161]. Moreover, PLIN2-GFP is typically considered to be an obligate LD protein, and its degradation by the proteasome is induced under low LD conditions[120,144,162,163]. Western blotting confirmed that endogenous PLIN2 protein levels were undetectable in CLCC1^{KO} cells (Figure 2-3B). Incubation with the proteasome inhibitor MG132 rescued PLIN2 levels in the CLCC1^{KO} cells, indicating that despite high amounts of LDs, PLIN2 is being degraded post-translationally by the proteasome (Figure 2-S6A). Immunofluorescence staining of PLIN2 also revealed a strong reduction in PLIN2-positive LDs in the CLCC1^{KO} cells, with the large LDs appearing to be completely devoid of any PLIN2 staining (Figure 2-3C). Importantly, overexpression of CLCC1 rescued the PLIN2-GFP localization to LDs (Figure 2-S6B) and the reduction in PLIN2-GFP levels (Figure 2-S6C) in CLCC1^{KO} cells, consistent with the altered PLIN2 and LDs reflecting on-target depletion of *CLCC1*. Furthermore, proteomics analyses of LD-enriched buoyant fractions validated the reduction in PLIN2 on LDs and revealed the reduction in numerous well known LD proteins, such as ATGL, ABHD5, FSP1, LDAH, PNPLA3, and others (Figure 2-3D). These results indicate that although CLCC1^{KO} cells appear to accumulate large LDs, the LDs lack canonical LD proteins. To examine the generalizability of this phenotype, we generated knock out CLCC1 HepG2 (hepatoma), U-2 OS (osteosarcoma), and LX-2 (stellate) cell lines that were previously genetically

engineered to express PLIN2 fused to GFP (i.e., PLIN2-GFP) at is genomic locus[144]. As in the Huh7 CLCC1^{KO} cells, HepG2 CLCC1^{KO} cells exhibited enlarged PLIN2-negative LDs (Figure 2-S6D), a reduction in PLIN2-GFP levels (Figure 2-S6E), and an increase in monodansylpentane (i.e., neutral lipid) staining (Figure 2-S6E). In contrast, LDs in the U-2 OS and LX-2 CLCC1^{KO} cells were of the expected size and were PLIN2-positive (Figure 2-S6F,H), and PLIN2 and neutral lipid amounts were also unchanged (Figure 2- S6G,I). These data suggest that the observed LD phenotypes are specific to hepatocytes.

One potential mechanism that could explain the reduction of LD proteins is that the LD surface is somehow occluded, preventing protein trafficking to or insertion into the LD bounding monolayer. For example, tight organelle contacts can exclude proteins[164]. We therefore examined the distribution of several organelles and their relationship with LDs in the CLCC1^{KO} cells by immunofluorescence. The distribution and morphology of the Golgi, lysosomes, and mitochondria were mostly unchanged (Figure 2-S7A). However, the ER (marked by BFP-KDEL) exhibited an atypical morphology (Figure 2-S7A-B). Instead of sheets and tubules, strong ER staining was observed encircling the enlarged LDs in CLCC1^{KO} cells (Figure 2-S7A-B). To further understand the relationship between the ER and LDs we performed EM. Typical ER-LD contact sites were observed between the ER and LDs in control cells (Figure 2-3E). In the CLCC1^{KO} cells, LDs were surrounded by a bilayer membrane (Figure 2-3E). The monolayer of the LD was distinguishable from the bounding bilayer (Figure 2-3E). In some cases, we observed an ER sheet that was connected to a bilayer encircling one or more LDs (Figure 2-3E), indicating that LDs are present within the ER lumen instead of the cytoplasm. We observed a similar relationship in EM images of liver tissue from the Clcc1^{HepKO} mice, with LDs inside an encapsulating bilayer membrane (Figure 2-3F). These data indicate that LDs in CLCC1^{KO} cells are devoid of cytoplasmic LD proteins because they emerged into the ER lumen and are spatially segregated from cytoplasmic LD proteins. These findings further suggest that the LDs in CLCC1^{KO} cells are resistant to lipolysis because they are within the ER, rendering them inaccessible to ATGL and other cytoplasmic lipases.

2.2.5 Lipid droplets in CLCC1^{KO} cells are MTP-dependent

The accumulation of PLIN2-negative LDs in the ER lumen was specific to hepatocyte-derived cell types (Figure 2-3A-F and Figure 2-S6D-I), suggesting that a distinct property of hepatocyte lipid metabolism is important. A unique aspect of hepatocytes is their ability to form and secrete lipoproteins (i.e., VLDLs) to provide lipids to other tissues. Similar to LDs, lipoproteins consist of a neutral lipid core encircled by a phospholipid membrane decorated with regulatory proteins such as apolipoprotein B (apoB). The initial formation of lipoproteins involves microsomal triglyceride transfer protein (MTP)-mediated transfer of TAG into the ER lumen[149]. Incubation of CLCC1^{KO} cells with the MTP inhibitor CP-346086 rescued the biogenesis of PLIN2-positive LDs (Figure 2-3G,H) and the amount of neutral lipids (marked by monodansylpentane) (Figure 2-3I). MTP inhibitor treatment also rescued PLIN2 protein levels (Figure 2-S7C). There was no change in MTP levels in CLCC1^{KO} cells (Figure 2-S7D). In addition, we observed an increased percentage of apoB positive LDs in the CLCC1^{KO} cells (Figure 2-3J-K), though not all LDs were apoB positive. There was also an increased amount of apoB peptide counts in buoyant, LD-enriched fractions (Figure 2-3L). Consistent with the reduced HDL and TAG measured in the

mouse serum of Clcc1^{HepKO} mice (Figure 2-2O), we observed a reduction in apoB secretion into medium by CLCC1^{KO} cells (Figure 2-3M). No change in the levels of secreted albumin in medium was observed (Figure 2-S8A), suggesting that secretion is not generally disrupted. In addition, a luciferase-based assay of ER protein folding and secretion, which uses the substrate asialoglycoprotein receptor 1 (ASGR1) fused to luciferase Cluc[165,166], also showed no impairment in the CLCC1^{KO} cells (Figure 2-S8B). Together, these findings indicate that the enlarged LDs are aberrant lipoproteins that exhibit reduced secretion. The near complete lack of cytoplasmic PLIN2-positive LDs suggests a profound shift in neutral lipid flux away from cytoplasmic LDs towards lumenal MTP-dependent lipoproteins. It is noteworthy that VLDLs typically have a diameter of ~50-80nm, whereas the mean diameter of the lumenal LDs in the CLCC1^{KO} cells is ~1.84 μm. Thus, the lipoproteins that accumulate in the CLCC1^{KO} cells are exceptionally large in volume compared to a normally secreted VLDL particle (>10,000-fold larger).

2.2.6 CLCC1 and its relationship with ER stress and ER scramblases

Loss of CLCC1 has been associated with an increase in ER stress[158,159]. However, there was no increase in the mRNA transcripts of a variety of common ER stress targets (Figure 2-S8C) or the protein levels of the ER chaperone grp78/BiP (Figure 2-S8D) in CLCC1^{KO} cells. Moreover, although induction of ER stress by treatment with tunicamycin and thapsigargin altered LD distribution, the LDs remained PLIN2-GFP positive (Figure 2-S8E). These findings indicate that ER stress is not necessary for the lumenal LDs CLCC1^{KO} cells nor is it sufficient to trigger the accumulation of lumenal LDs. *CLCC1* was the only gene that exhibited an increase in neutral lipid amount and a decrease in PLIN2-GFP in the pairwise comparison of our batch retest screens (Figure 2-3A). Broader examination of our genome-wide screens revealed that depletion of *TMEM41B* was also associated with an increase in neutral lipids and a decrease in PLIN2-GFP (Figure 2-S9A). TMEM41B is an ER scramblase that interacts with apoB and regulates hepatic lipoprotein secretion[33]. *TMEM41B* KO in mice reduces lipoprotein secretion and results in severe hepatic steatosis and the accumulation of LDs encapsulated by ER membranes[33]. The KO of a second ER scramblase, VMP1, causes hepatic steatosis and the buildup of PLIN2-negative LDs, similarly suggesting an association between phospholipid scrambling and ER lumenal LDs in hepatocytes[30,32]. However, in our screens in Huh7 cells, loss of *VMP1* was associated with a reduction in PLIN2-GFP but no change in neutral lipid staining (Figure 2-S9A). There was no change in the levels of TMEM41B or VMP1 in CLCC1^{KO} cells (Figure 2-S9B). To explore the relationship of CLCC1 and ER scramblases, we generated *TMEM41B* and *VMP1* KO Huh7 cells (Figure 2-S9C,D). LDs were PLIN2 positive (i.e., cytoplasmic) in the VMP1^{KO} cells (Figure 2-S9E). A portion of LDs in TMEM41B^{KO} cells were enlarged and PLIN2 negative (Figure 2-S9E), consistent with an ER lumenal localization. However, in contrast to CLCC1^{KO} cells, TMEM41B^{KO} cells exhibited PLIN2 crescent staining (Figure 2-S9E), which suggests that a fraction of LDs in the TMEM41B^{KO} cells are trapped in the membrane with half of the LD facing the cytoplasm and the other half the ER lumen. In addition, although MTP inhibition completely rescued LD cytoplasmic emergence in the CLCC1^{KO} cells (Figure 2-3G,H), MTP inhibition only had a partial effect on TMEM41B^{KO} cells and the effect was not significant (Figure 2-S9F,G). Finally, overexpression of either TMEM41B or VMP1 in CLCC1^{KO} cells had no effect on the amount of PLIN2-negative and -positive LDs (Figure

2-S10A-C). These data indicate that while there are similarities in the phenotypes and a potential functional relationship, dysregulation of ER scramblases alone was not sufficient to account for the altered neutral lipid flux in the CLCC1^{KO} cells.

2.2.7 CLCC1 is structurally homologous to yeast Brl1p / Brr6p

CLCC1 was first identified through a series of blast searches using a partial sequence of a yeast chloride channel Mid-1[167]. It was noted that CLCC1 exhibits no overall sequence similarity with Mid-1 and no similarity with known channel families[167]. There was, however, a short motif in a CLCC1 transmembrane domain that was partially present in the CLIC family of chloride channels, leading to the naming of CLCC1 initially as Mid-1-related chloride channel (MCLC) and eventually as CLCC1[167]. Altered chloride conductance in ER microsomes isolated from cells overexpressing CLCC1 has been observed[159,167], but direct evidence for ion conductance using purified CLCC1 is lacking. Moreover, the predicted alpha-fold structure of CLCC1 is considerably different from canonical CLIC chloride channels (Figure 2-S11A-B), suggesting that if CLCC1 conducts chloride it would be through a novel mechanism. Given these data, we considered the possibility that CLCC1 may have alternative biochemical functions. An HHpred search for remote homologs revealed a strong relationship between amino acids 204-378 of CLCC1 with the yeast paralogs Brl1p (probability score 94%) and Brr6p (probability score 86%) (Figure 2-4A and Figure 2-S12). This is based on both sequence and structural homology. Indeed, the alpha-fold predicted structures showed a homology domain with very similar features (Figure 2-4B). Both predicted structures contain an elongated transmembrane helix (TMH) within a portion of a helix that enters deep into the lumen, a sharp turn followed by a short helix (knuckle region), a perpendicular amphipathic helix (AH), and another TMH. These features are absolutely conserved in both families. The knuckle region of Brl1p and Brr6p contains two cysteine pairs that stabilize the structure with intramolecular disulfide bonds[154], and CLCC1 contains one cysteine pair. Co-immunoprecipitation data with differentially tagged CLCC1 indicated that CLCC1 self-associates[159], possibly forming a dimer or higher order oligomer. Indeed, proteome-scale predictions of homo-oligomeric assemblies predict a CLCC1 dimer that is stabilized by intermolecular disulfides in a lumenal N-terminal domain not shared with Brl1p / Brr6p[36] (Figure 2-4C and Figure 2-S13A). Consistent with this model, we find that in the absence of reducing agent, CLCC1 migrates as a dimer (Figure 2-4D). The addition of DTT yields the expected CLCC1 monomer (Figure 2-4D). Furthermore, analysis of the CLCC1 Brl1p homology domain using ColabFold suggests the possibility of larger CLCC1 oligomers that form a ring structure (Figure 2-S13B). The same is also the case for Brl1p and Brr6p (Figure 2-S13C).

2.2.8 CLCC1 plays a critical role in nuclear pore assembly

Brl1p and Brr6p function in the assembly of nuclear pore complexes, which are large nuclear envelope (NE) protein complexes that perforate the inner and outer NEs to enable regulated exchange between the nucleus and cytoplasm[151–156,156]. Although the detailed architecture of nuclear pore complexes has been determined[168], their mechanisms of biogenesis and insertion into membranes remains incompletely understood. *BRL1* and *BRR6* are essential, and conditional disruptions result in nuclear membrane herniations (also referred to as nuclear blebs) indicative of disruptions in nuclear pore complex

insertion, as well as altered membrane composition and synthetic interactions with lipid metabolic pathways[152–156,156]. It is noteworthy that there is precedence for factors that have roles in both nuclear pore complex assembly and hepatic neutral lipid storage. The ER lumenal AAA ATPase torsinA and its cofactors Lull1 and Lap1 promote nuclear pore complex biogenesis, and loss of these factors results in nuclear membrane herniations[38]. In addition, the conditional loss of torsinA, Lull1, or Lap1 in mouse liver causes hepatic steatosis and reduced lipoprotein secretion[169,170].

Given the structural homology between CLCC1 with yeast Brl1p / Brr6p, we examined a potential relationship of CLCC1 with nuclear structure, including nuclear morphology and the integrity of the NE in CLCC1^{KO} cells. Interestingly, co-essentiality analyses[171] indicate a functional relationship between CLCC1 and nuclear pore complex genes (Figure 2-S14A). In addition, proteomic analyses of isolated organelles[172] indicate that CLCC1 is present in the ER, with similar localization profiles as the torsin activators Lap1 (also known as TOR1AIP1) and Lull1 (also known as TOR1AIP2) as well as the scramblases TMEM41B and VMP1 (Figure 2-S14B). Consistent with these data and past studies[157,158], fluorescence imaging revealed that endogenous CLCC1 localized to both the ER and NE (Figure 2-4E). Fluorescence imaging of CLCC1^{KO} cells indicated alterations in lamin A/C staining and nuclear morphology (Figure 2-4F and Figure 2-S15). Importantly, EM showed nuclear membrane herniations in the cultured CLCC1^{KO} cells (Figure 2-4G), similar to those found following depletion of Brl1p and Brl6p in yeast[151–156]. NE herniations occur when there is a failure of inner and outer NE fusion during nuclear pore complex insertion, resulting in membrane protrusions that contain extruded nucleoplasm. Consistent with this structure, puncta of GFP-tagged myeloid leukemia factor 2 (MLF2), a marker of NE herniations that accumulates in the nucleoplasmic interior of the NE herniation[172], decorated the NE of CLCC1^{KO} cells but not control cells (Figure 2-4H). Similar to our cultured cells, extensive NE herniations were also observed in the liver tissue of CLCC1^{HepKO} (Figure 2-4I). KO of *CLCC1* in the osteosarcoma cell line U-2 OS led to the accumulation of NE herniations (Figure 2-S15B), despite the absence of lumenal LDs in this cell line. Furthermore, although MTP inhibition rescues LD biogenesis (Figure 2-3G-I), MTP inhibition had no effect on the NE herniations in the CLCC1^{KO} cells (Figure 2-S15C,D). We also observed NE herniations in the TMEM41B^{KO} cells, though they were less abundant than in the CLCC1^{KO} cells (Figure 2-S15E,F). Together, these data indicate that while the effect of *CLCC1* KO on neutral lipid flux is restricted to hepatocytes, which secrete lipoproteins, there is a more generalizable role for CLCC1 in nuclear pore complex assembly across multiple cell lines. These data also indicate that the NE herniations are not downstream of the defects in neutral lipid flux. To characterize the impact of Clcc1 on organelle architecture, we performed focused ion beam scanning EM (FIB-SEM) analyses of liver tissue from control and Clcc1^{HepKO} mice (Figure 4J-L and Figure 2-S16A,B). As anticipated, this analysis revealed the accumulation of numerous enlarged LDs that occupied a large percentage of the cell volume, at the expense of other organelles (Figure 2-4J and Figure 2-S16C). One of the most remarkable phenotypes in the Clcc1^{HepKO} liver tissue was the presence of extensive NE herniations decorating the majority of the nucleus (Figure 4K,L and Figure 2-S16D). Most of the nuclear NE herniations are connected to the NE, often by a thin membrane stalk (Figure 2-4K-L). A small subset of blebs was not observed to have a NE connection, perhaps indicating

shedding of the bleb into the cytoplasm (Figure 2-4L). We also observed large indentations in the nucleus that were generated by juxtanuclear LDs pressing into the nucleus and that had reduced of amounts NE herniations (Figure 2-4L and Figure 2-S16D). Together, our findings implicate CLCC1 as the Brl1p / Brr6p human homolog that promotes nuclear pore complex assembly.

2.3 Discussion

In the current study, we performed a series of CRISPR-Cas9 screens under diverse metabolic conditions, establishing a phenotypically rich compendium of hepatic neutral lipid storage genetic modifiers. The chemical-genetic interactions present in our compendium of lipid storage regulators identified CLCC1 as an important mediator of lipid storage. Indeed, we find that loss of CLCC1 results in the accumulation of LDs and severe hepatic steatosis in mice. The lumenal location of LDs, requirement for MTP, and immunostaining with apoB suggest that these LDs are aberrant lipoproteins. It is noteworthy that these lumenal LDs accumulate at the expense of cytoplasmic LDs, indicating that loss of CLCC1 causes a profound shift in ER neutral lipid flux.

We identify a role for CLCC1 in nuclear pore complex assembly (Figure 2-5). In metazoan cells with open mitosis, the NE disassembles to enable chromosome segregation and then reassembles around chromatin[151]. Cells that employ open mitosis form nuclear pore complexes through two mechanisms, either by forming nuclear pore complexes on membranes associating with chromatin prior to the reformation of a sealed NE or through inside-out insertion of the nuclear pore complex into the intact NE during interphase[151]. The inside-out insertion mechanism is similar to the sole mechanism of nuclear pore complex biogenesis employed by organisms with closed mitosis, such as yeast[151]. This process involves the initial insertion of a set of nuclear pore complex subunits into the inner NE, causing the NE to dimple and thereby reducing the distance between the inner and outer NE membranes[151]. Through a poorly understood process, the inner and outer nuclear membranes fuse, perforating the NE and enabling the completion of a mature nuclear pore complex[151]. The discovery of Brl1p, Brr6p, and their binding partner Apq12p as NE assembly factors in yeast was an important breakthrough[152]. However, traditional BLAST searches failed to identify a metazoan homolog of these proteins, leading to the proposal that this mechanism was restricted to organisms with closed mitosis. How nuclear membrane fusion during nuclear pore complex insertion occurs in metazoan cells has remained a mystery. Our data solve this mystery and implicate CLCC1 as the long sought Brl1p / Brr6p human homolog. This conclusion is supported by sequence conservation and structural homology in terms of multiple features, as well as evidence of shared functions in nuclear pore complex assembly. Indeed, similar to loss of Brl1p and Brr6p, *CLCC1* KO results in nuclear membrane herniations, reflecting a failure in inner and outer nuclear envelope fusion during nuclear pore complex biogenesis. The integral membrane portion of CLCC1 and Brl1p / Brr6p (TMH1-Knuckle-AH-TMH2) is a conserved domain. We propose the name ‘NPC-biogenesis "h"-shaped (Nbh) domain’, based on the shared functions and shape which is reminiscent of a lowercase “h” (Figure 2-4A). One conserved feature of Nbh domains is the separation of TMH1 and TMH2 by the lumenal AH, which leads to the TMHs being unconstrained by each other, so that they

need not be parallel. This allows Nbh proteins to reside in curved membranes. A second feature is that all of TMH1, AH and TMH2 are strongly predicted by Alphafold Multimer [and similar algorithms - same results from DMFold and Multifold] to contain extensive interfaces that oligomerize side-by-side. Finally, the whole domain has a triangular cross-section, as shown by predicted dimers with the AHs pointing in different directions (Figure 2- 4B) and overall shape (Figure 2-S13A), which is the basis upon which ring oligomers can be predicted[173]. These features together provide the first explanation at a molecular/physical level for how Brl1p / Brr6p impact nuclear pore complex biogenesis, which has been missing since they were first linked genetically to this process[153,174]. Our protein structure models suggest a potential mechanism in which a CLCC1 homo-oligomer locally bends the membrane due to the TMHs positioned at increasingly extreme angles to the perpendicular, which also applies to the yeast homologs (Figure 2-S13B,C). We were able to obtain ring structures between 12-20 protomers, with the major difference being the size of the central pore (1.4-5.8nm). Determining the stoichiometry of this putative oligomer is an important research direction that could shed light on the CLCC1 mechanism of action. Prior modeling suggests the possibility of trans interactions between Brl1p and/or Brr6p on opposing inner and outer NE membranes, which is supported by a prediction of a Brl1p-Brr6p heterodimer that interact via their knuckles (Figure 2-S13D)[175]. The putative CLCC1 oligomer would be predicted to bend the membrane inward, and interactions with a second CLCC1 homo- oligomer on an opposing membrane could facilitate membrane fusion (Figure 2-S17).

Our data implicate CLCC1 in the control of neutral lipid flux and lipoprotein biogenesis (Figure 2-5). One possibility is that CLCC1 could provide a lipid salvage pathway using a similar membrane fusogenic function as in NPC assembly, but with hemifusion of the ER membrane to a lumenal LD's single leaflet. This would reconnect lumenal LDs with the inner leaflet of the ER and allow neutral lipids to regain the ability to be stored in cytosolic LDs through Ostwald ripening and emergence from the cytosolic leaflet (Figure 2-S17, bottom), a process which may require ER scramblases. Our findings, along with the emerging data examining the roles of torsinA complexes reveals a striking connection between a set of factors involved in nuclear pore complex assembly and hepatic neutral lipid flux. The precise role of torsinA in nuclear pore complex assembly and neutral lipid flux is unknown, but it is tempting to speculate that torsinA, CLCC1, and TMEM41B could function together, perhaps with CLCC1 oligomers as substrates of torsinA[169,170]. This is similar in concept to other AAA ATPases being dedicated to a very narrow range of targets, such as NSF regulation of the recycling of membrane fusogens (i.e., SNARE proteins). The similar phenotypes observed in cells lacking ER scramblases also suggests a potential functional role, such as in regulating NE membrane curvature or providing phospholipids for cytosolic LD emergence. Although many questions remain for future studies, our findings make an important advance by identifying a role for CLCC1 in hepatic neutral lipid flux and nuclear pore complex assembly.

2.4 Materials and methods

2.4.1 Cell lines and culture conditions

Huh7, U-2 OS, and HEK293T cells were cultured in DMEM containing 4.5 g/l glucose and L- glutamine (Corning) supplemented with 10% FBS (Thermo Fisher Scientific and Gemini Bio Products), penicillin, and streptomycin. HepG2 cells were cultured in RPMI 1640 medium (Gibco) containing L-glutamine supplemented with 10% FBS, penicillin, and streptomycin. All cells were maintained at 37°C and 5% CO_2. Generation of endogenously labeled PLIN2-GFP Huh7, HepG2, and U-2 OS reporter cells are detailed in Roberts et al., 2023.

2.4.2 Plasmids and cloning

All knockout cell lines (in Huh7, HepG2, and U-2 OS cells) were generated using the pMCB320 plasmid, a gift from M. Bassik (Addgene, 89359). Guide sequences for CLCC1, TMEM41B, VMP1, and safe-targets (sgSAFE #5784) were selected from the Bassik Human CRISPR Knockout Library (Addgene, 101926, 101927, 101928, 101929, 101930, 101931,101932, 101933, 101934). Guide sequences were cloned into pMCB320 using the restriction enzymes BstXI and BlpI.

For exogenous protein expression, CLCC1 (DNASU, HsCD00951632), 1X FLAG (DYKDDDDK)-tagged CLCC1, TMEM41B (DNASU, HsCD00829148), and VMP1 (DNASU, HsCD00080545) were cloned using the Gibson assembly and the Gateway system (Thermo Fisher, 11791020) in a pLenti-CMV-Hygro vector (Addgene, 17454).

2.4.3 Generation of CRISPR-Cas9 genome edited cell lines

To generate lentiviral particles, lentiCas-Blast plasmid (Addgene, 52962) was co-transfected with third-generation lentiviral packaging plasmids (pMDLg/pRRE, pRSV-Rev, and pMD2.G) into HEK293T cells. Lentiviral media was collected 72 hr after transfection, passed through a 40 µm filter, and then used to infect Huh7 (wild type, PLIN2-GFP), HepG2 (wild type, PLIN2-GFP), and U-2 OS (wild type, PLIN2-GFP) cells. Cells were selected in media containing blasticidin (4 µg/ml in Huh7 and U-2 OS; 6 µg/ml in HepG2) for 5 days. Active Cas9 expression was validated by flow cytometry analysis following infection with a self-cleaving mCherry plasmid (pMCB320 containing mCherry and an sgRNA targeting the mCherry gene).

Lentiviral particles with sgRNA-containing pMCB320 plasmids were generated as described above and used to infect cells stably expressing Cas9. After 72 hr of growth, infected cells were selected in media containing puromycin (2 µg/ml in Huh7 and HepG2; 1 µg/ml in U-2 OS) until over 90% cells were mCherry positive and all uninfected control cells were dead. Huh7 $CLCC1^{KO}$ and $TMEM41B^{KO}$ clones (in wild type and PLIN2-GFP backgrounds) were isolated using serial dilutions. Knockout efficiencies were confirmed via immunoblotting.

2.4.4 Genome-wide Huh7 CRISPR-Cas9 screens

All CRISPR-Cas9 screens reported here were described previously in Roberts et al., 2023 and in Mathiowetz et al., 2023. Genome-wide CRISPR-Cas9 screens were performed

using the Bassik Human CRISPR Knockout Library. The library consists of nine sublibraries, comprising a total of 225,171 elements, including 212,821 sgRNAs targeting 20,549 genes (~10 sgRNAs per gene) and 12,350 negative-control sgRNAs. Lentiviral particles containing each sublibrary were generated as described above. Huh7 cells stably expressing Cas9 were transduced with lentiviral packaged sublibraries (one sublibrary at a time) in 8 µg/ml polybrene. After 72 hr of growth, infected cells were selected in media containing 2 µg/ml puromycin until over 90% of cells were mCherry positive (via flow cytometry). Cells were then recovered for 3-5 days in media lacking puromycin and frozen in liquid nitrogen.

For the screen, library infected cells were thawed (one sublibrary at a time) and maintained at 1000x coverage (1,000 cells per library element) in 500 cm^2 plates (about 20^6 cells per plate). Each library was passaged once before sorting. On the day of the sort, cells were dissociated using 0.25% Trypsin-EDTA (Gibco), collected by centrifugation at 300 x g for 3 min, stained with 1 µg/µL BODIPY 493/503 (Thermo Fisher, D3922) in DPBS on ice for 30 minutes, then washed 1x with DPBS. Cells were resuspended in phenol red free media (HyClone, 16777-406) supplemented with 3% FBS and 1% fatty acid-free BSA and kept on ice until FACS. Cells were sorted on a BD FACS Aria Fusion equipped with 4 Lasers (488 nm, 405 nm, 561 nm, and 640 nm). sgRNA-expressing, mCherry+ cells were gated into the brightest 30% and dimmest 30% by the 488 nm laser. Cells were sorted into 15 ml conicals containing DMEM with 4.5 g/L glucose and L-glutamine supplemented with 10% FBS. For each sort, 1000X cells were collected (500X in each gate). Sorted cells were collected and sequenced according to Mathiowetz et al., 2023.

2.4.5 Lipid Droplet and Metabolism Library CRISPR-Cas9 screens

The custom human VLDM library contains 10,550 elements, with 8,550 sgRNAs targeting 857 genes (~10 sgRNAs per gene) and 2,000 negative control sgRNAs. Guide sequences were from the Bassik Human CRISPR Knockout Library, and the library construction protocol and cell line generation were previously described.

For each screen, cells were thawed and expanded at >1000x coverage. For all screens, cells were seeded into 500 cm^2 plates at 1,000-fold library coverage. For the Huh7 metabolic state-dependent screens, cells were treated the following day with 1) no treatment, 2) 1 µg/ml triacsin C for 24 hr, 3) 100 µM oleate-BSA complex for 24 hr, 4) HBSS (Gibco, 14025092) for 24 hr, 5) 0.2% FBS-containing DMEM (serum starve) for 48 hr, 6) glucose-free DMEM (Gibco, 11966025) for 24 hr, 7) 50 µM palmitic acid for 24 hr, 8) 5 µM arachidonic acid for 24 hr, 9) 5 µg/mL tunicamycin for 24 hr, 10) 500 ng/mL LPS for 24 hr, or 11) NASH stress mix for 16 hr. NASH stress mix was defined as 10 mM glucose, 5 mM fructose, 400 µM oleic acid, 200 µM palmitic acid, 100 ng/mL LPS, and 30 ng/mL TNFα. Cells were screened by FACS as described above.

2.4.6 CRISPR screen data analysis

Sequence reads were aligned to the sgRNA reference library using Bowtie 2 software. For each gene, a gene effect and score (likely maximum effect size and score) and *p*-values were calculated using the Cas9 high-Throughput maximum Likelihood Estimator

(casTLE) statistical framework as previously described. Morpheus (https://software.broadinstitute.org/morpheus/) was used to perform unbiased gene clustering on metabolic state screens. Genes were ranked according to casTLE score and complete Euclidean linkages. Functional interactions and protein-protein interactions for high confidence candidate regulators were identified using the STRING database[45].

2.4.7 General animal care

All experimental procedures involving animals were approved by the UC Berkeley Institutional Animal Care and Use Committee. Mice were maintained from 6 to 12 weeks of age on a 12 hr light:12 hr dark cycle at room temperature in the UC Berkeley pathogen-free barrier facility with free access to water and standard laboratory chow diet (PicoLab Mouse Diet 20 no. 5058, LabDiet). We used CLCC1 flox/flox and Albumin-Cre in the C57BL/6J genetic background (stock no. 000632). These animals were a generous gift from Dr. G. Ku at UCSF.

Experimentation was performed between 8-12 weeks of age. In animal experiments, all measurements were included in the analysis. Mice were randomly allocated to groups; the only criteria were sex and age as explained above. The sample size and number of replicates for this study were chosen based on previous experiments performed in our laboratory and others. No specific power analysis was used to estimate sample size. Imaging studies could not be done blinded owing to the evident intrinsic features of the datasets. *In vivo* studies could not be blinded owing to the adenoviral injection protocol. Experimental and control samples were processed together using the same conditions.

2.4.8 Floxed CLCC1 mouse generation

Clcc1 flox mice (generated by the Knockout Mouse Project) were obtained from the University of California Davis Mouse Biology Program (C57BL/6N-Atm1Brd Clcc1tm1a(KOMP)Mbp/JMmucd), where exon 7 has been floxed. The neomycin selection cassette and lacZ reporter were removed by breeding to CAG-Flpo (C57BL/6N-Tg(CAG-Flpo)1Afst/Mmcd). Mice were then bred for at least 4 generations to C57BL/6J animals, removing the CAG-Flpo. Genotyping for the flox-ed allele from genomic DNA was performed with the following PCR primers: TCATGACATGAACCATATGTGAATTCC and CACCATGCCTGGCTACAAATGC.

2.4.9 Adenovirus-mediated deletion of CLCC1

To deplete CLCC1, 8-week-old homozygous CLCC1-flox mice were injected with either AAV-Cre or AAV-GFP. 1.5 x 10^{11} GC of virus was diluted in 100 uL of PBS and injected via the tail vein. Mice were euthanized by CO^2 4 weeks post-injection. Livers were photographed. >4 mice were analyzed per experiment. The liver was weighed and divided into sections which were flash frozen in liquid nitrogen, transferred on dry ice, and stored at -80 °C.

2.4.10 Mouse plasma collection and analysis

Blood was collected via submandibular vein puncture and centrifuged at 2,000 x g in Microtainer SST (BD, 365967) tubes for 15 minutes at 4 °C to isolate plasma. Plasma

was analyzed via Clinical Analyzer. Triglycerides were quantified by a luciferase-based assay (Promega, J3160).

2.4.11 Flow cytometry

Cells were washed 2x in DPBS, dissociated using TrypLE Express (Gibco, 12605010), collected by centrifugation at 500 x g for 5 min, and stained with 1 µg/µL BODIPY 493/503 or 200 µM monodansylpentane (MDH) (Abcepta, SM1000b) in DPBS on ice for 30 minutes.

For all flow cytometry assays, fluorescence was analyzed using an LSR Fortessa (BD Biosciences). The following filter sets were used: FITC (GFP, BODIPY 493/503), Pacific Blue (BFP, MDH), and Texas-Red (mCherry). FlowJo Software (BD Biosciences) was used to quantify fluorescence and generate representative histograms.

2.4.12 Immunoblotting

Cells were lysed in 1% SDS and sonicated at 15% amplitude for 15 seconds. For albumin secretion, cells were incubated for 24 h in FBS-free DMEM, and proteins were precipitated from the media with acetone. Animal tissues were homogenized in 1% SDS with an immersion homogenizer for 15 seconds. Protein concentrations were determined and normalized using a BCA protein assay (Thermo Fisher Scientific, 23225). Equal amounts of protein by weight were combined with Laemmli buffer, boiled for 10 min at 95 °C, separated on 4–20% polyacrylamide gradient gels (Bio-Rad Laboratories) and transferred onto nitrocellulose membranes (Bio-Rad Laboratories). Membranes were incubated in 5% nonfat milk in PBS with 0.1% Tween-20 (PBST) for 30 min to reduce nonspecific antibody binding. Membranes were then incubated overnight at 4 °C in PBST containing antibodies diluted in 5% BSA, followed by incubation for at least 1 hr in fluorescence-conjugated secondary antibodies diluted in PBST containing 5% nonfat milk. Immunoblots were visualized on a LI-COR imager (LI-COR Biosciences), and Fiji/ImageJ was used for quantification of protein levels.

2.4.13 Fluorescence microscopy

For widefield microscopy of live cells, Huh7, HepG2, and U-2 OS cells were grown in 4-well or 8-well Nunc™ Lab-Tek™ II Chambered Coverglass (Borosilicate Glass 1.5; Thermo Fisher Scientific, 155360) coated with poly-L-lysine. Lipid droplets were stained with 1 µM BODIPY 493/503 for 30 minutes or 500 nM LipiBlue for 30 min, nuclei were stained with 5 µg/mL Hoeschst 33342 (Thermo Fisher Scientific, 62249) for 30 min, lysosomes were stained with 75 nM Lysotracker DND-22 (Thermo Fisher Scientific, L7525) for 30 min, and mitochondria were stained with 500 nM Mitotracker Green (Thermo Fisher Scientific, M7514) for 30 min. For imaging the ER, cells were transiently transfect with BFP-KDEL (Addgene, 49150) and imaged 48 hr later. For imaging of nuclear blebs, cells were transiently transfected with MLF2-GFP (a gift from Dr. C. Schlieker) and imaged 48 hr later. Prior to imaging, cells were washed 2x with DPBS and imaged in fresh phenol red-free medium supplemented with 10% FBS. Live cells were imaged using a Zeiss Axio Observer 7 fitted with a 63X oil objective using DAPI, GFP, Cy-3, and Cy-5 filters. Cells were imaged at 37 °C with 5% CO^2. Z-stacks of 0.2-µm thickness were acquired. For widefield microscopy of fixed cells, Huh7 cells were grown

in 12-well plates on glass coverslips coated with poly-L-lysine. Cells were washed 3x with DPBS, fixed for 15 min in 4% (w/v) PFA in DPBS and washed 3x again with DPBS. Cells were permeabilized for 15 min with 1% BSA in DPBS containing 0.1% Triton X-100 when staining for ER, Golgi, or nuclear proteins or 0.01% digitonin when staining for LD proteins and then washed 3x with DPBS. Cells were incubated in antibodies to PLIN2 (Abcepta, AP5118c), GM130 (Cell Signaling, 12480), CLCC1 (Thermo, HPA009087), KDEL (Abcam, ab276333), or lamin A/C (Cell Signaling, 4777) diluted at 1:1000 in 1% BSA in DPBS for 1 hr in the dark. Lipid droplets were stained with 1 µM BODIPY 493/503 for 30 minutes or 500 nM Lipi-Blue for 30 minutes, nuclei were stained with 1 µg/mL DAPI, and primary antibodies were blotted with fluorescent secondaries (Thermo Fisher, A21202, A-21109) diluted at 1:1000 for 30 min in the dark. Cells were washed 3x with DPBS and coverslips were mounted on 1 mm glass slides using Fluoromount-G (SouthernBiotech, 0100-01). For live cell confocal microscopy, Huh7 cells were grown in 24-well glass bottom plates (170 µm coverglass bottom; Eppendorf, 0030741021; Cellvis, P24-1.5H-N). Cells were either untreated or incubated in 100 µM oleate-BSA complex for 24 hr, 1 µg/ml triacsin C for 8 hours, or 0.2% FBS-containing DMEM (serum starve) for 48 h. Lipid droplets were stained with 1 µM BODIPY 493/503 and nuclei were stained with 5 µg/mL Hoeschst 33342 for 30 minutes. Prior to imaging, cells were washed 2x with DPBS and imaged in fresh phenol red-free medium supplemented with 10% FBS. Live cells were imaged using an Opera Phenix Plus High-Content Screening System (Perkin Elmer) confocal microscope equipped with a 40X water immersion objective using DAPI and GFP filters. Cells were imaged at 37 °C with 5% CO2. Z-stacks of 0.3- µm slices were acquired.

Images were merged and brightness and contrast were adjusted using Fiji/ImageJ (https://imagej.net/software/fiji/). LDs were quantified by creating a custom analysis sequence using Harmony High Content Image Analysis Software, v4.9 (Perkin Elmer). For each field, maximum projection Z-stacks were processed with advanced flatfield correction. Nuclei and cytoplasm were defined using the DAPI and GFP channels, respectively, and border cells were automatically excluded from analyses. LDs were defined using the “Find Spots” building block (Lipi-Green stain, GFP channel), thresholding for size, intensity, and roundness. For each cell, lipid droplet number and area were quantified. LD quantification data were graphed and analyzed in Prism 9 (GraphPad).

2.4.14 Transmission electron microscopy

For cell lines, Huh7 and U-2 OS cells were grown on 3 cm gridded LabTek dishes and fixed in 2% paraformaldehyde and 2% glutaraldehyde in PBS. Samples were stained with 1% osmium tetroxide + 1.5% potassium ferrocyanide for 1 hr and 1% uranyl acetate overnight. The next day, samples were washed and subsequently dehydrated in grades of ethanol (10 min each; 30%, 50%, 70%, 95% and 2 × 10 min at 100%). Samples were embedded in increasing concentrations of eponate resin mixed with ethanol (30 min each; 1:2, 1:1, 2:1 and 100% acetone) followed by polymerization in 100% eponate overnight at 50°C.

For liver tissues, mice were anesthetized with 300 mg/kg ketamine and 30 mg/kg xylazine in PBS and perfused with 10mL of DPBS followed by 10mL of fixative buffer containing 4 parts of FP stock (2.5 % PFA, 0.06 % picric acid in 0.2M Sodium Cacodylate buffer pH 7.4) and 1 part of 25 % glutaraldehyde. After perfusion, small pieces (1–2 mm^3) of liver were sliced at 300-µm thickness with a compresstome, transferred into a fresh fixative solution containing and incubated at 4°C overnight. Samples were then washed in ice-cold 0.15 M sodium cacodylate buffer for 5 min, 3 times, and then incubated in 0.1 M sodium cacodylate solution containing 1% osmium tetroxide and 1.5% potassium ferrocyanide for 1 hr at 4°C. Samples were rinsed 3x with water and incubated for 20 min in 1% thiocarbohydrazide and rinsed again 3x for 5 min with water. Samples were incubated in 2% OsO4 for 30 min and then rinsed 3x for 5 min with water, followed by washing 3x and incubation overnight at 4 °C in 1% uranyl acetate in MB. The next day, samples were washed and subsequently dehydrated in grades of acetone (10 min each; 50%, 70%, 90% and 2 × 10 min at 100%). Samples were embedded in increasing concentrations of eponate resin mixed with acetone (30 min each; 50%, 70%, 90% and 100% acetone) followed by incubation in 100% eponate for 4 hr. The samples were moved to fresh 100% eponate and polymerized at 65°C for 24 hr.

The resin embedded sample blocks were trimmed, and 70 nm ultrathin sections were cut using a Leica UC6 ultramicrotome (Leica Microsystems, Vienna, Austria) and collected onto formvar-coated slot grids. Sections were imaged to find target regions using a Tecnai 12 120kV TEM (FEI, Hillsboro, OR, USA) and data recorded using an Gatan Rio16 CMOS camera and GMS3 software (Gatan Inc., Pleasanton, CA, USA).

2.4.15 Structure predictions

Monomeric and multimeric sequences were submitted to AlphaFold2 using MMseqs2 using either the Google Colabatory[46] or COSMIC2[47] or were submitted to DMFold, MultiFOLD, or trRosetta[48]. The pLDDT of core homology regions as monomers and ring oligomers predicted by AlphaFold2: CLCC1 residues 209-353: monomer 79.2%, 16-mer: best 80.9%, average 80.2%; Brr6 residues 44-185: monomer 80.5%, 16-mer: best 78.1%, average 77.0%[49,50].

2.4.16 Focused ion beam scanning electron microscopy (FIB-SEM)

Mouse livers were fixed and prepared described above. The trimmed sample blocks were glued with silver paint (Ted Pella Inc.) onto Al stubs, and sputter coated (Pd/Au) with a Tousimis sputter coater on top of a Bio-Rad E5400 controller. Focused Ion Beam Scanning Electron Microscopy (FIB-SEM) imaging were performed using a Zeiss Crossbeam 550 (Carl Zeiss Microsystems GmbH, Oberkochen, Germany). The sample was tilted at 54˚ in order to perpendicular to ion beam. The FIB milling and SEM imaging of the target area were set up using Atlas 5 3D tomography (Carl Zeiss Microsystems GmbH, Oberkochen, Germany). Slices with a thickness of 10 nm were milled from the target area using the 30 kV 300pA ion beam. Energy-selective Backscattered (ESB) images were collected at 1.5 kV 1nA, with a dwell time of 18 ns, image pixel size of 10 nm, and tilt correction angle of 36°. The collected images were aligned with the Slice Registration in Dragonfly 2022.2 (Comet Technologies Canada Inc., Canada).

2.4.17 FIB-SEM data segmentation, quantification, and visualization

Ground truth labels were generated by manually annotating each class (ER, mitochondria, nucleus, and lipid droplets) in five consecutive full-size images using Napari (v0.4.18). Tunable 2D-U-Net networks (DLSIA) were used to obtain rough predictions for each class[51]. These rough predictions were manually proofread and corrected in Napari. A block consisting of at least 250x250x250 voxels was used to train and fine-tune 3D-U-Net network models with Incasem[52]. Additional proofreading and manual corrections were performed in Napari. Objects, images, videos and quantifications from each class were generated using Arivis Vision 4D (v3.6.0).

2.4.18 Liver histology

Liver preparation was performed as described above with 4% PFS. Liver pieces were flash frozen, embedded in OCT, and cryosectioned into 10 µm-thick sections. Liver sections were fixed in 4% paraformaldehyde for 20 min and stained with either oil red O or hematoxylin and eosin. Images were acquired on a Zeiss LSM 880 FCS.

2.4.19 BODIPY 558/568 C12 incorporation assay

Huh7 safe-targeting control and CLCC1^{KO} cells were seeded in 60-mm plates at 350 cells per plate. To determine the rate of LD biogenesis, cells were incubated in BODIPY C12-BSA complex (complete media + 1% BSA + 1 µM BODIPY 558/568 C12) for 0, 1, 3, or 6 hr. Cells were harvested by washing them twice, collecting in cold DPBS, and transferring to Eppendorf tubes (Eppendorf, 022363352). Cells were centrifuged at 500 x g for 5 min, washed in DPBS, and centrifuged again. Cell pellets were stored at -80 °C until the lipid extraction step. For the lipolysis assay (measuring loss of esterified C12), cells were incubated in BODIPY C12-BSA complex for 16 hr. Cells were then washed 3x with media and incubated in fresh media for 1 hr. Cells were then treated with 1 µg/mL triacsin C for 0, 6, or 24 hr. Cells were harvested, and pellets stored at -80 °C as described above.

2.4.20 Triglyceride measurements by thin layer chromatography

Cell pellets were thawed at room temperature and resuspended in 50 µL DPBS. Liver tissues (approximately 30 mg, three per mouse) were homogenized in 1 ml methanol using an immersion homogenizer for 5 min at 4°C. Lipids were extracted by adding tert-butyl methyl ether (1250 µL) and methanol (375 µL). The mixture was incubated on an orbital mixer for 1 hr at room temperature. To induce phase separation, water (315 µL) was added, and the mixture was incubated on an orbital mixer for 10 min at room temperature. Samples were centrifuged at 1,000x g for 10 minutes at room temperature. The upper organic phase was collected and subsequently dried *in vacuo*.

Dried lipid extracts were reconstituted in 30 µL (cells) or 200 µL (liver) chloroform/methanol (2:1, v/v). Lipids were then separated using HPTLC Silica gel 60 F254 plates (Sigma, 1137270001). 10 µL of the cell samples and 2 µL of the liver samples were spotted onto TLC plates and developed in CHCl3/EtOH/TEA/H2O (5:5:5:1, v/v). Plates were imaged on a ChemiDoc MP Imaging System (Bio-Rad Laboratories). Band densitometry analysis was performed using Image Lab 5.0 (Bio-Rad Laboratories). The reported mean ± standard deviation was determined from three biological replicates.

2.4.21 Untargeted lipidomics of mouse liver and plasma

Before extraction, frozen mouse liver was homogenized in 1 mL methanol + 0.1% BHT in a Qiagen TissueLyser II for 3 min at 30 Hz. 20 mg liver or 100 µL of plasma were transferred to a glass tube and lipids were extracted by adding tert-butyl methyl ether (4.125 ml) and methanol (1.25 mL). The mixture was incubated on an orbital mixer for 1 hr (room temperature, 32 rpm). To induce phase separation, water (1 mL) was added, and the mixture was incubated on an orbital mixer for 10 min (room temperature, 32 rpm). Samples were centrifuged (room temperature, 10 min, 17,000 x g). Upper organic phase with collected and subsequently dried in vacuo (Eppendorf concentrator 5301, 1 ppm). Mass spectrometry and lipidomic identification and analysis were performed according to Roberts et al.

For data representation, data was $\log_{10}$ transformed and autoscaled using metaboanalyst.ca.

2.4.22 Proteomic analysis of LD proteins

Safe-targeting and CLCC1^{KO} cell lines were grown until confluent in 500 cm^2 plates of cells were scraped harvested in DPBS, centrifuged for 10 min at 500 x g, and stored at -80°C. Buoyant fractions containing 1% SDS were acidified to a final concentration of 15% TFA. Samples were then cooled on ice for 30 min and centrifuged at 20,000 x g for 30 min at 4°C. The protein pellet was washed 3 times with 500 µL of ice-cold acetone and centrifuged for 10 min between each wash. The protein pellet was then dried in a vacuum evaporator for 10 min. Dried, precipitated proteins were resuspended in 0.1% RapiGest with 6 µL of sequencing-grade trypsin (Promega, 0.5 µg/µL) added to each sample and digested overnight at 37°C. Trypsinized samples were quenched with a final concentration of 5% TFA. Samples were desalted using the Waters Sep- pak 1cc (50mg) C18 cartridge. Peptides were resuspended in 1% formic acid and 0.5 µg of peptides were separated on an Easy nLC 100 UHPLC equipped with a 15 cm nano-liquid chromatography column. Using a flow rate of 300 nL/min, the linear gradient was 5% to 35% over B for 90 min, 35% to 95% over B for 5 min and 95% hold over B for 15 min (solvent A 0.1% formic acid in water, solvent B 0.1% formic acid in ACN). Peptide identified and relative abundances were determined using Proteome Discoverer 2.4. Results are represented as average ± s.d. of duplicates.

2.4.23 ApoB ELISA assay

Safe-targeting and CLCC1$_{KO}$ cells were seeded in 6 cm plates and treated with 1 µg/mL DMSO or 50 nM MTPi for 72 hr. 24 hr before harvesting, cells were changed into FBS- and phenol red-free media. Media was collected and ApoB ELISA Assay (Sigma Aldrich, RAB069) was performed according to protocol. ApoB levels were normalized to cell protein levels and results are represented as average ± s.d. of biological duplicates.

2.4.24 ASGR luciferase assay

The ASGR reporter plasmid was a generous gift from Dr. Ana Arruda's lab at UC Berkeley. Safe-targeting and CLCC1^{KO} cells were infected with lentivirus containing the ASGR construct. For the experiment, cells were changed to a fresh medium containing phenol red-free and incubated for 24 h with or without increasing doses of thapsigargin.

10 µl of media was transferred to 96-well white plates (Corning) for luciferase assays following the manufacturer's protocol. Briefly, 50 µl of luciferase substrate (1 µM Cypridina (CLUC) or 10 mM CTZ (GLUC) in 100 mM tris buffer, pH 7.5) was added to the 10 µl medium and incubated in the dark for 5 min. The luminescence was read on Infinite 200 PRO plate reader (Tecan).

2.4.25 Statistical analysis with Prism

All statistical analyses were performed using Prism 9 (GraphPad). For each panel, the number of biological replicates (n), *p*-values, and statistical tests employed are reported in figure legends and methods.

2.5 Figures

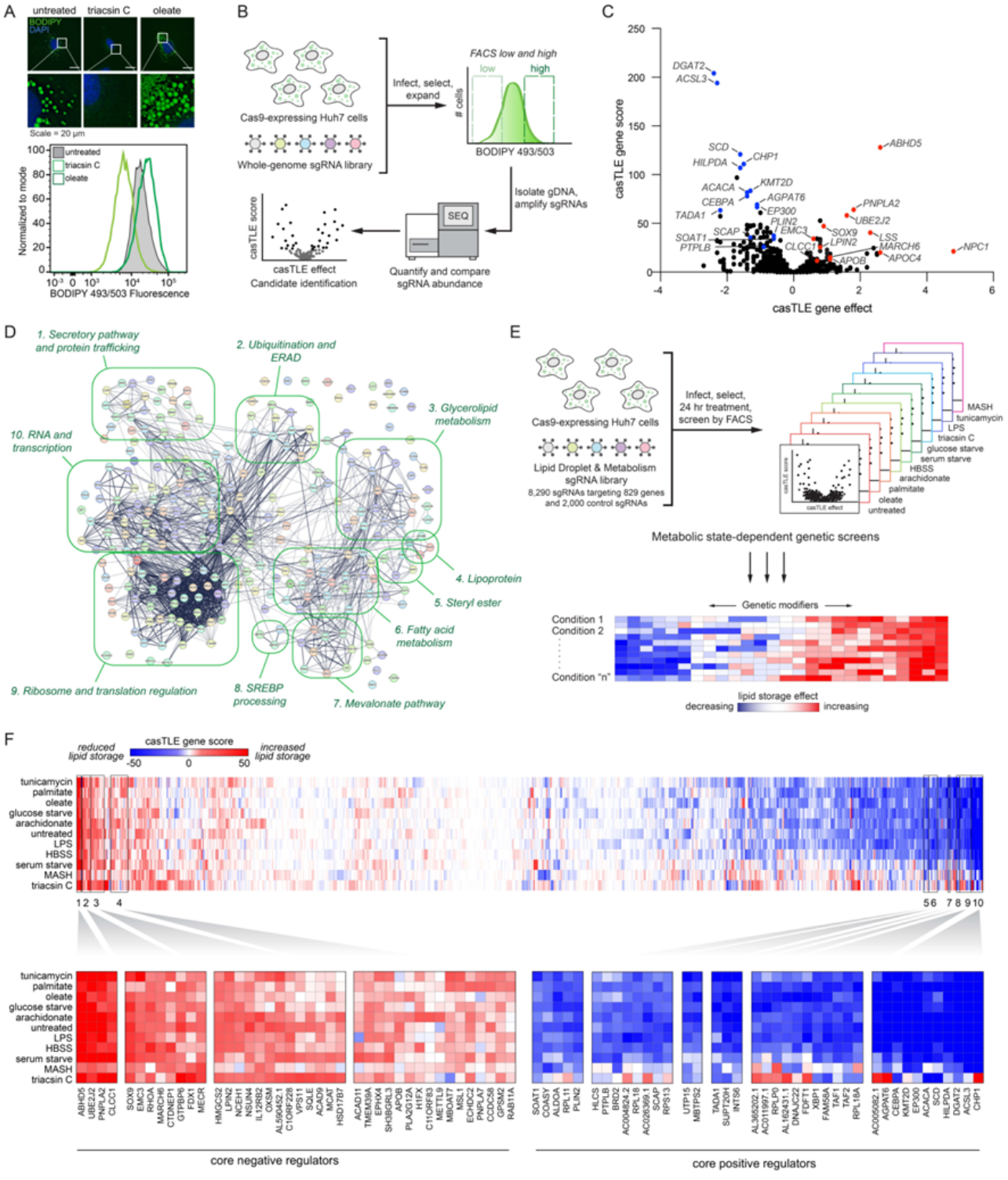
A
untreated
triacsin C
oleate
BODIPY
DAPI
Scale = 20 μm
Normalized to mode
BODIPY 493/503 Fluorescence
B
Cas9-expressing Huh7 cells
Whole-genome sgRNA library
Infect, select, expand
FACS low and high
low
high
cells
BODIPY 493/503
Isolate gDNA, amplify sgRNAs
SEQ
Quantify and compare sgRNA abundance
casTLE score
casTLE effect
Candidate identification
C
casTLE gene score
casTLE gene effect
DGAT2
ACSL3
SCD
HILPDA
CHP1
ACACA
KMT2D
CEBPA
AGPAT6
TADA1
EP300
PLIN2
SOAT1
PTPLB
SCAP
EMC3
CLCC1
SOX9
LPIN2
ABHD5
PNPLA2
UBE2J2
LSS
MARCH6
APOC4
APOB
NPC1
D
1. Secretory pathway and protein trafficking
2. Ubiquitination and ERAD
3. Glycerolipid metabolism
4. Lipoprotein
5. Steryl ester
6. Fatty acid metabolism
7. Mevalonate pathway
8. SREBP processing
9. Ribosome and translation regulation
10. RNA and transcription
E
Cas9-expressing Huh7 cells
Lipid Droplet & Metabolism sgRNA library
8,290 sgRNAs targeting 829 genes and 2,000 control sgRNAs
Infect, select, 24 hr treatment, screen by FACS
MASH
tunicamycin
LPS
triacsin C
glucose starve
serum starve
HBSS
arachidonate
palmitate
oleate
untreated
Metabolic state-dependent genetic screens
Genetic modifiers
Condition 1
Condition 2
Condition "n"
lipid storage effect
decreasing
increasing
F
reduced lipid storage
casTLE gene score
increased lipid storage
-50
0
50
tunicamycin
palmitate
oleate
glucose starve
arachidonate
untreated
LPS
HBSS
serum starve
MASH
triacsin C
1 2 3
4
5 6
7 8 9 10
ABHD5 UBE2J2 PNPLA2 CLCC1
SOX9 EMC3 RHOA MARCH6 CTDNEP1 GTPBP6 FDX1 MECR
HMGCS2 LPIN2 NCEH1 NSUN4 IL12RB2 OXSM AL590452.1 C1ORF228 VPS11 SQLE ACAD9 NSF HSD17B7
ACAD11 TMEM39A EPHX4 SH3BGRL3 APOB PLA2G12A H1FX C11ORF63 HERC3 MBOAT7 MSL1 ECHDC2 PNPLA7 CCDC58 GPSM2 RAB11A
SOAT1 COASY ALDOA RPL11 PLIN2
HLCS PTPLB BMP2K AC004854.2 RPL18 AC026369.1 SCAP RPS13
UTP15 MBTPS2
TADA1 SUPT20H INTS6
AL365202.1 AC011997.1 RPLP0 AL162431.1 DNAJC22 FDFT1 XBP1 FAM58A TAF1 TK2 RPL18A
AC005082.1 AGPAT6 CEBPA KMT2D EP300 ACACA SCD HILPDA DGAT2 ACSL3 CHP1
core negative regulators
core positive regulators

Figure 2-1. Parallel CRISPR-Cas9 screens identify metabolic state-dependent genetic modifiers of lipid storage.
A) *Top*: Screen conditions were optimized in Huh7 cells treated for 24 h with 1 μg/mL triacsin C or 100 μM oleate and analyzed by fluorescence microscopy of cells labeled with BODIPY 493/503 (LDs) and DAPI (nuclei). *Bottom*: Flow cytometry BODIPY 493/503 fluorescence histograms of untreated, 1 μg/mL triacsin C- and 100 μM oleate-treated Huh7 cells. B) Schematic of FACS-based CRISPR-Cas9 screen approach to identify genes that regulate neutral lipid abundance, using BODIPY 493/503 as a neutral lipid reporter. C) Volcano plot indicating the gene effects (i.e., phenotype) and gene scores (i.e., confidence) for individual genes from batch retest screens in Huh7 cells. Gene effects and scores are calculated from two biological replicates. Positive (red) and negative (blue) genes of interest are highlighted. D) 265 of the 285 credible hits mapped in STRING confidence (text mining, experiments, physical interactions, genetic interactions, functional pathways) grouped manually by GO functional annotations. E) Schematic of parallel CRISPR screens under eleven different metabolic stress conditions. F) Heatmap of clustered genes based on gene score across all conditions. Boxes 1-4 indicate clusters of core positive regulators and boxes 5-10 indicate clusters of core negative regulators.

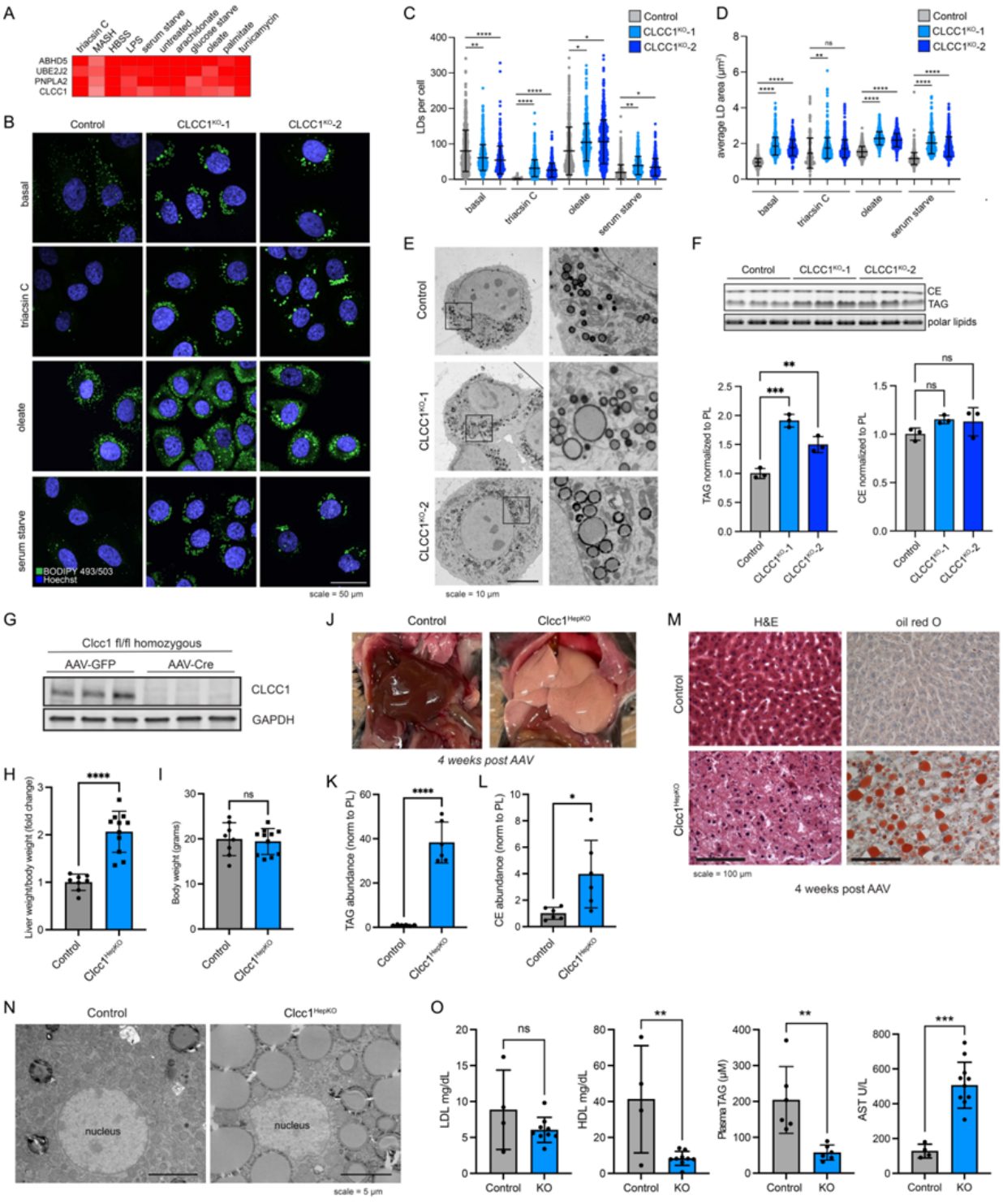

Figure 2-2. Loss of CLCC1 results in lipid droplet accumulation and hepatic steatosis.

A) Cluster of top negative regulators of lipid storage from metabolic state-dependent CRISPR- Cas9 screens. B) Representative confocal images of lipid droplets using

BODIPY 493/503 in control (expressing safe targeting sgRNA) and CLCC1^{KO} cells under basal conditions or following treatment with 1 µg/mL triacsin C for 24 h, 100 µM oleate for 24 h, or serum starve for 48 h. C) Quantification of the number of LDs from (C). Data represent mean ± SD of > 100 cells across three biological replicates. *****p<0.0001 by one-way ANOVA with Dunnett's multiple comparisons test.* D) Quantification of the area of LDs from (C). Data represent mean ± SD of > 100 cells across three biological replicates. *****p<0.0001 by one-way ANOVA with Dunnett's multiple comparisons test.* E) Representative transmission EM images of negative stained Huh7 cells expressing a safe targeting sgRNA (control) or sgRNAs against CLCC1. F) TLC resolving of TAG, CE, and polar lipids in Huh7 control and CLCC1$_{KO}$ cells. Quantification of TAG (left graph) and CE (right graph) bands normalized to phospholipids. Data represent mean ± SD of three biological replicates. *****p<0.0001 by one-way ANOVA with Dunnett's multiple comparisons test.* G) Immunoblot analysis of three Clcc1 fl/fl mice injected with either AAV-GFP (control) or AAV- Cre (Clcc1^{HepKO}). Samples were analyzed four weeks post-injection. H) Fold change in liver weight normalized to body weight for control and Clcc1^{HepKO} mice. *n > 9.* I) Body weight of the indicated control and Clcc1^{HepKO} mice. *n > 9.* J) Representative images of livers of control and CLCC1^{HepKO} m. K,L) Quantification of TAG (K) and CE (L) normalized to PL using TLC. Data represent mean ± SD of six mice. *****p<0.0001 by one-way ANOVA with Dunnett's multiple comparisons test.* M) Representative hematoxylin and eosin (H&E) stained and oil red O stained liver sections from control and Clcc1^{HepKO} mice. N) Representative transmission EM images of negative stained control and Clcc1^{HepKO} m. O) Quantification of AST, LDL and HDL from clinical analyzer. Data represent mean ± SD of > four mice. *****p<0.0001 by one-way ANOVA with Dunnett's multiple comparisons test.*

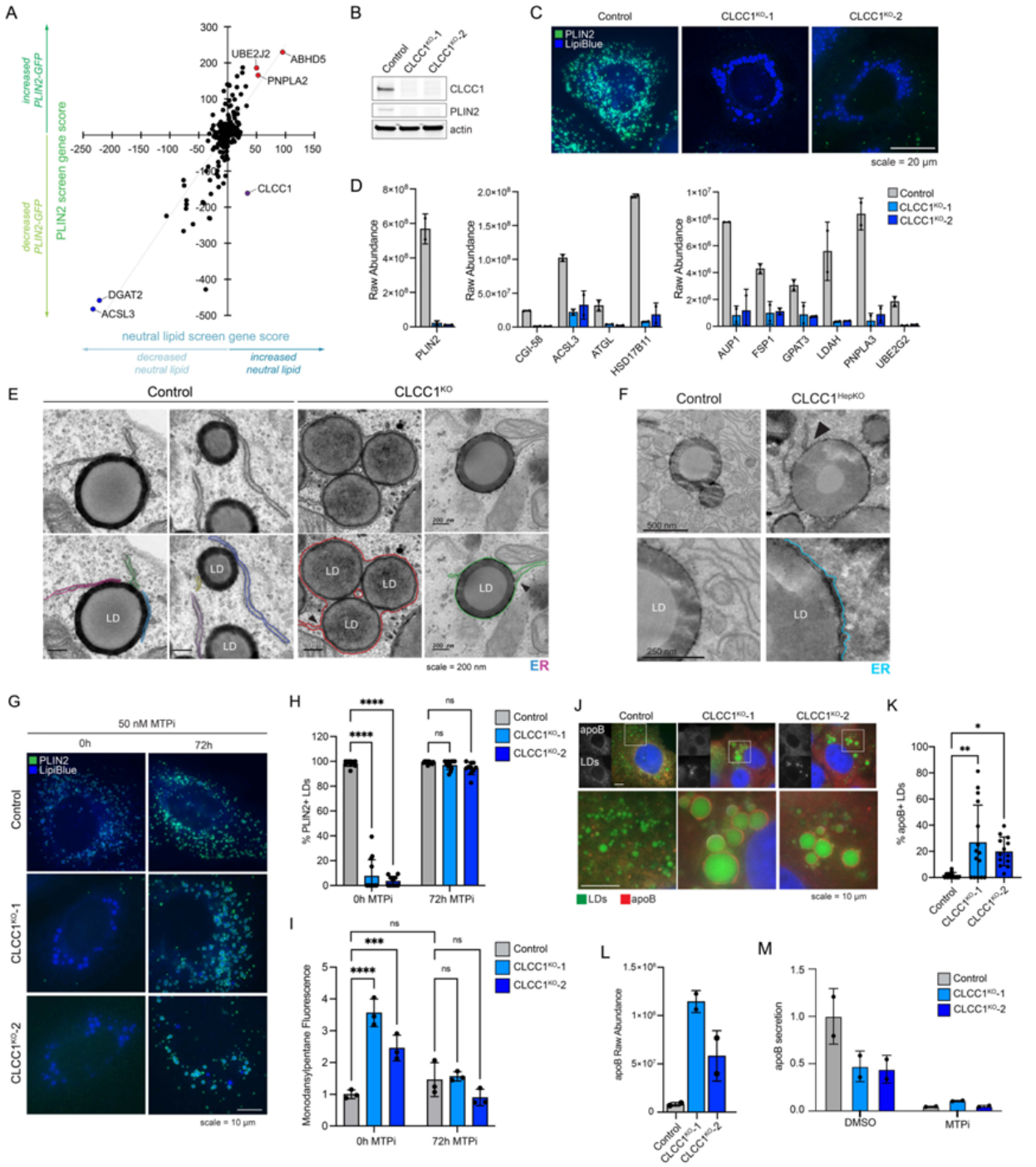

Figure 2-3. LDs in CLCC1^{KO} cells are trapped within the ER lumen.
A) Pairwise comparison of the BODIPY 493/503 neutral lipid batch retest screen (Fig 1C) and a prior PLIN2-GFP batch retest screen[9]. B) Immunoblot analysis of PLIN2 levels in control and CLCC1^{KO} cells. C) Representative fluorescence microscopy images of PLIN2 and LDs in CLCC1^{KO} cells. PLIN2 was labeled with rabbit anti-PLIN2 antibody (green) and LDs (blue) were stained with 500 nM Lipi-Blue. Scale bar represents 20 µm. D) Raw abundance values for selected known LD proteins from buoyant fraction proteomics

across two technical replicates. E) Transmission EM of negative stained control and CLCC1^{KO} cells. ER is highlighted in color and bifurcations, locations where the ER separates and a bilayer is found to encircle LDs, are denoted with black arrows. Scale bar represents 200 nm. F) Transmission EM of negative stained control and Clcc1^{HepKO} mouse liver. ER is highlighted in color and bifurcations are denoted with black arrows (as in panel E). Scale bar represents 200 nm. G) Representative fluorescence microscopy images of cells treated with the MTP inhibitor 50 nM CP-346086 for 72 h. Cells were fixed, PLIN2 was labeled with rabbit anti-PLIN2 antibody (green), and LDs were stained with 500 nM Lipi-Blue (blue). Scale bar represents 10 μm. H) Quantification of PLIN2-positive LDs in (C) where n > 10 cells. I) Quantification of flow cytometry measuring neutral lipid storage by monodansylpentane (i.e., Autodot) fluorescence. J) Representative fluorescence microscopy images of control and CLCC1^{KO} cells. ApoB was labeled with goat anti-apoB antibody (red) and LDs were stained with 500 nM Lipi-Blue (blue). Scale bar represents 10 μm. K) Quantification of the percentage of apoB-positive LDs in (H) where n > 10 cells. L) Raw abundance values for apoB from buoyant fraction proteomics across two technical replicates. M) Quantification of secreted apoB in medium using ELISA.

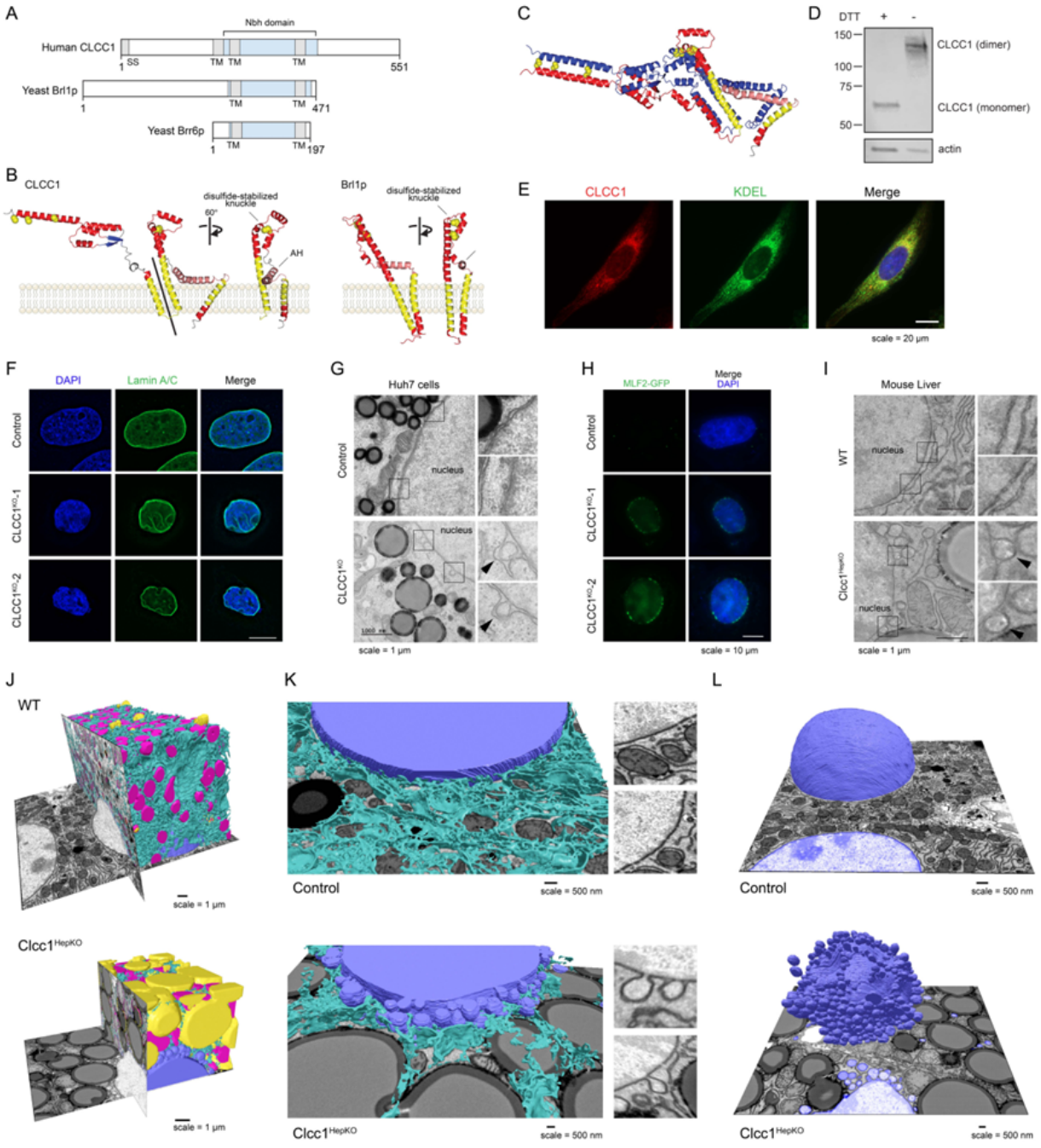

Figure 2-4. CLCC1 mediates membrane remodeling and is the human homolog of yeast Brl1p.

A) Domain structure of human CLCC1, yeast Brl1p, and yeast Brr6 indicating transmembrane domains (TM), signal sequence (SS), and the homologous 'NPC-biogenesis "h"-shaped (Nbh) domain' in blue. B) Human CLCC1 and yeast Brl1p homologous region alpha-fold structure. Ribbon colors: yellow =TMH, pink = AH, red = other helix; blue = sheet; yellow spheres = conserved cysteines. C) Predicted disulfide-stabilized CLCC1 dimer. Colors: one protomer as in B, one all blue. D) Western blot

analysis of CLCC1 in the presence and absence of the reducing agent DTT. E) Fluorescence microscopy images of CLCC1 (red), the ER marker KDEL (green) and nuclei (DAPI, blue) in control and CLCC1^{KO} cells. F) Representative fluorescence microscopy images of nuclei (DAPI, blue) and lamin A/C (green) in control and CLCC1$_{KO}$ cells. G) Transmission EM of negative stained control and CLCC1^{KO} cells. Zoomed regions are included to highlight the NE ultrastructure. H) Representative fluorescence microscopy images of the NE herniation marker MFL2-GFP (green) and DAPI-stained nuclei (blue). Scale bar represents 20 μm. I) Transmission EM of negative stained control and Clcc1^{HepKO} mouse liver. Zoomed regions are included to highlight the NE ultrastructure. J,K) Partial (J,K) reconstruction of segmented raw FIB-SEM data with ER (cyan), mitochondria (magenta), nuclei (blue) and LDs (yellow) from hepatocytes of WT (above) and Clcc1^{HepKO} (below) mice. Insets in panel K show examples of nuclear membrane in the WT and Clcc1^{HepKO} mice. L) Partial reconstruction of segmented raw FIB-SEM data with nuclei (blue), from hepatocytes of WT (above) and Clcc1^{HepKO} (below) mice.

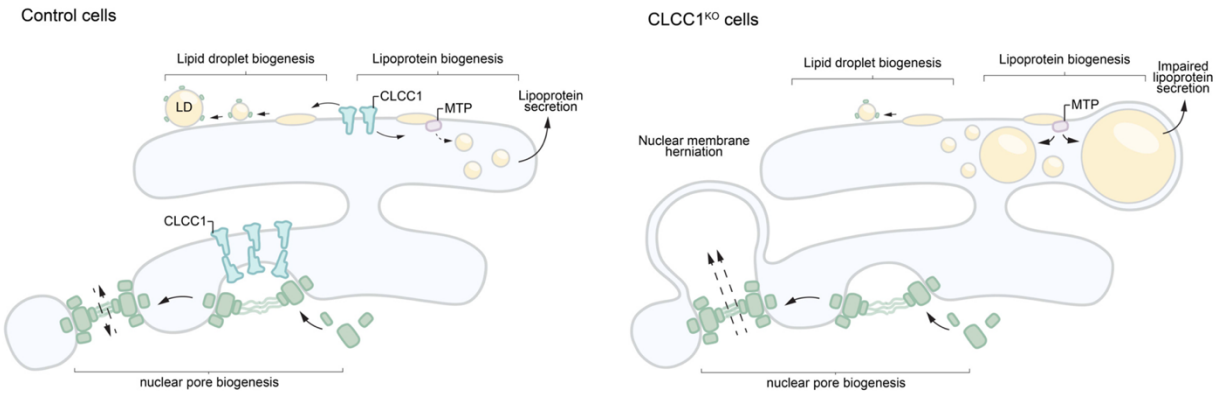

Figure 2-5. CLCC1 mediates membrane remodeling and is the human homolog of yeast Brl1p.

Model depicting the cellular functions of CLCC1 and the impact of CLCC1 depletion. CLCC1 is an ER and NE multi-pass transmembrane protein that promotes nuclear pore complex assembly and is required for the fusion of the inner and outer NE membranes. In the absence of CLCC1, nuclear pore complex assembly is impaired and large nuclear membrane herniations (i.e., blebs) accumulate. CLCC1 also regulates neutral lipid flux between cytoplasmic LDs and lumenal lipoproteins. CLCC1^{KO} cells exhibit reduced neutral lipid channeling into cytoplasmic LDs and instead neutral lipid are channeled into enlarged MTP-dependent lipoproteins that build up in the ER lumen and fail to be properly secreted. (Also see Figure 2-S17).

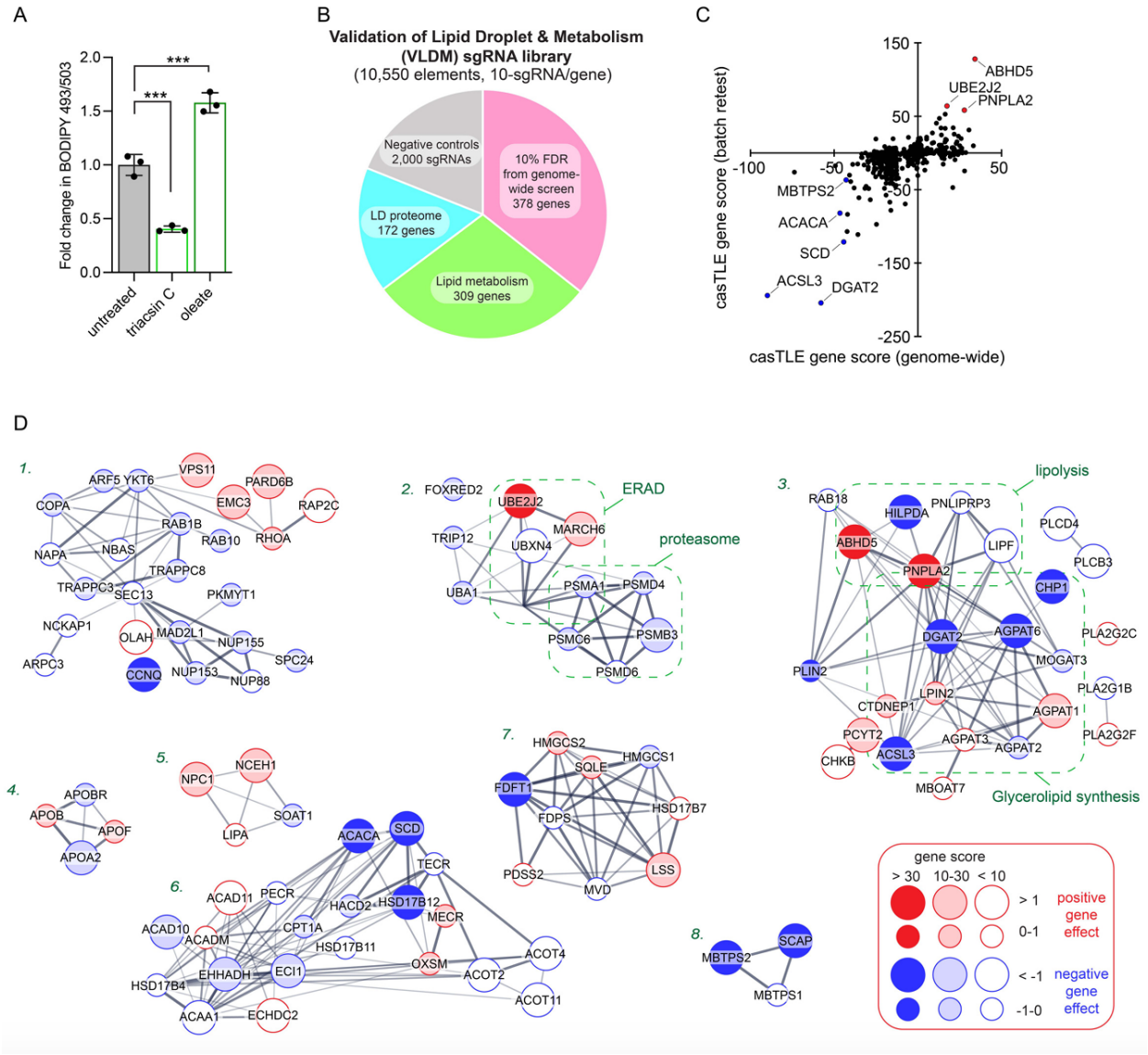

Figure 2-S1. Analysis of lipid storage CRISPR-Cas9 screens.
A) Quantification of the amount of neutral lipid from flow cytometry histograms (representative histograms shown in Fig 1A). Data represent mean ± SD across three biological replicates. *****p<0.0001 by one-way ANOVA with Dunnett's multiple comparisons test.* B) Breakdown of the custom lipid metabolism CRISPR-Cas9 library used in batch retest screens. C) Pairwise comparison of gene scores between the genome-wide and batch retest screens. Scores were adjusted as positive or negative based upon the direction of gene effect. D) Significant gene clusters from Figure 1D. Nodes are marked based on directionality of effect (red or blue), gene effect size, and confidence score.

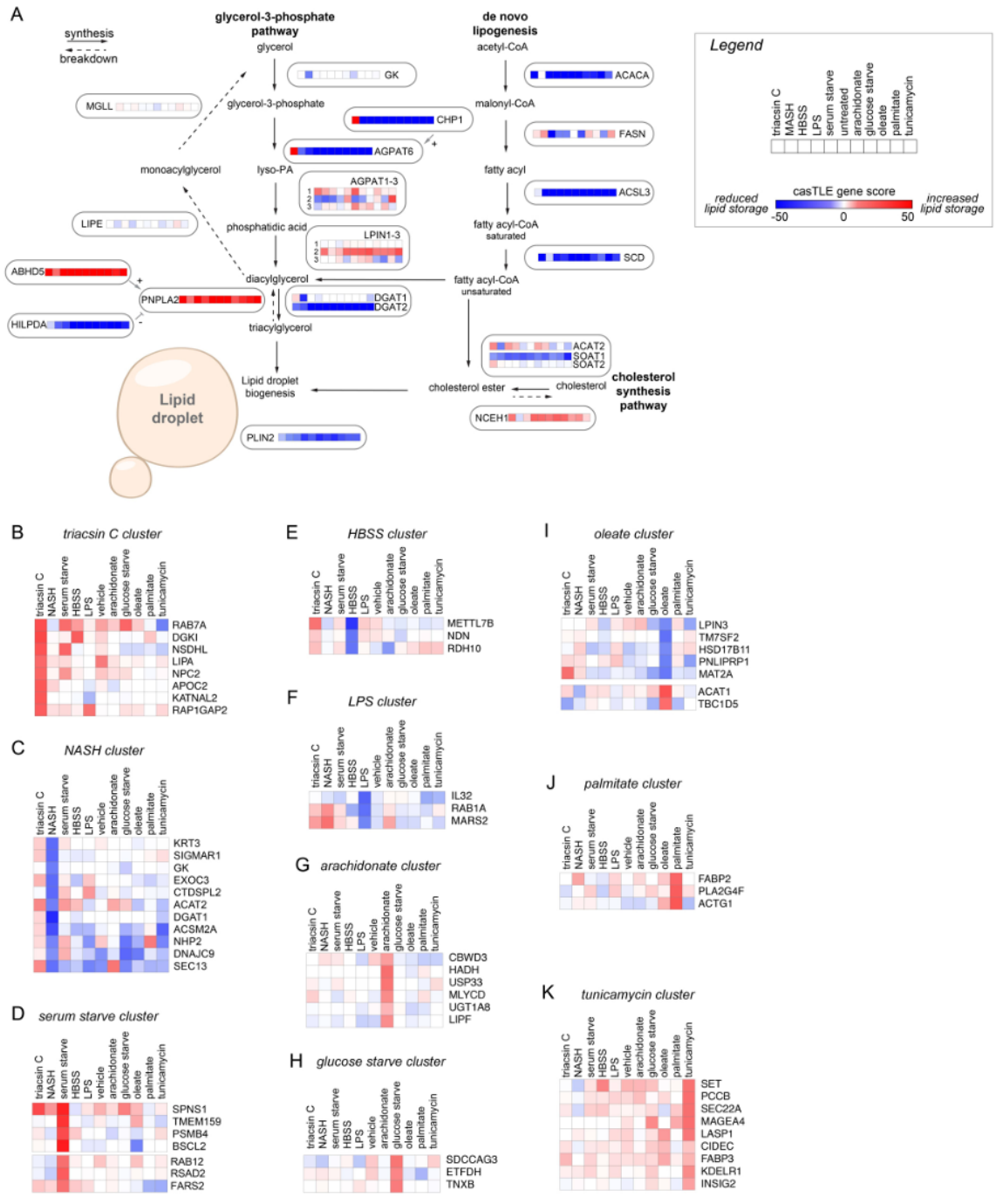

Figure 2-S2. Enriched pathways and metabolic state-specific regulators of lipid storage.

A) Schematic of LD synthesis and breakdown pathways. Genes are annotated with heatmaps corresponding to the gene score across metabolic conditions. Metabolic states follow the order indicated in the legend. B-K) Selected examples of gene clusters exhibiting metabolic state specific effects on neutral lipid storage.

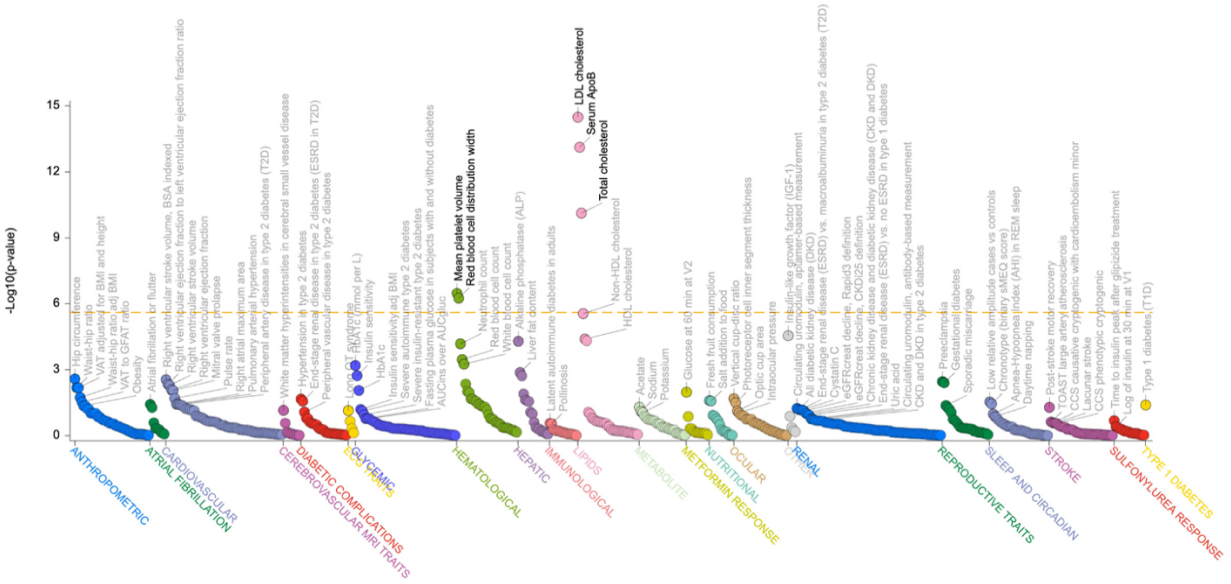

Phenotype	P-Value	Variants	Z-Stat	Sample Size
LDL cholesterol	3.27e-15	-	7.79	2,099,821
Serum ApoB	7.60e-14	34	7.39	434,341
Total cholesterol	7.39e-11	-	6.41	1,912,019
Mean platelet volume	3.39e-7	-	4.97	830,950
Red blood cell distribution width	5.64e-7	-	4.87	941,639
Non-HDL cholesterol	2.82e-6	-	4.54	994,596

Figure 2-S3. Genetic association of CLCC1 variants with altered serum lipids. Common variant gene-level associations for CLCC1 from the Common Metabolic Diseases Knowledge Portal. The plot shows phenotypic associations for CLCC1 based upon genetic associations using Multi-marker Analysis of GenoMic Annotation (MAGMA)[53].

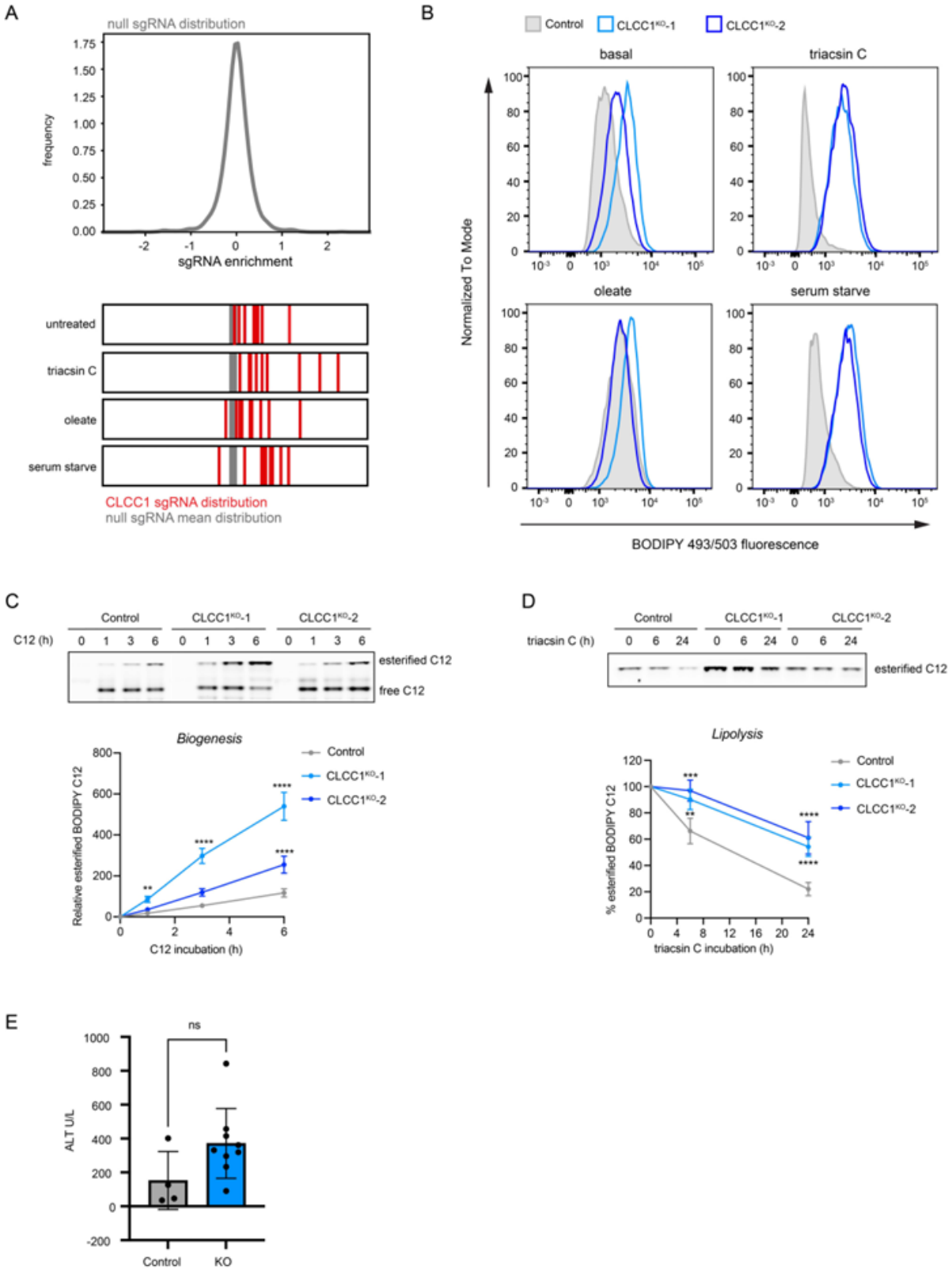
A
null sgRNA distribution
frequency
sgRNA enrichment
untreated
triacsin C
oleate
serum starve
CLCC1 sgRNA distribution
null sgRNA mean distribution
B
Control
CLCC1KO-1
CLCC1KO-2
basal
triacsin C
oleate
serum starve
Normalized To Mode
BODIPY 493/503 fluorescence
C
C12 (h)
esterified C12
free C12
Biogenesis
Relative esterified BODIPY C12
C12 incubation (h)
D
triacsin C (h)
esterified C12
Lipolysis
% esterified BODIPY C12
triacsin C incubation (h)
E
ns
ALT U/L
Control
KO

Figure 2-S4. Loss of CLCC1 results in the accumulation of neutral lipids.
A) Histogram indicating the distribution of control (null) sgRNAs. Shown below is the relative enrichment of CLCC1 targeting sgRNAs (red lines) under untreated, triacsin C, oleate, and serum starve conditions. The gray line indicates the mean of the control sgRNA distribution. B) Representative flow cytometry histograms of control and $CLCC1^{KO}$ Huh7 cells following treatment with 1 μg/mL triacsin C for 24 h, 100 μM oleate for 24 h, serum starve for 48 h, or basal levels. C) Representative TLC resolving esterified and free BODIPY C12 558/568 in Huh7 cells expressing a safe targeting sgRNA or sgRNAs against CLCC1. Cells were incubated with BODIPY C12 for the indicated times, followed by lipid extraction and TLC. A graph of the quantification of esterified BODIPY C12 levels is shown. BODIPY C12 levels at each time point were quantified relative to time 0 for each cell line. Data represent mean ± SD of three biological replicates. ****$p<0.0001$ *by two-way ANOVA with Dunnett's multiple comparisons test.* D) Representative TLC resolving esterified BODIPY C12 558/568 in Huh7 cells expressing a safe targeting sgRNA or sgRNAs against CLCC1. Cells were incubated with BODIPY C12 for 16 h followed by triacsin C treatment for the indicated times, followed by lipid extraction and TLC. A graph of the quantification of esterified BODIPY C12 levels is shown. BODIPY C12 levels at each time point were quantified relative to time 0 for each cell line. Data represent mean ± SD of three biological replicates. ****$p<0.0001$ *by two-way ANOVA with Dunnett's multiple comparisons test.* E) Quantification of ALT from clinical analyzer. Data represent mean ± SD of > four mice. ****$p<0.0001$ *by one-way ANOVA with Dunnett's multiple comparisons test.*

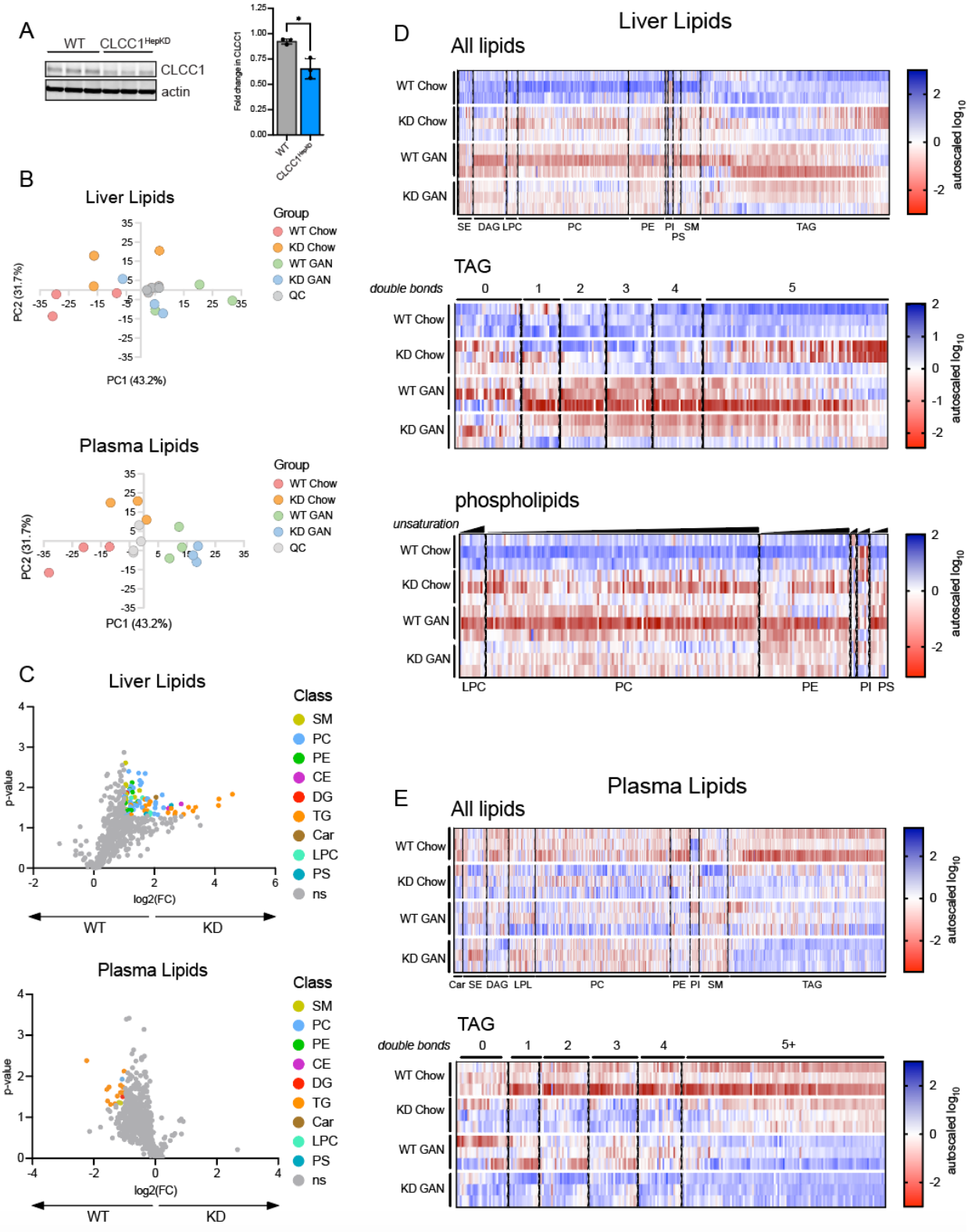
A
WT
CLCC1HepKD
CLCC1
actin
Fold change in CLCC1
B
Liver Lipids
Group
WT Chow
KD Chow
WT GAN
KD GAN
QC
PC2 (31.7%)
PC1 (43.2%)
Plasma Lipids
C
Liver Lipids
Class
SM
PC
PE
CE
DG
TG
Car
LPC
PS
ns
p-value
log2(FC)
WT
KD
Plasma Lipids
D
Liver Lipids
All lipids
WT Chow
KD Chow
WT GAN
KD GAN
SE DAG LPC PC PE PI SM PS TAG
autoscaled log10
TAG
double bonds
phospholipids
unsaturation
LPC PC PE PI PS
E
Plasma Lipids
All lipids
Car SE DAG LPL PC PE PI SM TAG
5+

Figure 2-S5. Clcc1 depletion alters lipid abundance in mouse liver and plasma.
A) Immunoblot and quantification of CLCC1 levels in control and CLCC1^{HepKD} mouse livers. B) PCA plots showing correlation between WT and CLCC1^{HepKD} mouse liver lipids on chow and GAN diets. C) Volcano plot indicating liver and plasma lipids in WT and CLCC1^{HepKD} mice on chow diet. Log2(FC) and p-values are calculated from three biological replicates. Significant lipids are highlighted by color according to lipid species. D) Heatmap of all liver lipid species identified through untargeted proteomics. Middle and bottom boxes highlight TAG and phospholipid species by degree of saturation, respectively. Values were calculated using MetaboAnalyst. E) Heatmap of all plasma lipid species identified through untargeted proteomics. Bottom box highlights TAG species by degree of saturation. Values were calculated using MetaboAnalyst.

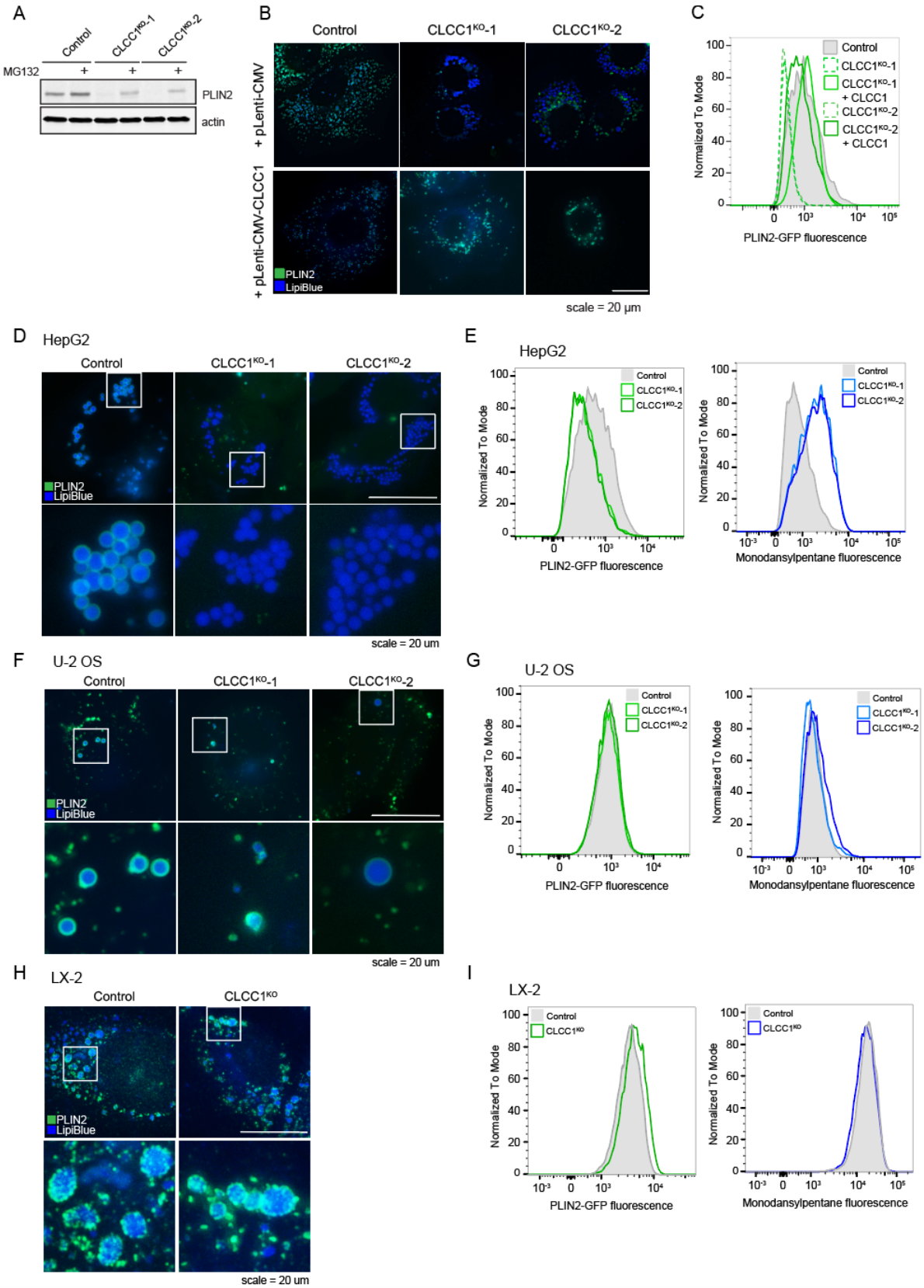
A
Control
CLCC1KO-1
CLCC1KO-2
MG132
+
+
+
PLIN2
actin
B
Control
CLCC1KO-1
CLCC1KO-2
+ pLenti-CMV
+ pLenti-CMV-CLCC1
PLIN2
LipiBlue
scale = 20 µm
C
Control
CLCC1KO-1
CLCC1KO-1 + CLCC1
CLCC1KO-2
CLCC1KO-2 + CLCC1
Normalized To Mode
PLIN2-GFP fluorescence
D
HepG2
Control
CLCC1KO-1
CLCC1KO-2
PLIN2
LipiBlue
scale = 20 um
E
HepG2
Control
CLCC1KO-1
CLCC1KO-2
Normalized To Mode
PLIN2-GFP fluorescence
Monodansylpentane fluorescence
F
U-2 OS
Control
CLCC1KO-1
CLCC1KO-2
PLIN2
LipiBlue
scale = 20 um
G
U-2 OS
Control
CLCC1KO-1
CLCC1KO-2
Normalized To Mode
PLIN2-GFP fluorescence
Monodansylpentane fluorescence
H
LX-2
Control
CLCC1KO
PLIN2
LipiBlue
scale = 20 um
I
LX-2
Control
CLCC1KO
Normalized To Mode
PLIN2-GFP fluorescence
Monodansylpentane fluorescence

Figure 2-S6. Loss of CLCC1 results in the accumulation of PLIN2-negative lipid droplets.

A) Immunoblot of PLIN2-GFP levels in control and CLCC1^{KO} cells treated with 1 μM MG132 for 12 h. B) Representative fluorescence microscopy images of PLIN2-GFP Huh7 cells, control and CLCC1KO cells, expressing a control plasmid or an untagged CLCC1 expression plasmid. LDs are stained with LipiBlue (blue). Scale bar represents 10 μm. C) Flow cytometry histograms of PLIN2-GFP fluorescence in control and CLCC1^{KO} PLIN2-GFP Huh7 cells expressing a control plasmid (dashed) or an untagged CLCC1 expression plasmid (solid). D) Representative fluorescence microscopy images of PLIN2-GFP HepG2 cells expressing a safe targeting sgRNA (control) or sgRNAs against CLCC1. LDs were stained with 500 nM Lipi-Blue. Scale bar represents 20 μm. E) Representative fluorescence microscopy images of PLIN2-GFP U2-OS cells expressing a safe targeting sgRNA (control) or sgRNAs against CLCC1. LDs were stained with 500 nM Lipi-Blue. Scale bar represents 20 μm. F) Flow cytometry histograms of PLIN2 and neutral lipid levels (monodansylpentane fluorescence) in control and CLCC1^{KO} HepG2 cells. G) Flow cytometry histograms of PLIN2 and neutral lipid levels (monodansylpentane fluorescence) in control and CLCC1^{KO} HepG2 cells.

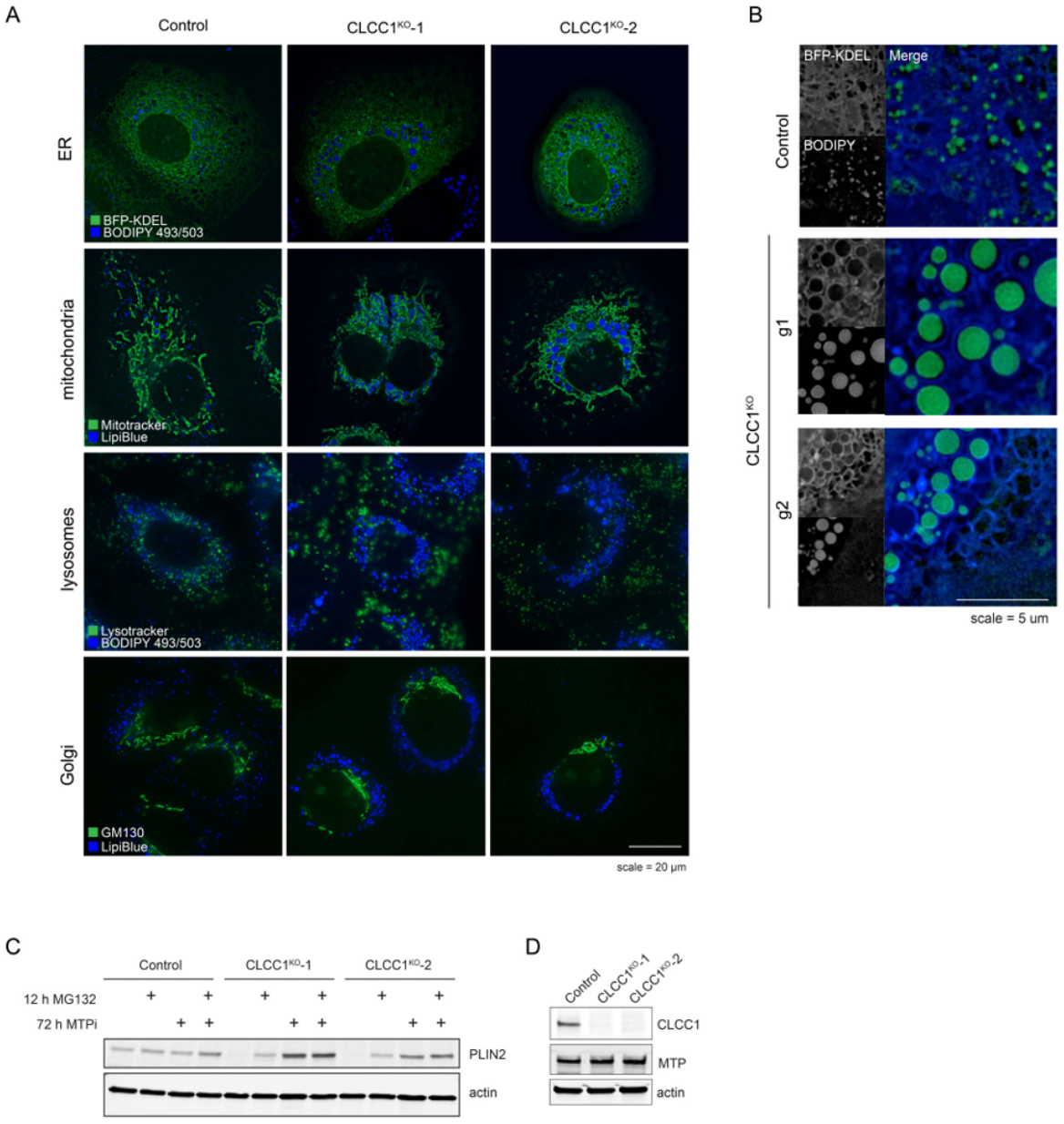

Figure 2-S7. Analysis of organelle morphology in CLCC1 knockout cell lines.
A) Representative fluorescence microscopy images of mitochondria, lysosomes, Golgi, and LDs in CLCC1^{KO} cells. Mitochondria was labeled with 500 nM mitotracker green, lysosomes were labeled with 75 nM lysotracker dnd-22, the Golgi apparatus was labeled with rabbit anti-GM130 antibody, and LDs were stained with either 500 nM Lipi-Blue or 1 µg/mL BODIPY 493/503. Scale bar represents 20 µm. B) Fluorescence imaging of ER and LDs in CLCC1^{KO} cells. ER is labeled with a transiently transfected BFP-KDEL construct and LDs were stained with 1 µg/mL BODIPY 493/503. Scale bar represents 5 µm. C) Immunoblot of PLIN2-GFP levels in control and CLCC1^{KO} cells treated with 1 µM MG132 for 12 h and/or 50 nM MTPi for 72 h. D) Immunoblot of MTP levels in control and CLCC1^{KO} cells.

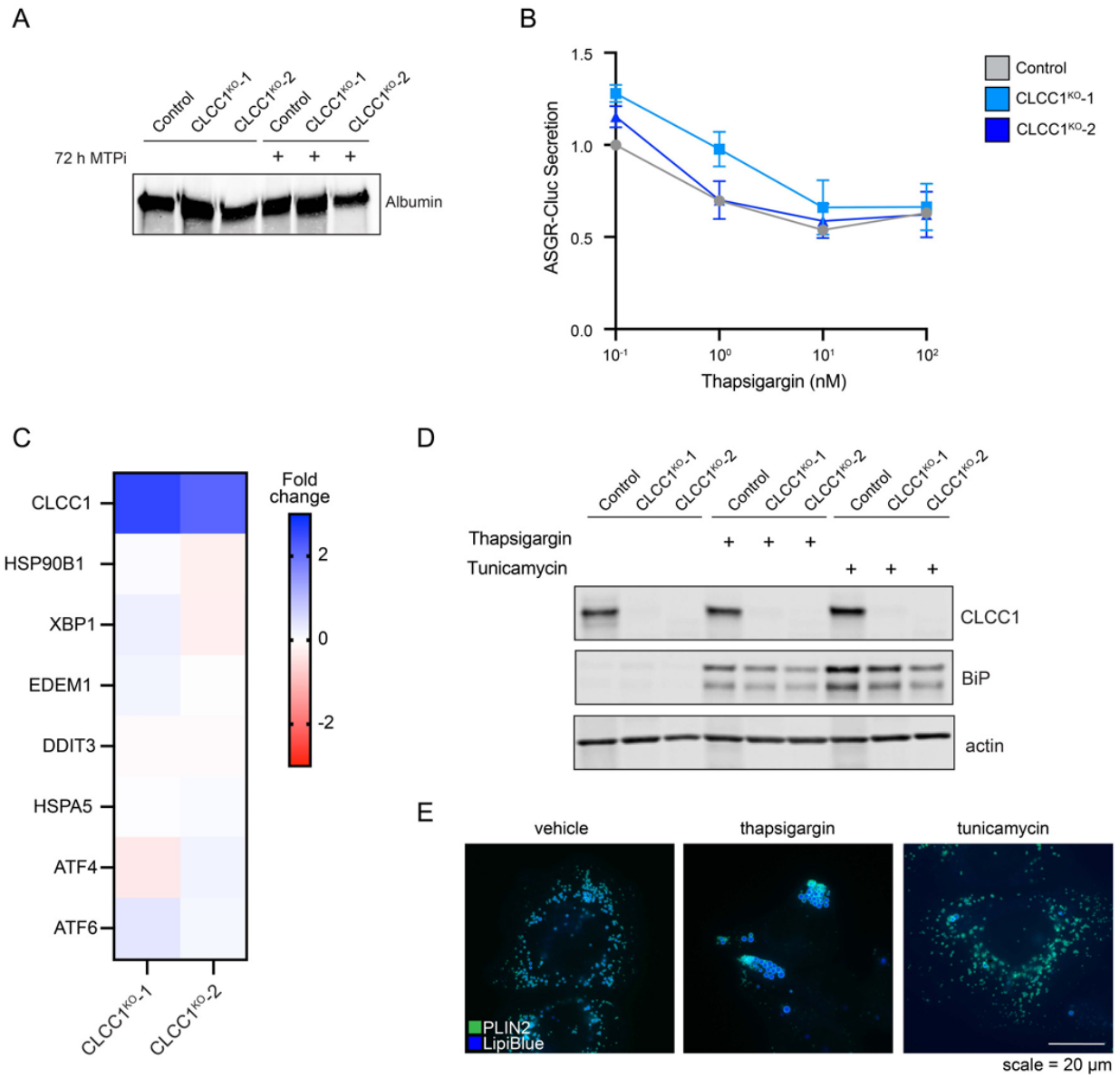

Figure 2-S8. ER stress and general secretion are unchanged in CLCC1 knockout cell lines.

A) Immunoblot of albumin secretion from control and CLCC1^{KO} cells. Conditioned serum-free media was collected and precipitated before immunoblotting. B) Quantification of ASGR-Cluc secretion in CLCC1^{KO} cells across three biological replicates. C) Fold change of selected mRNA transcripts in CLCC1^{KO} cells relative to control cells, measured using RNA sequencing. D) Immunoblot of BiP levels in control and CLCC1^{KO} cells treated with 5 μg/mL tunicamycin or 1 μM thapsigargin for 24 h. E) Representative fluorescence microscopy images of PLIN2 (green) and LDs (blue) in Huh7 cells treated with ER stress inducers thapsigargin and tunicamycin. Scale bar represents 20 μm.

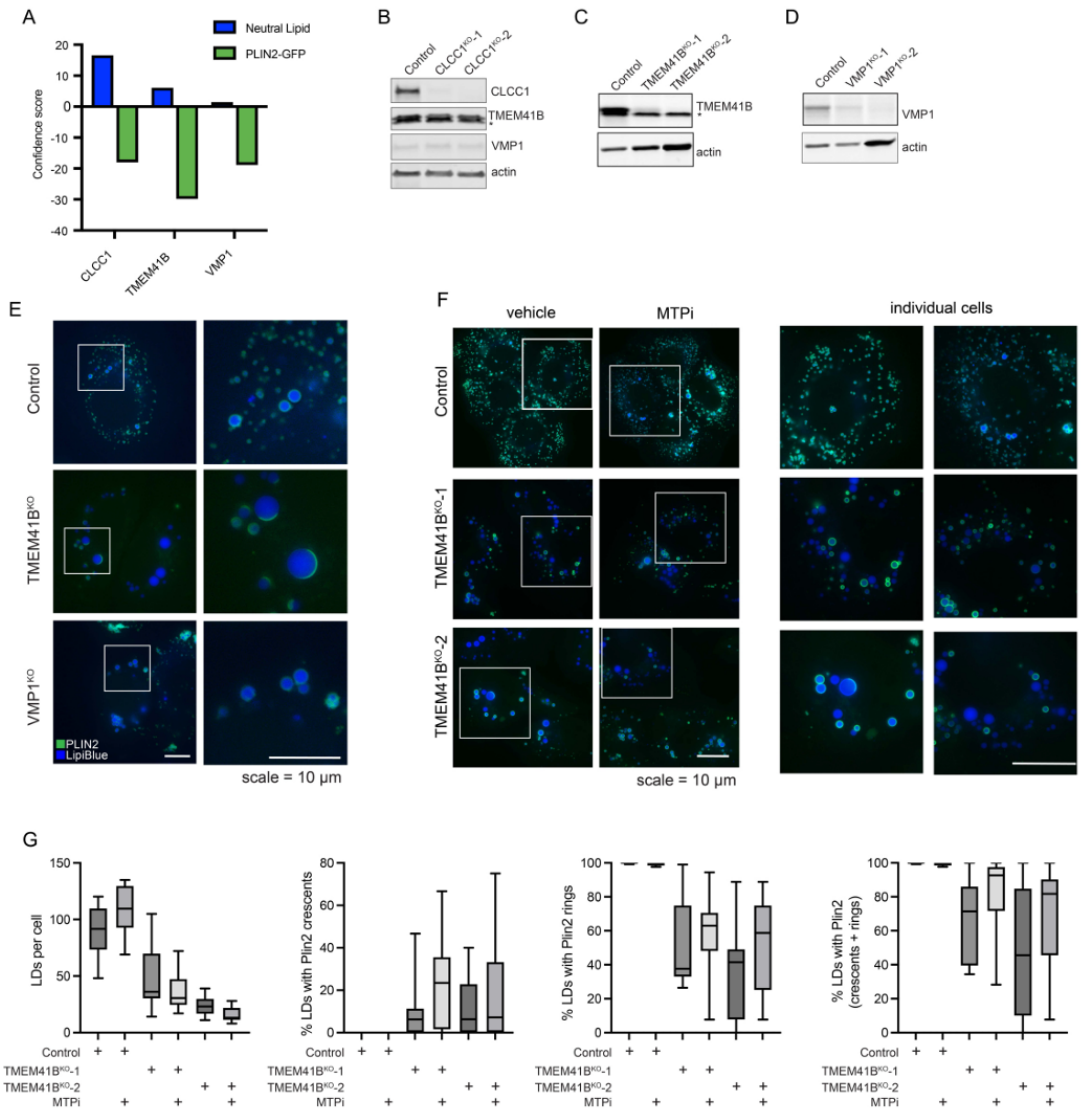

Figure 2-S9. Analysis of ER scramblases and lumenal lipid droplets.
A) Confidence score for CLCC1, TMEM41B, and VMP1 from two genome wide CRISPR screens, the neutral lipid (i.e., BODIPY 493/503) screen in the current manuscript and a previous PLIN2-GFP screen[9]. The sign, positive or negative, indicates the effect of gene depletion on neutral lipids or PLIN2-GFP levels. B) Immunoblot of the indicated proteins in control and CLCC1^{KO} Huh7 cells. C) Immunoblot of TMEM41B in control and TMEM41B^{KO} Huh7 cells. D) Immunoblot of VMP1 in control and VMP1^{KO} Huh7 cells. E) Representative fluorescence microscopy images of PLIN2 (green) and LDs (blue) in control and TMEM41B^{KO} and VMP1^{KO} cells. Scale bar represents 10 µm. F) Representative fluorescence microscopy images of PLIN2 (green) and LDs (blue) in control and TMEM41B^{KO} cells treated with MTP inhibitor (MTPi) for 72 h. Zoom images of the boxed regions are shown on the right. Scale bar represents 10 µm. G) Quantification of LDs and LD PLIN2 staining of control and TMEM41B^{KO} cells incubated in the presence and absence of MTP inhibitor (MTPi) as in panel F.

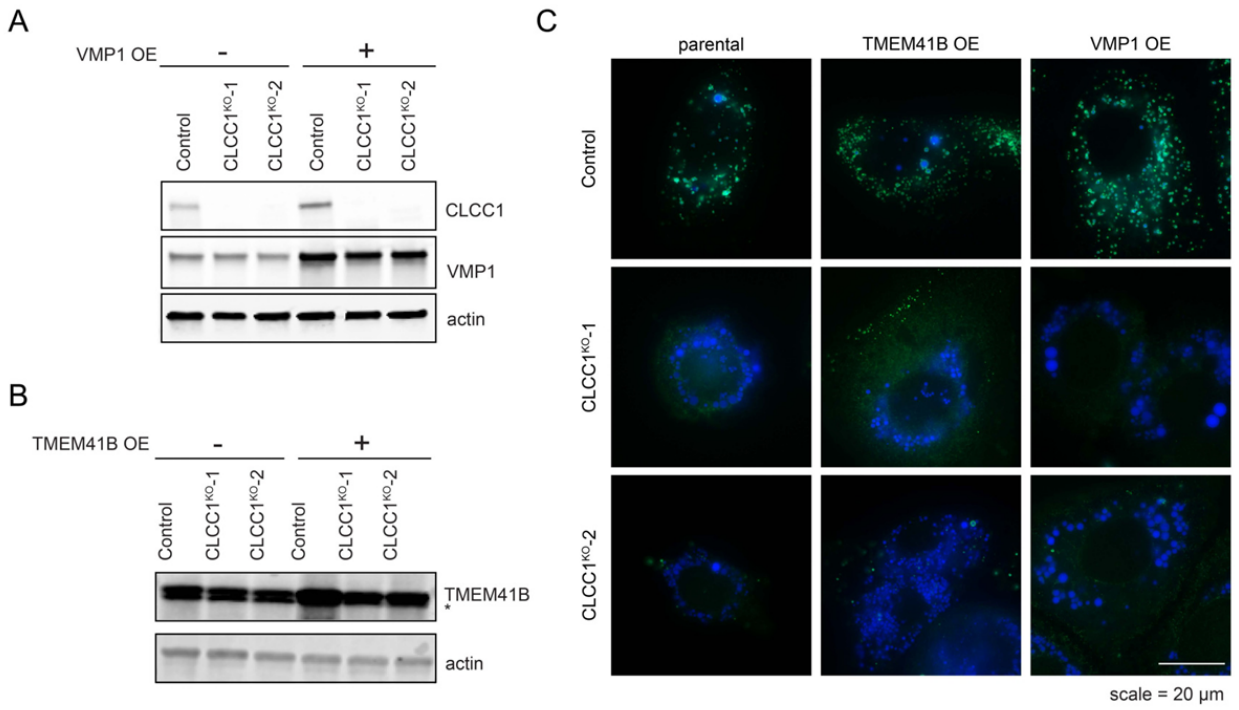

Figure 2-S10. Analysis of ER scramblases in CLCC1^{KO} cells.
A) Immunoblot of VMP1 overexpression in control and CLCC1^{KO} cells. B) Immunoblot of TMEM41B overexpression in control and CLCC1^{KO} cells. C) Representative fluorescence microscopy images of PLIN2 (green) and LDs (blue) in control and CLCC1^{KO} cells overexpression TMEM41B and VMP1, as indicated. Scale bar represents 20 µm.

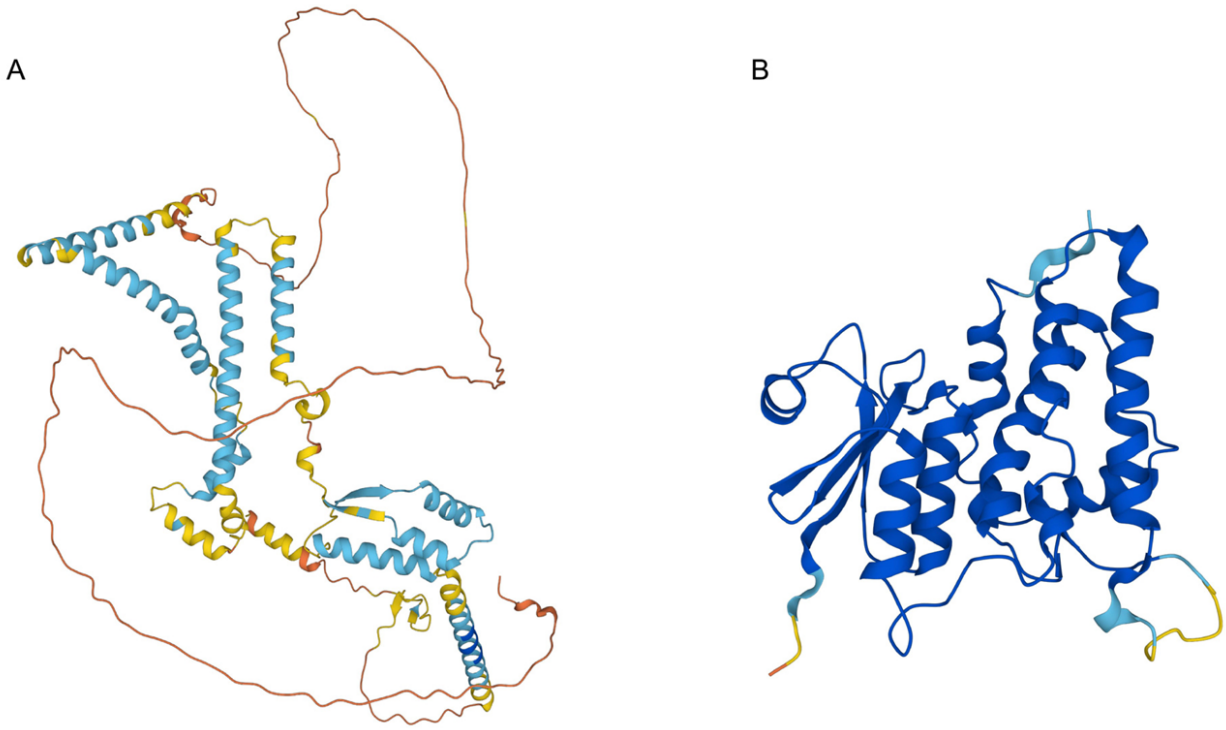

Figure 2-S11. Alphafold and multimer structural predictions.
A, B) Alphafold structural predictions of CLCC1 and CLIC1. Images colored by pLDDT (predicted local distance difference test), where blue indicates a confident prediction (light – high, dark – very high), while yellow/orange/red represent predictions of progressively low confidence.

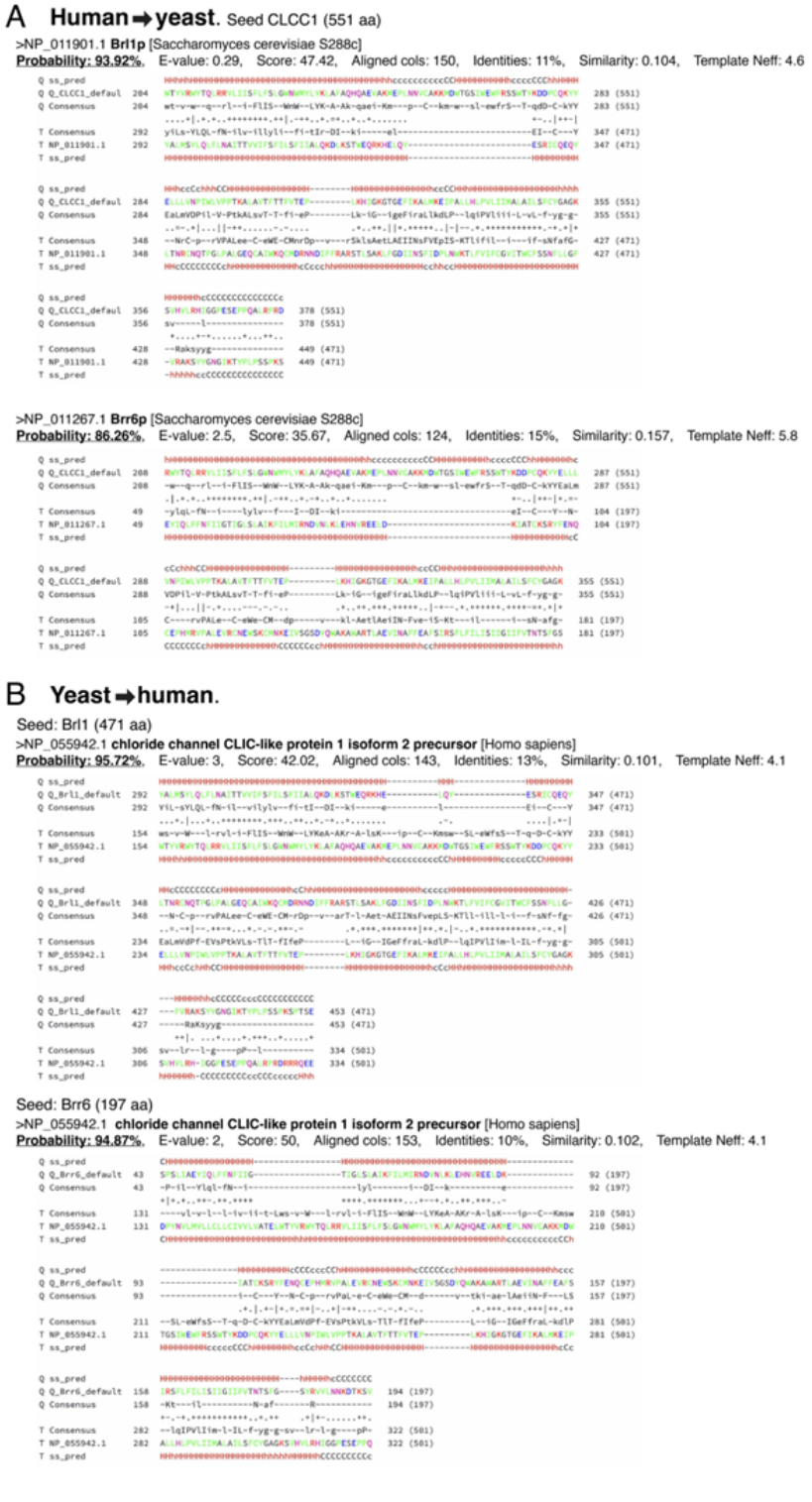

Figure 2-S12. Remote homology analysis linking CLCC1 with Brl1p and Brr6p. HHpred remote homology searches using default settings: (A) in S. cerevisiae using human CLCC1 as the query protein; (B) in human using S. cerevisiae Brl1p or Brr6p as query proteins.

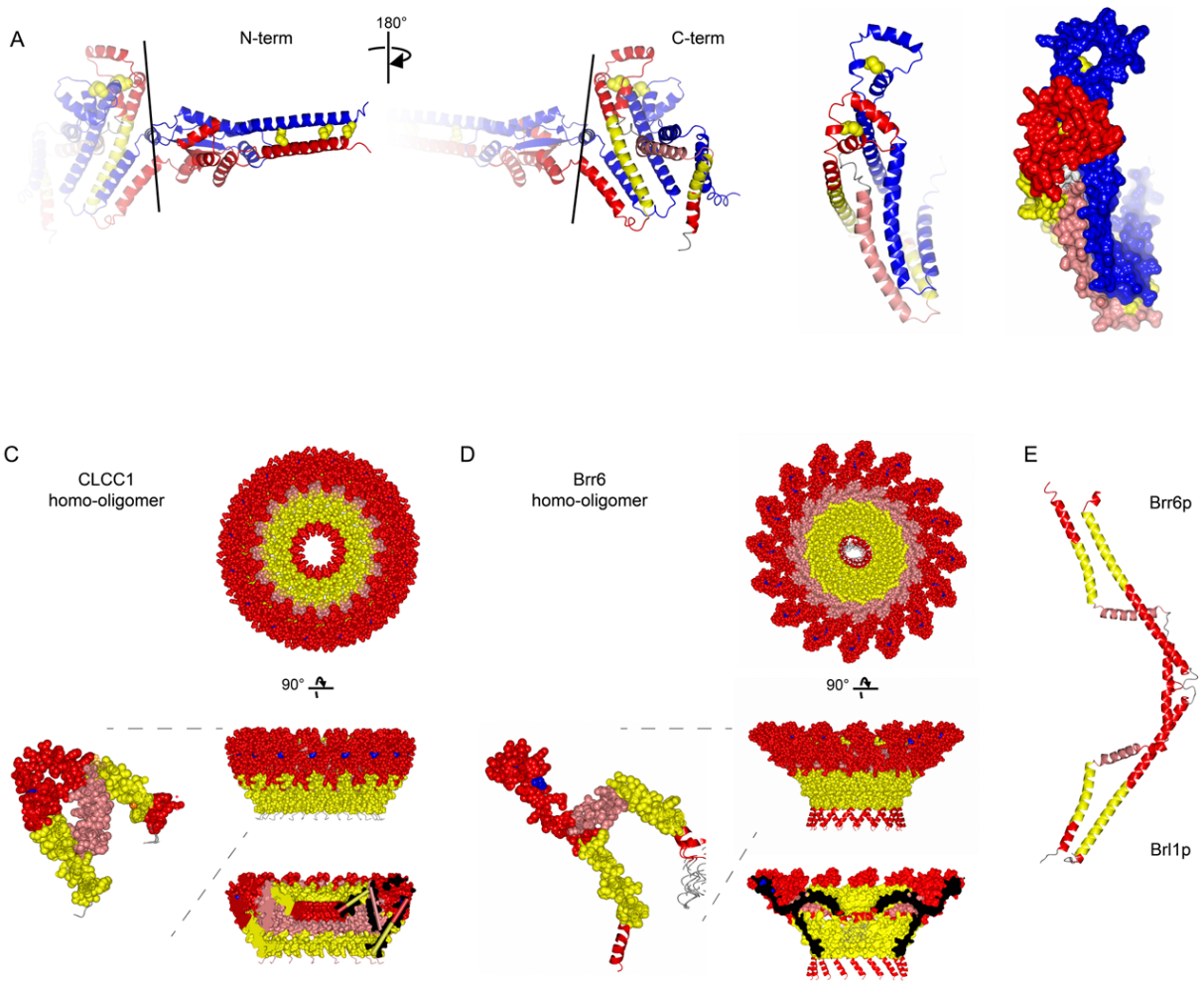

Figure 2-S13. Structure homology analysis of CLCC1 with Brr6p and Brl1p.
A) Additional visualizations highlighting the N- and C-termini of the predicted disulfide-stabilized CLCC1 dimer structure Q96S66_V1_5 created by the Levy lab[36] (downloaded from 3D-Beacons database). The two protomers are colored as in Fig 4C. B) Colabfold structural prediction of CLCC1 (205-360aa) homo-oligomer (16-subunits). Colors: yellow =TMH, pink = AH, red = other helix, blue spheres = conserved cysteines. C) Colabfold structural prediction of Brr6p (28-197aa) homo-oligomer (16-subunits). Colors as B. D) RoseTTAFold structural prediction of Brr6p/Brl1p heterodimer (38-197aa & 281-438)[45].Colors as B.

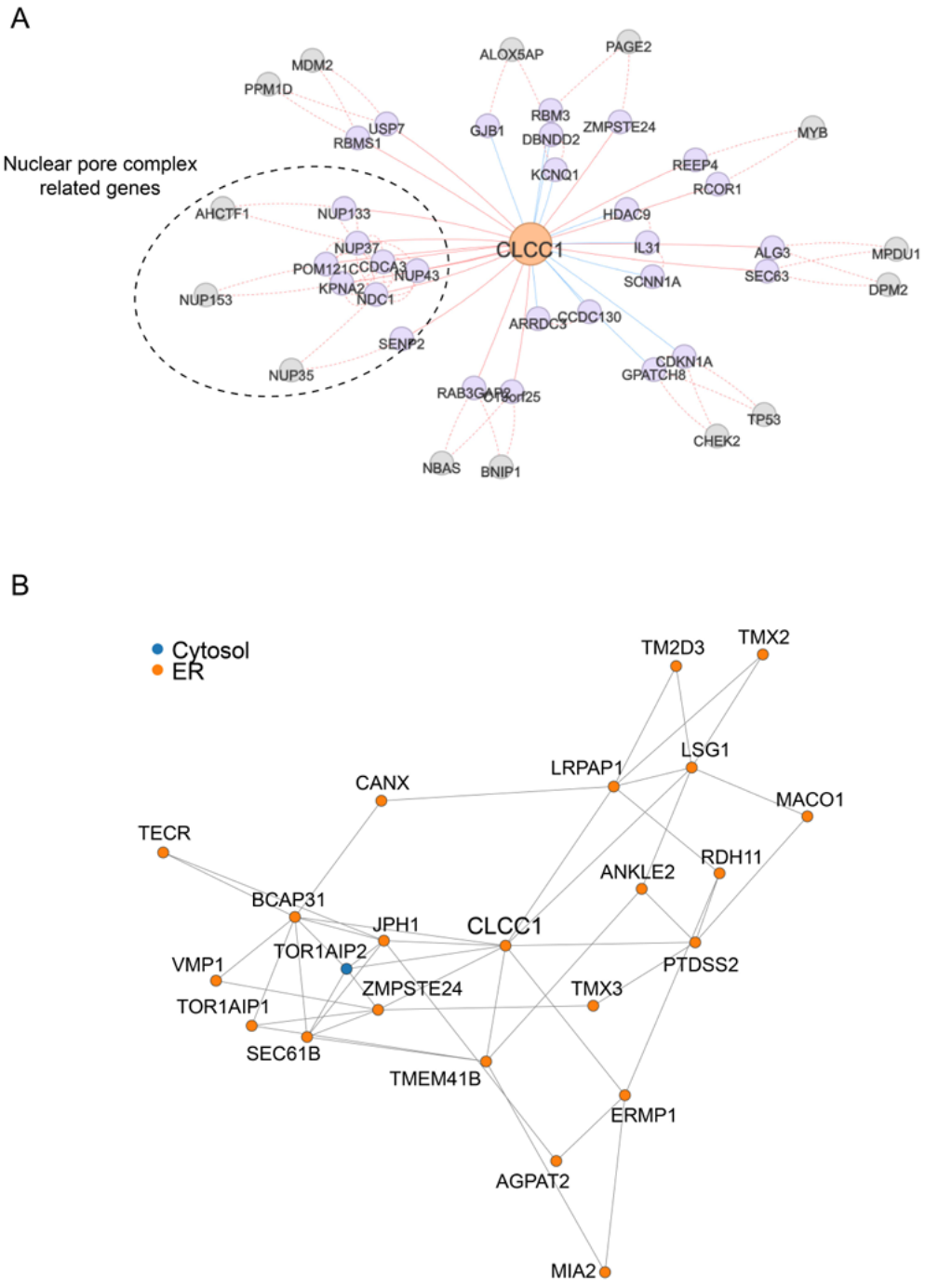

Figure 2-S14. Analyses of CLCC1 co-essentiality and localization neighborhood. A) CLCC1 co-essentiality network using FIREWORKS interactive web tool to reveal gene-gene relationships[41]. B) CLCC1 localization neighborhood using proteomic profiling data of affinity purified organelles[42].

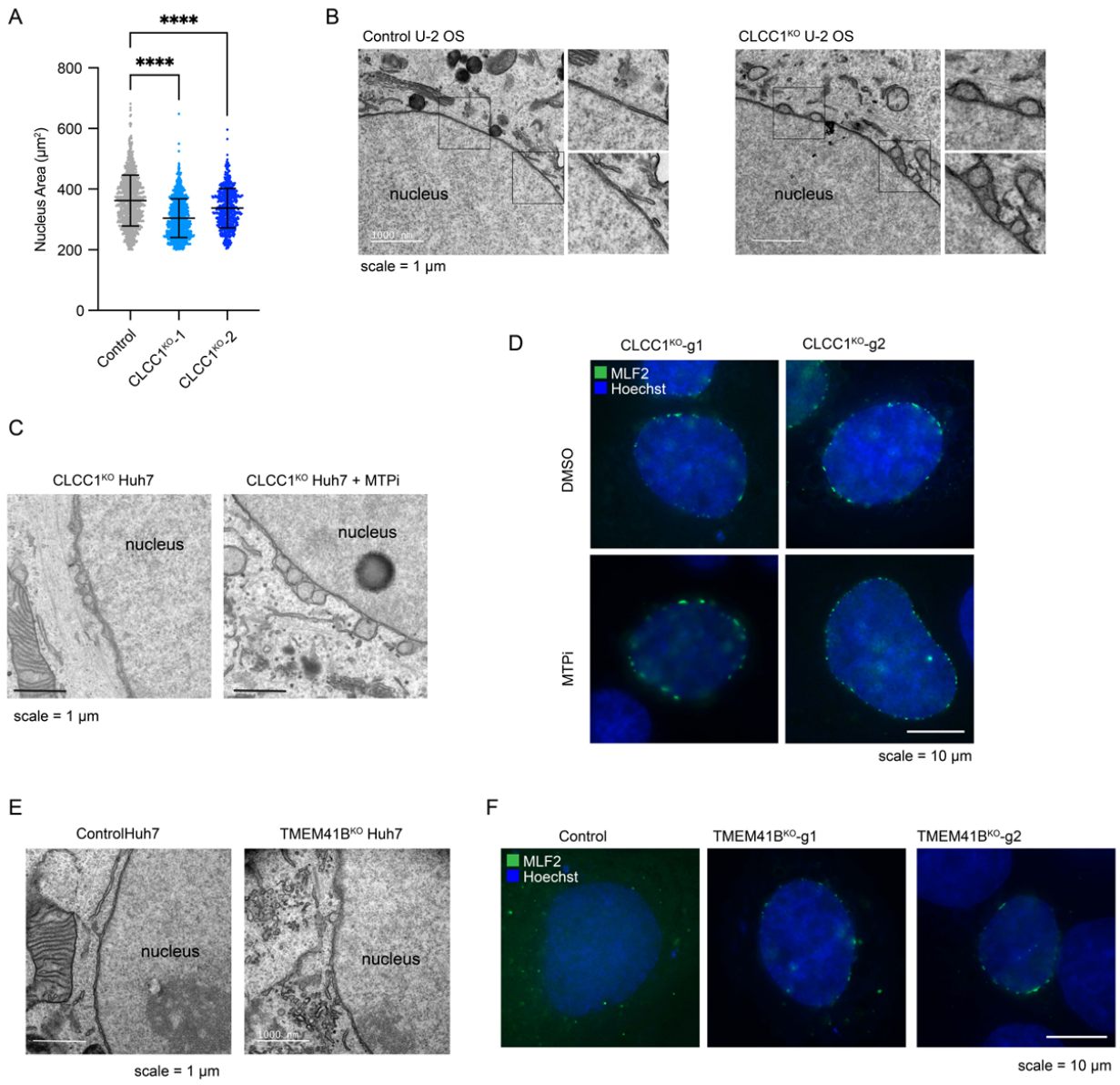

Figure 2-S15. Analysis of nuclear morphology and NE herniations.
A) Nuclei were visualized using DAPI fluorescence imaging and the area of the nucleus in control and CLCC1^{KO} cells was quantified. B) Transmission EM of negative stained control and CLCC1^{KO} U-2 OS cells. C) Transmission EM of negative stained CLCC1^{KO} Huh7 cells treated in the presence and absence of MTP inhibitor (MTPi) for 72 h. D) Fluorescence imaging of MLF2-GFP (nuclear bleb marker) in CLCC1^{KO} Huh7 cells treated in the presence and absence of MTP inhibitor (MTPi) for 72 h. E) Transmission EM of negative stained control and TMEM41B^{KO} Huh7 cells. F) Fluorescence imaging of MLF2-GFP (nuclear bleb marker) in control and TMEM41B^{KO} Huh7 cells.

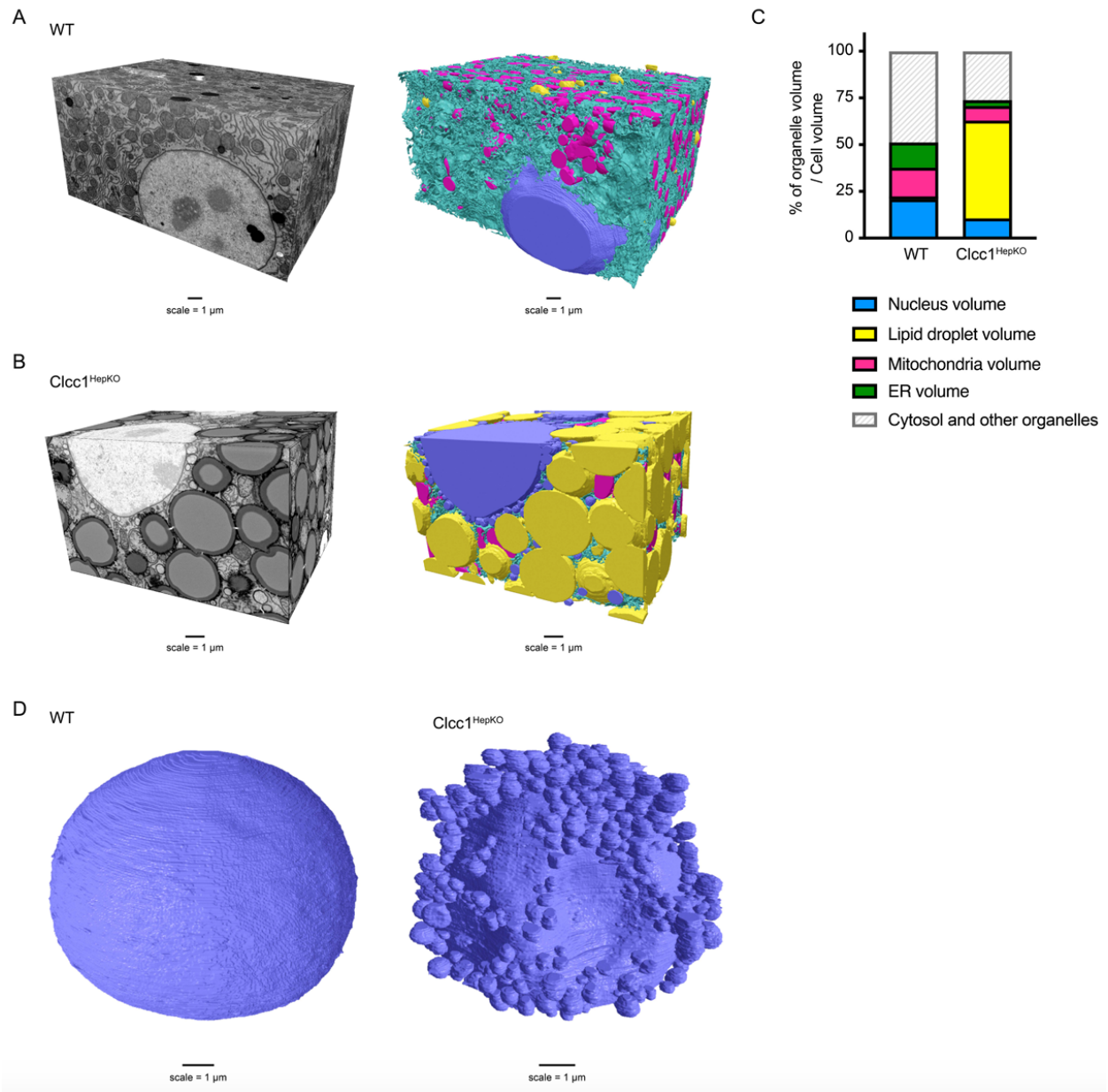

Figure 2-S16. Analysis of organelle architecture using FIB-SEM.
A,B) 3D reconstruction of FIB-SEM images and convolutional neural network based automated segmentation of liver volumes derived from liver volumes from WT (A) and Clcc1^{HepKO} (B) mice. ER (Cyan), mitochondria (magenta), LDs (yellow), and nucleus (purple). C) Quantification of organelle volume as a percentage of cellular volume in FIB-SEM reconstructions (A,B) from WT and Clcc1^{HepKO} mice. D) Reconstruction of segmented raw FIB-SEM data for nuclei (blue) from hepatocytes of WT and Clcc1^{HepKO} mice.

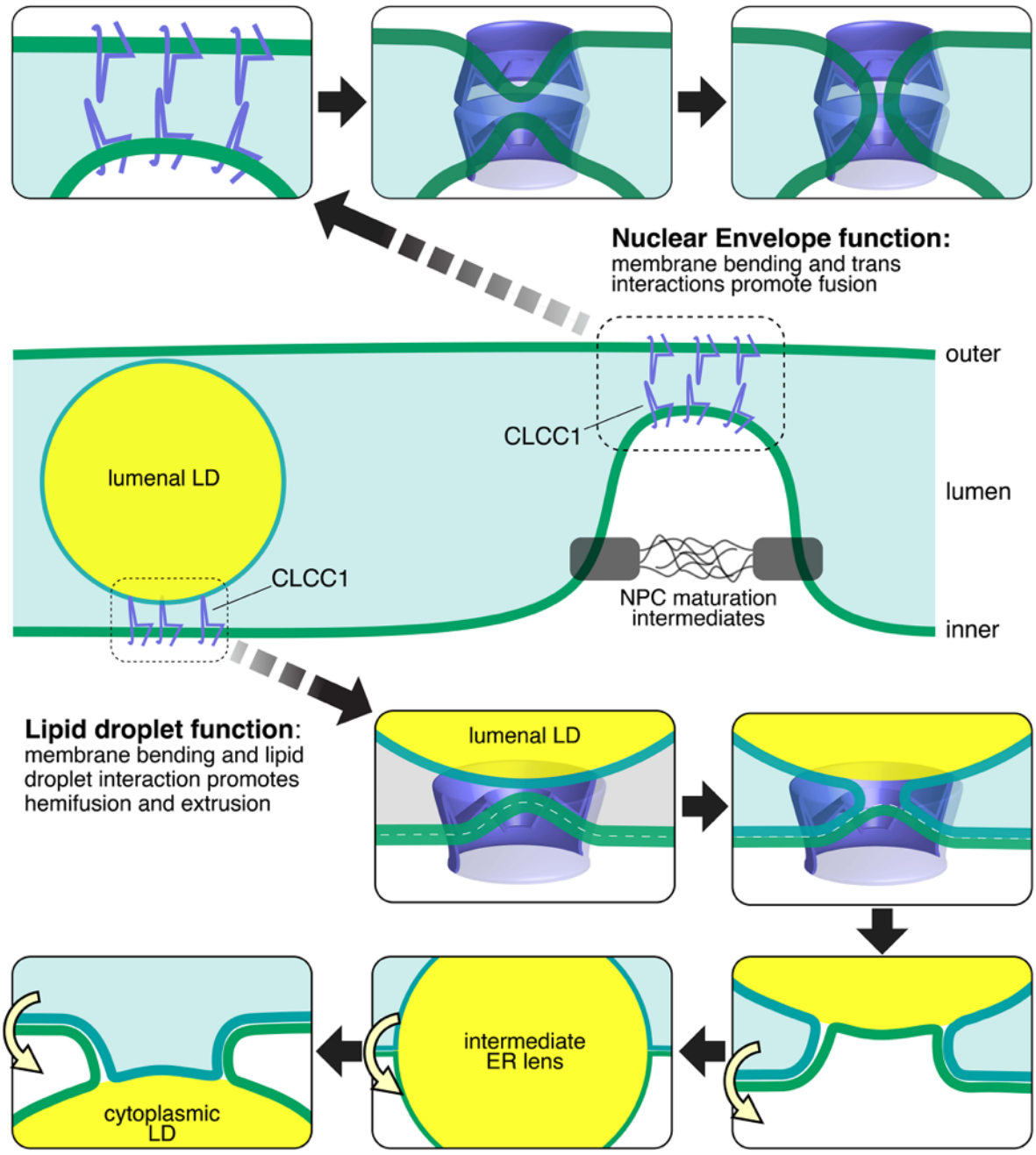

Figure 2-S17. Models of CLCC1 actions at the nuclear envelope and in the ER. Our findings provide strong evidence for a role of CLCC1 in nuclear pore assembly and ER neutral lipid channeling in hepatocytes. Similar to Brl1p and Brr6p in yeast, we propose that CLCC1 acts at the membrane fusion step of nuclear pore complex assembly, which is essential for the insertion of nuclear pores during interphase. Following the insertion of nuclear pore subunits into the inner nuclear membrane, CLCC1 may be recruited to form homo-oligomeric rings that face each other on opposing membranes. Each CLCC1 ring is predicted to bend the membrane towards the other across the lumen, potentially facilitating membrane fusion and perforation. Oligomeric

rings formed by Brl1p and its homologs would fulfil the same functions in yeast and organisms in all five eukaryote supergroups[54]. Within the ER, similar structural features of CLCC1 or CLCC1 homo-oligomers promote correct ER neutral lipid flux. In the absence of CLCC1 there is an aberrant increase in neutral lipid flux towards the ER lumen. One possible model is that CLCC1 reduces lumenal LD accumulation by mediating membrane fusion between the inner leaflet of the ER and the lumenal LD. This fusion would form a membrane bridge, allowing neutral lipids to migrate from the lumenal LD into the ER membrane, and emerge in cytosolic LDs. ER scramblases such as TMEM41B could act at this step to ensure that there are sufficient phospholipids for cytosolic emergence. This could represent an LD salvage pathway to provide a homeostatic balance for maintenance of correct amounts of lumenal and cytosolic LDs.

Chapter 3: IL32 and lipid droplet heterogeneity

3.1 Introduction

LDs are central hubs of cellular lipid metabolism, and as such must be able to store and release lipids rapidly in response to changing environments. LDs shuttle fatty acids to mitochondria for β-oxidation during starvation[109] and sequester lipids during periods of abundance to prevent lipotoxicity[1,108]. It is necessary to maintain a steady level of lipid storage to preserve energy homeostasis, and too few or too many LDs can have negative consequences for whole-body physiology[176,177].

Despite their known roles in a wide array of cellular processes, many details surrounding LD biogenesis and breakdown are not completely understood. To add to the complexity, the regulation and function of LDs must drastically change under environmental stressors—such as starvation[3], fatty acid overload[178] or inflammation[6]—yet the pathways that govern these responses are understudied. In Chapter 2, we performed genome-wide and metabolic state-dependent screens to identify a compendium of genes that modulate neutral lipid storage under a variety of conditions. Using data from these orthogonal screens, we generated a list of high-priority candidates that were either core regulators or metabolic state-dependent regulators of neutral lipid storage.

Many proteins that localize to the monolayer surface of LDs, known as the LD proteome, were high confidence regulators of lipid storage. The LD proteome is responsible for maintaining LD structure and stability and for performing biochemical reactions related to lipid storage. Some LD proteins had consistent effects on lipid storage across conditions, such as ABHD5 and ACSL3, many proteins exhibited a diversity of effects across metabolic conditions—GAPDH, HSD17B11, LSS, UBE2J2—or were only important under a single condition—LPCAT1, IL32, NDUFB6, RAB7A, VCP, VIM, VPS13C (Figure 3-1A).

Lipopolysaccharide (LPS), the major component of gram-negative bacterial membranes, induces LD biogenesis, and one of the LPS-dependent candidate regulators of lipid storage that emerged from the metabolic state-specific screens is IL32 (Figure 3-1B,C). IL32 is a secreted pro-inflammatory cytokine that the Olzmann Lab unexpectedly identified as an LD protein using proximity labeling proteomics[96]. We found that depletion of IL32 decreases cellular lipid storage under inflammatory conditions, though interestingly, IL32 only localizes to a subset of lipid droplets. We also developed a protocol to immunoprecipitate intact LDs using the LD-resident protein PLIN2, which can be optimized isolate to IL32-positive LDs to study LD heterogeneity. This project will advance an emerging function of LDs in innate immunity and inflammation, as well as address hypotheses surrounding LD heterogeneity.

3.2 Results

3.2.1 Depletion of IL32 causes a decrease in lipid storage under inflammatory conditions

A fascinating and common theme across bacterial and viral infection is the sudden upregulation of host LDs[8,179]. As LDs are concentrated “packets” of energy, it is attractive to hypothesize that viral and bacterial pathogens could use host lipids for nutrients and

membrane building blocks[6]. In addition, LDs are known to participate in the viral life cycle of hepatitis C virus[180,181] and SARS-CoV-2[182]. However, recent research has indicated that LD biogenesis is a protective host response to pathogenic infiltration[183]. This discovery is bolstered by recent findings that the LD localization of anti-bacterial proteins is important for their anti-bacterial activities[184,185]. These data argue against the dogma that LDs are simply fuel for the invading pathogen. Individual components of bacteria, such as LPS, or inflammatory cytokines like TNFα and IFNγ are known activators of IL32 expression[184]. 24h treatment with LPS, TNFα, IFNγ, or a combination of TNFα and IFNγ potently increased IL32 expression in Huh7 cells (Figure 3-2A).

Consistent with the results from the metabolic state-dependent screens, flow cytometry analysis shows that IL32-KO results in a decrease in lipid storage under inflammatory conditions (Figure 3-2B,C). By imaging, we determined that these LDs were both smaller and less abundant (Figure 3-2D,E), though more replicates of these experiments will need to be performed to determine statistical accuracy. This is corroborated by data in human patients where IL32 levels positively correlate with metabolic dysfunction steatohepatitis (MASH) severity and chronic hepatitis C[186] Incubation of liver organoids with IL32 also increases triglyceride levels[187]. Together, these data suggest a potential mechanism where IL32 is upregulated in response to inflammation and stabilizes LDs.

3.2.2 IL32 localizes to the surface of a subset of LDs

The phospholipid monolayer surrounding LDs is a unique structure that permits only specific protein structures. Class I proteins traditionally contain hydrophobic hairpins and traffic to LDs from the ER, and Class II proteins containing amphipathic helices or lipid modifications that intercalate between phospholipid head groups. LDs can serve as hubs to sequester non-metabolic proteins such as histones[188] or transcription factors[189], so it is conceivable that cytokines could also use LDs as intermediary carriers.

IL32 was detected in the buoyant fraction of Huh7 cells (Figure 3-3A) and on LDs in enterocytes and natural killer T (NKT) cells[190]. While most LD proteins exhibit non-discriminant localization to all LDs in the cell, not all the LDs within these cells were decorated with endogenous IL32, implying a selective subcellular targeting mechanism[190]. In Huh7 cells, IL32 only localizes to a subset of LDs in both untreated and pro-inflammatory conditions (Figure 3-3B-D). Induction of LDs with oleate also increases the abundance of IL32 on LDs, though still only to a subset of LDs (Figure 3-3B-D). There are some possibilities for this phenomenon: IL32 is preventing degradation of specific LDs, IL32 is marking LDs that contain antibacterial proteins, or IL32 uses LDs as a trafficking intermediate prior to export from the cell. Determining the cause of this intriguing localization pattern will be a novel advancement in our understanding of LD protein localization.

3.2.3 Immunoprecipitation of LD-resident proteins can pull down intact LDs

LPS treatment alters the LD proteome composition in mice, including the upregulation of several antibacterial proteins[184]. Lipophilic antimicrobial factors can also be sequestered within the hydrophobic interior of LDs, pointing toward a role for the neutral lipid core in the host-pathogen response[185]. Thus, it is likely that changes in the proteome or lipidome

could recruit IL32 to LDs, or IL32 expression cells during inflammation could change the LD proteome or lipidome. Therefore, it is essential to have a protocol to extract and analyze IL32-positive LDs.

The Olzmann Lab established a density-based protocol for isolating LDs from cells[96]. However, to analyze IL32-positive LDs, we developed a protocol to immunoprecipitate LD proteins and trap entire LDs (Figure 3-4A). Using a cell line expressing GFP tagged to endogenous PLIN2, we prepared cells in non-denaturing conditions, incubated lysate with anti-GFP beads for 2 hours at 4°C and boiled the sample to elute the LDs. We detected PLIN2-GFP as well as multiple LD proteins, including IL32, ATGL, and GAPDH (Figure 3-4B). Expression of exogenous IL32-GFP was shown to localize to the surface of a subset of LDs in Huh7 cells (Figure 3-4C), which can be used with this protocol to isolate IL32-positive LDs and perform subsequent lipidomics and proteomics.

3.3 Discussion

LD dysregulation lies at the center of many heritable and acquired conditions. Congenital lipodystrophies, or the inability to generate and utilize adipose tissue, have well-established causal mutations related to triglyceride storage, such as lipin1 in generalized lipodystrophy[191] and seipin in Berardinelli-Seip syndrome[192]. However, the majority of modern disease states are characterized by an overabundance of LDs, such as those seen in obesity, type II diabetes, and metabolic dysfunction-associated fatty liver disease (MAFLD)[191]. In each case, there is increased lipid storage in adipose tissue, with steatosis occurring in the liver or muscle. Interestingly, IL32 was recently identified as a biomarker for MAFLD patients since transcript levels drastically increase with disease severity and correlate with both hepatic fat levels and liver damage[186,193]. Therefore, understanding the tie between IL32 and lipid storage will have implications in both infectious and non-infectious disease research.

Many proteins directly involved in lipid metabolism, such as lipases and acyltransferases, localize to the LD monolayer. IL32 is the only known cytokine to localize to this monolayer, and this likely occurs through a predicted N-terminal amphipathic helix, though how IL32 only gets to certain LDs in unknown. LDs high in triglycerides or cholesterol esters recruit different proteins[194]. One attractive hypothesis is that lipidome changes as a result of LPS-treatment could recruit IL32 to specific LDs that are primed to fight bacteria. Yet whether endogenous or endocytosed IL32 traffics to membranes, or if IL32 on LDs is destined for secretion, remain open fields of study. Interestingly, our data show that IL32 only localizes to a subpopulation of LDs, likely to stabilize them during infection and inflammation (Figure 3-5). There are many possibilities for how and why this phenomenon may occur: IL32 is selectively targeting LDs for lipolysis or lipophagy, IL32 is marking LDs that contain antibacterial proteins, IL32 is at contact sites with other organelle membranes, etc. Establishing the reasoning for this localization will be fundamental for understanding protein compartmentalization and organelle heterogeneity.

3.4 Materials and methods

3.4.1 Cell lines and culture conditions

Huh7 and HEK293T cells were cultured in DMEM containing 4.5 g/l glucose and L-glutamine (Corning) supplemented with 10% FBS (Thermo Fisher Scientific and Gemini Bio Products), penicillin, and streptomycin. All cells were maintained at 37°C and 5% CO_2. Generation of endogenously labeled PLIN2-GFP Huh7 reporter cells are detailed in Roberts et al., 2023.

3.4.2 Plasmids and cloning

IL32 knockout cell lines were generated using the pMCB320 plasmid, a gift from M. Bassik (Addgene, 89359). Guide sequences for IL32 are as follows—sg1: GGGAGGAGCATTACCATT; sg2: GCCGGATCCTTGTCCCTCCA—and were selected from the Bassik Human CRISPR Knockout Library (Addgene, 101926, 101927, 101928, 101929, 101930, 101931,101932, 101933, 101934). Guide sequences were cloned into pMCB320 using the restriction enzymes BstXI and BlpI.

To generate lentiviral particles, lentiCas-Blast plasmid (Addgene, 52962) was co-transfected with third-generation lentiviral packaging plasmids (pMDLg/pRRE, pRSV-Rev, and pMD2.G) into HEK293T cells. Lentiviral media was collected 72 hr after transfection, passed through a 40 µm filter, and then used to infect Huh7 cells. Cells were selected in media containing 4 µg/ml blasticidin for 5 days. Active Cas9 expression was validated by flow cytometry analysis following infection with a self-cleaving mCherry plasmid (pMCB320 containing mCherry and an sgRNA targeting the mCherry gene).

3.4.3 Flow cytometry

Cells were washed 2x in DPBS, dissociated using TrypLE Express (Gibco, 12605010), collected by centrifugation at 500 x g for 5 min, and stained with 1 µg/µL BODIPY 493/503 or in DPBS on ice for 30 minutes.

For all flow cytometry assays, fluorescence was analyzed using an LSR Fortessa (BD Biosciences). The following filter sets were used: FITC (GFP, BODIPY 493/503) and Texas-Red (mCherry). FlowJo Software (BD Biosciences) was used to quantify fluorescence and generate representative histograms.

3.4.4 Immunoblotting

Cells were lysed in 1% SDS and sonicated at 15% amplitude for 15 seconds. Protein concentrations were determined and normalized using a BCA protein assay (Thermo Fisher Scientific, 23225). Equal amounts of protein by weight were combined with Laemmli buffer, boiled for 10 min at 95 °C, separated on 4–20% polyacrylamide gradient gels (Bio-Rad Laboratories) and transferred onto nitrocellulose membranes (Bio-Rad Laboratories). Membranes were incubated in 5% nonfat milk in PBS with 0.1% Tween-20 (PBST) for 30 min to reduce nonspecific antibody binding. Membranes were then incubated overnight at 4°C in PBST containing antibodies diluted in 5% BSA, followed by incubation for at least 1 hr in fluorescence-conjugated secondary antibodies diluted in

PBST containing 5% nonfat milk. Immunoblots were visualized on a LI-COR imager (LI-COR Biosciences), and Fiji/ImageJ was used for quantification of protein levels.

3.4.5 Fluorescence microscopy

For widefield microscopy of fixed cells, Huh7 cells were grown in 12-well plates on glass coverslips coated with poly-L-lysine. Cells were washed 3x with DPBS, fixed for 15 min in 4% (w/v) PFA in DPBS and washed 3x again with DPBS. Cells were permeabilized and blocked for 30 min with 5% BSA in DPBS containing 0.01% digitonin and then washed 3x with DPBS. Cells were incubated with an antibody to IL32 (R&D Systems, AF3040) diluted at 1:250 in 1% BSA in DPBS for 1 hr in the dark. Lipid droplets were stained with 1 µM BODIPY 493/503 for 30 minutes, nuclei were stained with 1 µg/mL DAPI, and primary antibodies were blotted with fluorescent secondaries (Abcam, GR3228336) diluted at 1:1000 for 30 min in the dark. Cells were washed 3x with DPBS and coverslips were mounted on 1 mm glass slides using Fluoromount-G (SouthernBiotech, 0100-01).

For live cell confocal microscopy, Huh7 cells were grown in 24-well glass bottom plates (170 µm coverglass bottom; Eppendorf, 0030741021; Cellvis, P24-1.5H-N). Cells were either untreated or treated with TNFα (20 ng/mL), IFNγ (10 ng/mL), and/or LPS (500 ng/mL) for 24 h. Lipid droplets were stained with 1 µM BODIPY 493/503 and nuclei were stained with 5 µg/mL Hoeschst 33342 for 30 minutes. Prior to imaging, cells were washed 2x with DPBS and imaged in fresh phenol red-free medium supplemented with 10% FBS. Live cells were imaged using an Opera Phenix Plus High-Content Screening System (Perkin Elmer) confocal microscope equipped with a 40X water immersion objective using DAPI and GFP filters. Cells were imaged at 37 °C with 5% CO2. Z-stacks of 0.3-µm slices were acquired. Images were merged and brightness and contrast adjusted using Fiji/ImageJ (https://imagej.net/software/fiji/). LDs were quantified by creating a custom analysis sequence using Harmony High Content Image Analysis Software, v4.9 (Perkin Elmer). For each field, maximum projection Z-stacks were processed with advanced flatfield correction. Nuclei and cytoplasm were defined using the DAPI and GFP channels, respectively, and border cells were automatically excluded from analyses. LDs were defined using the “Find Spots” building block (Lipi-Green stain, GFP channel), thresholding for size, intensity, and roundness. For each cell, lipid droplet number and area were quantified. LD quantification data were graphed and analyzed in Prism 9 (GraphPad).

3.4.6 Immunoprecipitation of LDs

WT or endogenously-tagged PLIN2-GFP cells were untreated or treated with 100 µM oleate or 20 ng/mL TNFα + IFNγ and grown until confluent in 10 cm^2 plates. Cells were scraped harvested in DPBS, centrifuged for 10 min at 500 x g, and resuspended in 100 µL HLM buffer with protease inhibitor. Samples were dounced 80 times, centrifuged at 1000 x g for 10 min, and the upper fraction was collected. Beads were centrifuged at 700 RPM for 2 min at 4°C, wash 2x with 390 uL HLM buffer, and resuspend in 130 uL HLM buffer. 30 µg of lysate was collected for Western blotting and 650 µg of each sample was incubated with 130 µL GFP bead resin on an end-over-end rotating rocker for 2 h at 4°C. Samples were placed in a magnetic rack to collect beads and remove

unbound/flowthrough (~500 uL). Beads were washed 1x with 300 uL HLM + PI and eluted using 100 uL 2.5X loading dye in HLM + PI and boiled at 95°C for 5 min. To run the Western blot, 30 ug lysate, 10 uL flowthrough, 10 uL washes, and 10 uL elution were diluted 1:2 5X loading dye + 50 uL HLM + PI.

3.4.7 Statistical analysis with Prism

All statistical analyses were performed using Prism 9 (GraphPad). For each panel, the number of biological replicates (n), *p*-values, and statistical tests employed are reported in figure legends and methods.

3.5 Figures

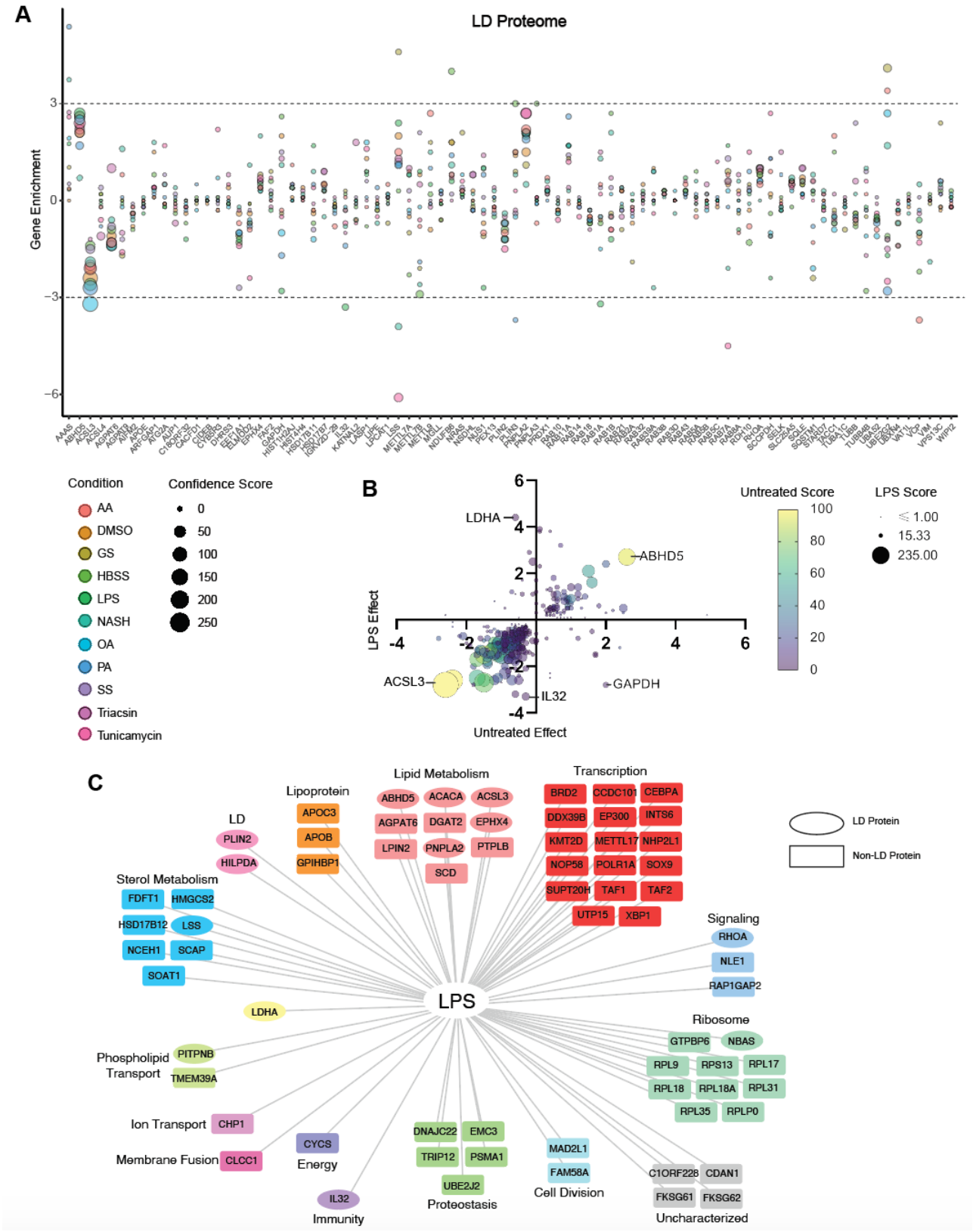
A
LD Proteome
Gene Enrichment
3
0
−3
−6
Condition
AA
DMSO
GS
HBSS
LPS
NASH
OA
PA
SS
Triacsin
Tunicamycin
Confidence Score
0
50
100
150
200
250
B
LDHA
ABHD5
ACSL3
GAPDH
IL32
LPS Effect
Untreated Effect
Untreated Score
LPS Score
≤ 1.00
15.33
235.00
C
LD
PLIN2
HILPDA
Lipoprotein
APOC3
APOB
GPIHBP1
Lipid Metabolism
ABHD5
ACACA
ACSL3
AGPAT6
DGAT2
EPHX4
LPIN2
PNPLA2
PTPLB
SCD
Transcription
BRD2
CCDC101
CEBPA
DDX39B
EP300
INTS6
KMT2D
METTL17
NHP2L1
NOP58
POLR1A
SOX9
SUPT20H
TAF1
TAF2
UTP15
XBP1
Sterol Metabolism
FDFT1
HMGCS2
HSD17B12
LSS
NCEH1
SCAP
SOAT1
LDHA
LPS
Signaling
RHOA
NLE1
RAP1GAP2
Ribosome
GTPBP6
NBAS
RPL9
RPS13
RPL17
RPL18
RPL18A
RPL31
RPL35
RPLP0
Phospholipid Transport
PITPNB
TMEM39A
Ion Transport
CHP1
Membrane Fusion
CLCC1
Energy
CYCS
Immunity
IL32
Proteostasis
DNAJC22
EMC3
TRIP12
PSMA1
UBE2J2
Cell Division
MAD2L1
FAM58A
Uncharacterized
C1ORF228
CDAN1
FKSG61
FKSG62
LD Protein
Non-LD Protein

Figure 3-1. LD proteins regulate lipid storage under different metabolic states.
A) casTLE effects and scores of Huh7 LD proteins[8] across all metabolic conditions tested in chapter 2. Node colors represent metabolic states and node sizes represent confidence scores. Plot was made using *ggplot2* function in *R*. B) Pairwise comparison of untreated and LPS conditions from metabolic state-dependent screens. Node color represents confidence score in the untreated condition and node size represents confidence score in the LPS condition. C) Neutral lipid regulators under LPS treatment, distributed by function. Oval nodes represent LD proteins and rectangle nodes represent non-LD proteins.

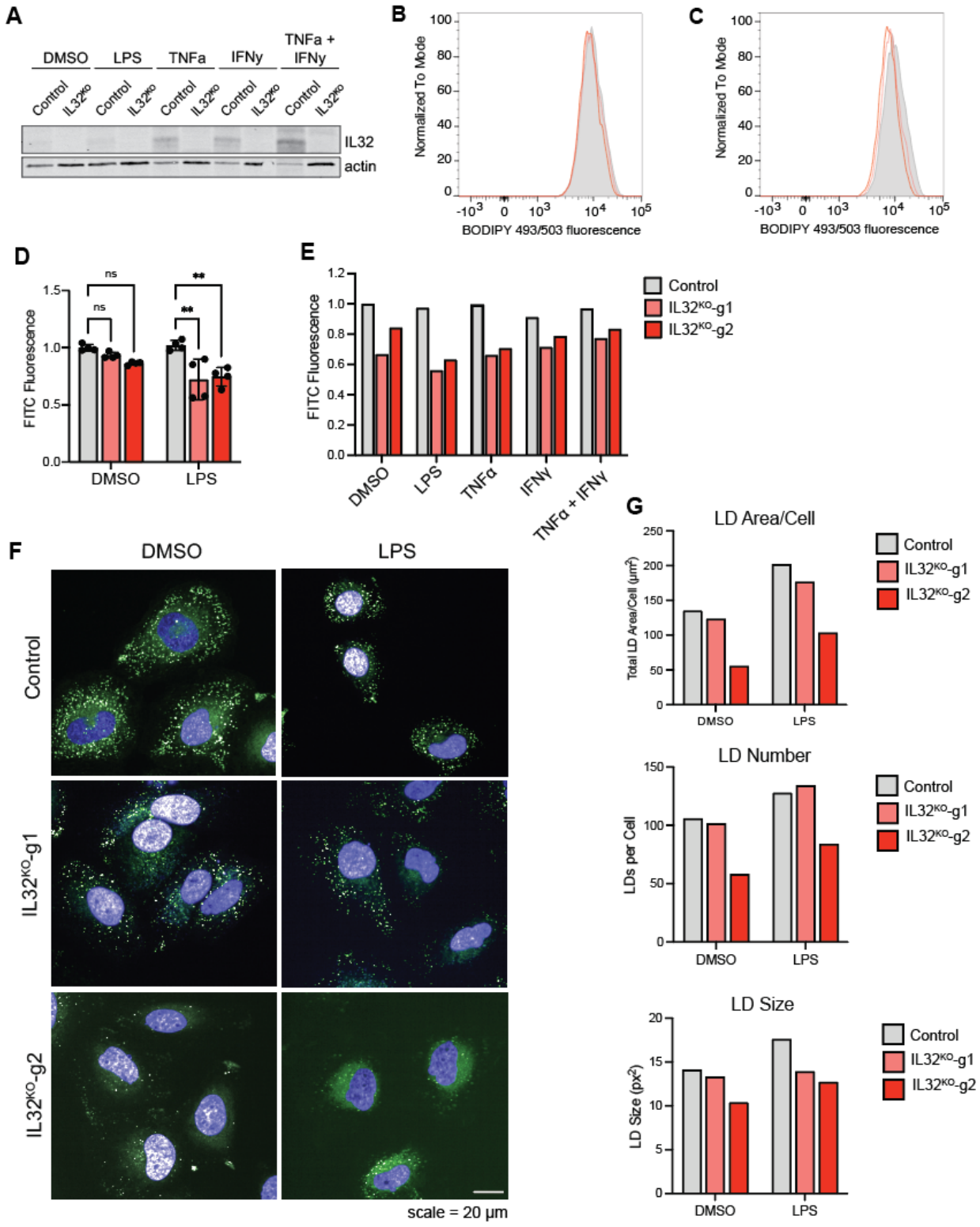
A
DMSO
LPS
TNFa
IFNy
TNFa + IFNy
Control
IL32KO
IL32
actin
B
Normalized To Mode
BODIPY 493/503 fluorescence
C
Normalized To Mode
BODIPY 493/503 fluorescence
D
FITC Fluorescence
ns
**
DMSO
LPS
E
FITC Fluorescence
Control
IL32KO-g1
IL32KO-g2
DMSO
LPS
TNFα
IFNγ
TNFα + IFNγ
F
DMSO
LPS
Control
IL32KO-g1
IL32KO-g2
scale = 20 µm
G
LD Area/Cell
Total LD Area/Cell (µm²)
LD Number
LDs per Cell
LD Size
LD Size (px²)
Control
IL32KO-g1
IL32KO-g2
DMSO
LPS

Figure 3-2. Depletion of IL32 causes a decrease in lipid storage under inflammatory conditions.
A) Immunoblot analysis of IL32 levels in control and $IL32^{KO}$ cells untreated or treated with TNFα (20 ng/mL), IFNγ (10 ng/mL), and/or LPS (500 ng/mL) for 24 h. B-C) Representative flow cytometry histograms of control and $IL32^{KO}$ Huh7 cells following no treatment or treatment with 500 ng/mL LPS for 24 h. D) Quantification of the amount of neutral lipid from flow cytometry histograms in B. E) Quantification of the amount of neutral lipid from flow cytometry of cells treated with TNFα (20 ng/mL), IFNγ (10 ng/mL), and/or LPS (500 ng/mL) for 24 h. F) Representative confocal images of lipid droplets using BODIPY 493/503 in control (expressing safe targeting sgRNA) and $IL32^{KO}$ cells under basal conditions or following treatment with 500 ng/mL LPS for 24 h. G) Quantification of the number and size of LDs from (F). Data represent mean ± SD of > 100 cells in one biological replicate.

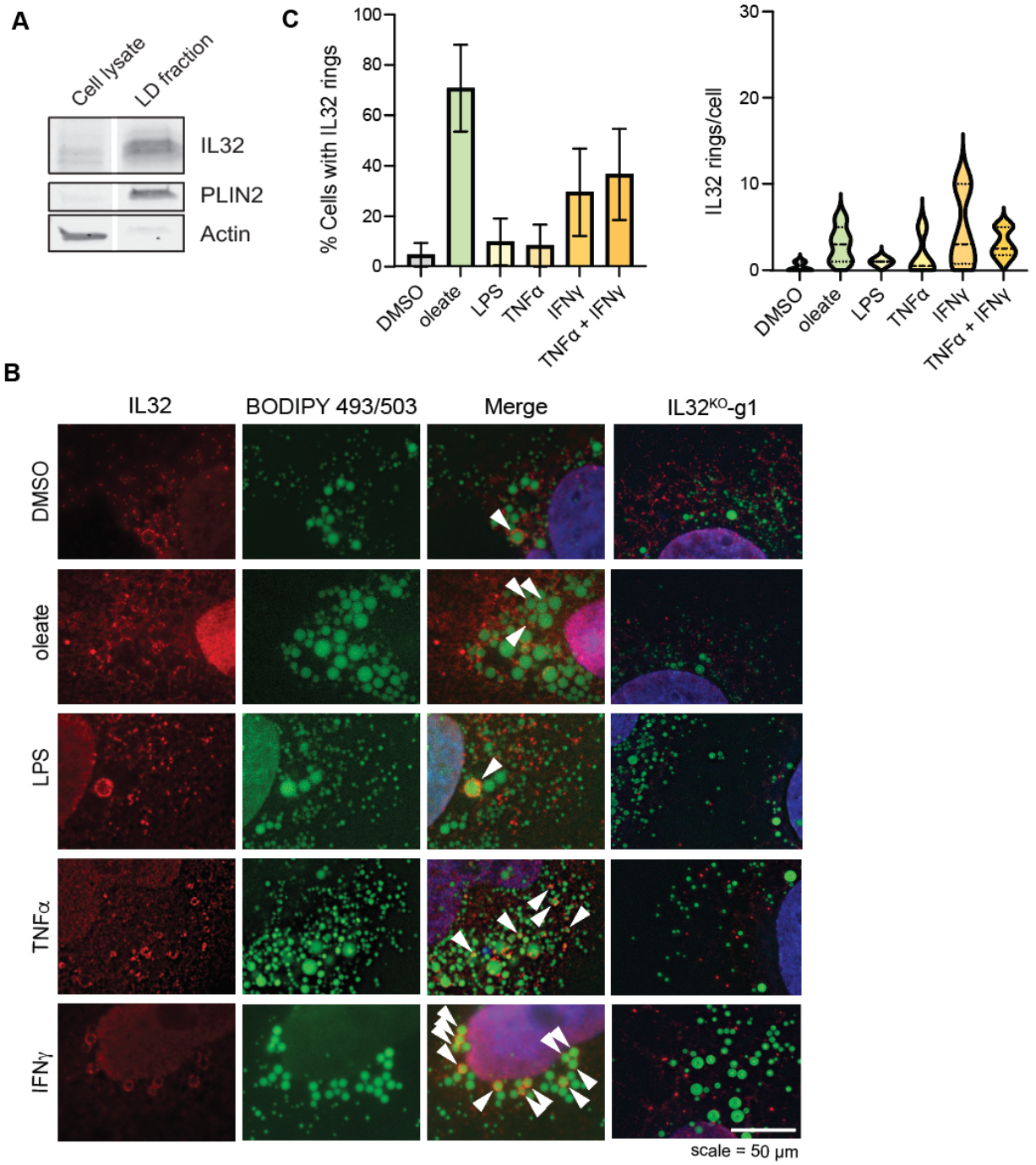

Figure 3-3. IL32 forms rings around a subpopulation of LDs.
A) Immunoblot analysis of IL32 and PLIN2 levels from whole cell lysate and the buoyant fraction of WT Huh7 cells. B) Representative fluorescence microscopy images of IL32 and LDs in control and IL32^{KO} cells treated with 100 μM oleate, TNFα (20 ng/mL), IFNγ (10 ng/mL), or LPS (500 ng/mL) for 24 h. IL32 was labeled with goat anti-IL32 antibody (red), LDs were stained with 1 μg/mL BODIPY 493/503 (green), and the nuclei was stained with DAPI. Scale bar represents 50 μm. C) Quantification of the number of cells with IL32 rings and the number of IL32 rings/cell in B.

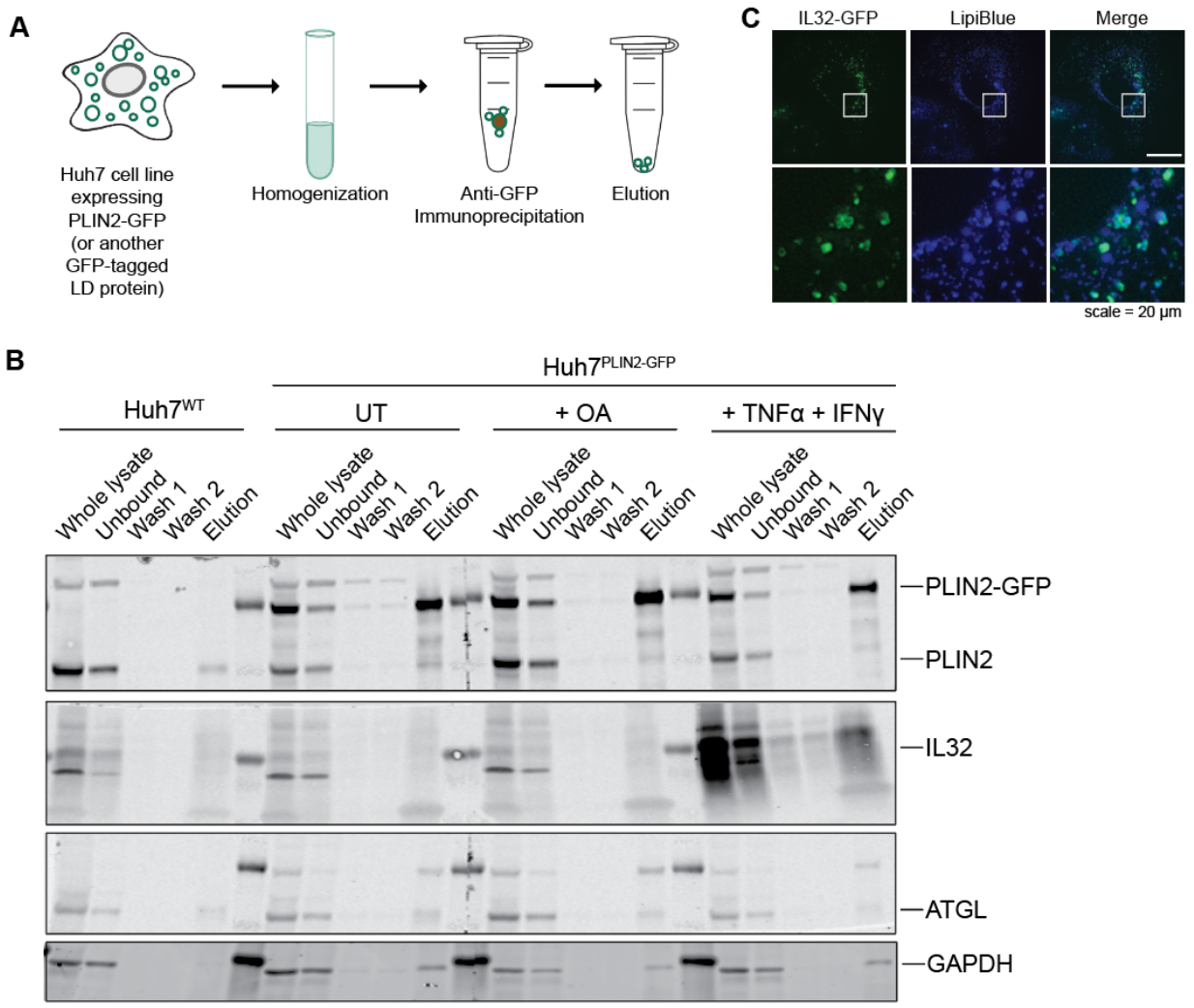

Figure 3-4. Immunoprecipitation of intact LDs.
A) Schematic of LD immunoprecipitation through trapping of GFP-tagged LD protein. B) Immunoblot analysis of whole cells, washes, and elutions to immunoprecipitated LDs through trapping of PLIN2-GFP. Cells without PLIN2-GFP *(left)* were a negative control. PLIN2-GFP cells were untreated, treated with 100 µM oleate, or 500 ng/mL LPS for 24 h before immunoprecipitating. C) Representative fluorescence microscopy images of cells overexpressing IL32-GFP. LDs (blue) were stained with 500 nM Lipi-Blue. Scale bar represents 20 µm.

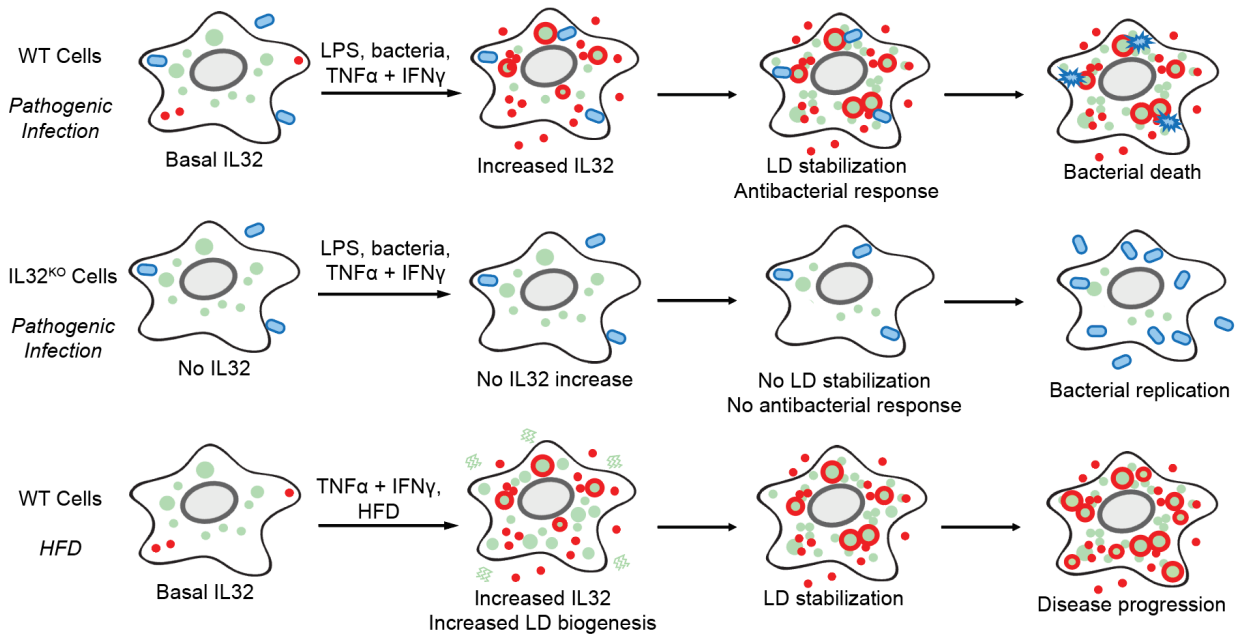

Figure 3-5. Hypothetical role of IL32 in lipid droplets and immunity.
Model depicting the cellular function of IL32 in response to immune stimuli. *Top:* In WT cells, IL32 levels increase in response to LPS, cytokines, or bacteria and localize to a subpopulation of LDs. This response could stabilize LDs as anti-immunity platforms, thereby increasing the ability to fight off pathogens. *Middle:* In IL32^{KO} cells, there is no response to immune stimuli, leading to no stabilization of LDs subsequent lack of antibacterial response. *Bottom:* In MASH patients, IL32 levels can still increase in response to increased inflammation, thereby leading to LD stabilization and disease progression.

Chapter 4: Protocol for performing pooled CRISPR-Cas9 loss-of-function screens

Contents in this chapter are modified from the previously published protocol paper:

Mathiowetz, A. J., Roberts, M. A., Morgens, D. W., Olzmann, J. A. & Li, Z. Protocol for performing pooled CRISPR-Cas9 loss-of-function screens. *STAR Protoc.* 4, 102201 (2023).

4.1 Introduction

Genetic screens are powerful, unbiased discovery approaches to systematically elucidate the genes involved in a process or phenotype of interest. With the emergence of CRISPR-Cas9 genome editing tools, the multitude of readily available single guide RNA (sgRNA) libraries, and the improved accessibility of CRISPR screen analysis pipelines, genetic screens in mammalian cells are rapidly becoming an indispensable staple of cell biology research. These screens include both loss-of-function, CRISPR knockout (KO) and CRISPR interference (CRISPRi), and gain-of-function, CRISPR activation (CRISPRa), screens. In a typical pooled CRISPR screen, an sgRNA plasmid library is introduced using viral based transduction into pools of cells expressing the appropriate Cas9 version – Cas9 for CRISPR KO, dCas9 fused to a transcriptional repressor for CRISPRi, and dCas9 fused to a transcriptional activator for CRISPRa. Cells expressing unique sgRNAs are then selected based upon a phenotype of interest, such as altered viability following a treatment or a change in the levels of a fluorescent reporter. The sgRNAs that influence the phenotype are then identified by deep sequencing and bioinformatics programs that quantify sgRNA enrichment between controls and treatments.

The screens performed in these studies are generalizable and can be readily employed to address a myriad of cell biology questions that provide selectable phenotypes. Here, we provide a step-by-step protocol for designing, performing, and analyzing pooled CRISPR KO screens in mammalian cells using either cell viability or fluorescent reporters as selection methods (Figure 4-1 and Figure 4-2).

4.2 Step-by-step protocol

4.2.1 Generate Cas9-expressing cells

Timing: 4 weeks

The CRISPR-Cas9 system includes two main parts: the Cas9 endonuclease and targeting sgRNAs. Both components can be introduced together or separately through lentiviral transduction. This integrates Cas9 and sgRNAs non-specifically into the genome, which is appropriate for almost all CRISPR screens in immortalized cells. However, if Cas9 needs to be expressed more specifically, such as when using stem cells, it can be expressed from a safe harbor locus[195]. In this protocol, we induce constitutive Cas9 expression through lentiviral transduction. Cas9 is then stably expressed and remains active throughout the screening process.

1. Plate 300,000 HEK293T cells into one well of a 6-well culture plate in 1 mL DMEM + 10% FBS such that they are at ~50% confluence 24 h later.
2. After 24 h, transfect HEK293T cells with Mirus LT1 transfection reagent, 500 ng 3rd generation lentiviral packaging vector mix (equal parts pMDLg/pRRE [Addgene # 12251], pRSV-Rev [Addgene # 12253], and pMV2.g [Addgene # 12259]), and 500 ng pLenti-Cas9-blast (Addgene # 52962) at a 3:1 Mirus:DNA ratio. Follow Mirus Bio's "TransIT-LT1 Full Transfection Protocol".

CRITICAL: To ensure sufficient viral titers are reached, all library and packaging plasmids should be endotoxin-free and the packaging HEK293T cells need to be healthy prior to transfection.

3. Incubate cells for 72 h.
4. After 72 h, collect viral supernatant through a 0.45 µm filter. Use immediately or store at 4°C for up to one week or −80°C for up to six months.

CRITICAL: When working with lentivirus, bleach all media and supplies and turn on ultraviolet light in the biosafety cabinet for thirty minutes to inactivate viral particles.

5. Plate 100,000 Huh7 cells into two wells of a 6-well tissue culture plate in DMEM + 10% FBS such that cells are at ~80% confluence 24 h later.
6. After 24 h, introduce 0.5 mL fresh DMEM + 10% FBS and 0.5 mL pLenti-Cas9-blast lentivirus-containing medium to the cells in one well with 8 µg/mL polybrene. Incubate for 24 h.

Note: Keep one well uninfected as a control for the antibiotic selection.

7. After 24 h, remove viral media and replace with DMEM + 10% FBS.
    a. Expand cells for 24 h and then begin antibiotic selection with 4 µg/mL blasticidin.
    Note: With the amount of lentivirus added in step 6, ~30%–50% of cells should be infected. Cells can therefore start selection at high confluency and not overgrow the plate.
    b. Replace the selection media every 3–4 days and split cells as necessary until all control cells have died.
    Note: The concentration of selection antibiotic is dependent on the cell line. This concentration should be determined in advance with antibiotic kill curves.
8. Once all control cells have died, replace media for Cas9 cells with fresh DMEM + 10% FBS without antibiotic to allow cells to recover. These are now your “Cas9” cells.

Note: Cas9 pools or clonal cells can be used for CRISPR screening. To avoid clonal bias from the genetic background, we screen pools of Cas9 cells and do not select monoclonal cells.

9. Validate Cas9 expression by Western blot (Figure 4-3A).
10. Freeze cells at −80°C and store in liquid nitrogen.

Note: It is useful to expand these cells and store in excess since they can be used for subsequent screens or individual gene knockouts.

Note: After introduction into cells, it is important to make sure that Cas9 is active (steps 11-16). To test Cas9 activity, independently infect cells with a lentiviral plasmid encoding:

1. mCherry plus a non-targeting sgRNA (control) and 2. mCherry plus an mCherry-targeting sgRNA (Figure 4-3B). Employ flow cytometry to measure mCherry expression (Figure 4-3C). Cells expressing active Cas9 will cleave the mCherry DNA and appear as an mCherry negative population. Conversely, cells lacking active Cas9 will fail to cleave the mCherry DNA and appear as an mCherry positive population. Due to the long half-life of mCherry, it may take up to 1–2 weeks to distinguish the active Cas9 (e.g. mCherry-negative) cells.

11. Repeat steps 1–4 to make lentiviral media containing a control sgRNA or mCherry-targeting sgRNA (see key resources table for sequences) cloned into pMCB320 lentiviral vector (Addgene # 89359).
12. Plate 100,000 Huh7 Cas9 cells into three wells of a 6-well plate in DMEM + 10% FBS so that cells reach ~80% confluence 24 h later.
13. 24 h, introduce viral media containing the control sgRNA or the mCherry-targeting sgRNA cloned into the pMCB320 lentiviral vector with 8 µg/mL polybrene to two of the wells. Incubate for 24 h.

Note: Keep one well uninfected for antibiotic selection.

14. After 24 h, remove viral media and replace with DMEM + 10% FBS. Expand cells for 48 h and then begin antibiotic selection with 2 µg/mL puromycin (see note above on antibiotic concentrations). Replace the selection media every 3–4 days until all control cells have died.
15. Once all control cells have died, replace media with fresh DMEM + 10% FBS without antibiotics to allow cells to recover.
16. Measure mCherry fluorescence by flow cytometry to validate Cas9 activity (Figure 4-3B,C).

4.2.2 Dose response analysis to determine concentration of cytotoxic compounds

Timing: 3–4 days

An optimal concentration of your choice compound to induce cell death is crucial to achieving the maximum dynamic range of the screen readout. For a drug-resistance screen, we suggest determining a sub-lethal concentration of drug that causes very modest cell death (~5%) in 24-48 h. Presumably, the depletion of a drug resistance factor will lead to a substantial increase in the sensitivity to the drug (Figure 4-4A,B), leading to a depletion of the sgRNA over time. For a drug-sensitivity screen, we recommend an initial drug concentration that causes ~50% cell death. However, as pools of surviving cells from the initial selection will become resistant to cell death induced by the drug, a slightly higher concentration may be required for each subsequent treatment cycle to achieve ~50% death.

Note: This is a specific example for identifying ferroptosis resistance factors using known ferroptosis inducing compounds. However, this protocol can be extrapolated to any treatment or condition that provides a selective pressure on cell viability.

Note: Huh7 and U-2 OS cells were used in our original studies[144,196], and the data used to generate Figures 4A-B were collected from U-2 OS cells. However, the protocol steps to test dose-response cytotoxicity can be applied to any cell type.

17. On day 0, seed ~5,000 U-2 OS cells in each well of a 96-well plate such that the final volume per well is 200 µL.
18. On day 1, aspirate the media from the 96 well-plate and replace it with 100 µL fresh media.
19. Prepare a 2× final solution of the compound at varying concentrations by serial dilution in media containing 60 nM SYTOX Green Dead Cell Stain.

Note: 8–12 different concentrations are recommended to ensure that the optimum concentration is within the standard curve. We usually begin with a 10-point, 5-fold dilution series.

20. Slowly add 100 µL compound containing media back to each well so that the final volume of media in each well is 200 µL with 30 nM SYTOX Green Dead Cell Stain.
21. Monitor cell death using an Incucyte Live-Cell Analysis System (Essen Biosciences), taking images every 2 h for 24–48 h total. Dead cells will be SYTOX green-positive.
22. On day 2 or 3, determine the percentage of cell death by dividing the number of dead cells (SYTOX green-positive) by the total number of cells (visualized by phase imaging).

Note: Due to some limitations of the Incucyte system and the dramatic difference in cell morphology, thresholding and automatically counting total cell number using phase images can sometimes be difficult and inaccurate. Generating a cell line that stably expresses mCherry or using a genetically encoded live-cell nuclear marker (e.g., Incucyte Nuclight reagents) greatly improves the accuracy of the counting for live cells.

Note: If an Incucyte Live-Cell Analysis System is not available, a CellTiter-Glo 2.0 Cell Viability Assay can be used to determine the sub-lethal dose of the drug.

23. Choose a concentration of drug that results in ~5% cell death. Use this concentration for the CRISPR screen (Figure 4-4A,B).

4.2.3 Determine the dynamic range for fluorescence-based assays

Timing: 1 week

The confidence of screen results depends on the dynamic range of the fluorescence reporter. A greater distance between the high and low fluorescence intensity bins will result in less biological noise and will increase the confidence of positive results and reduce the occurrence of false positives and negatives[197]. When possible, it is useful to determine the dynamic range of a cell population using a positive control prior to screening to ensure that cells with altered phenotypes can be accurately sorted by FACS.

Note: Fluorescence can arise from a fluorescent reporter protein or a fluorescent dye. To obtain the highest dynamic range from a reporter protein, it may be useful to sort cells to obtain a population with uniform fluorescence levels. For fluorescent dyes, test multiple concentrations and incubation times.

Note: It is important to establish the timeframe and treatment conditions before performing the screen itself. For example, it may take several days for a genetic perturbation or drug to produce a measurable effect on a fluorescent reporter. Cells may also need to be differentiated or pretreated with drugs or nutrients. Therefore, optimize conditions and establish a timeline for seeding cells, inducing genetic perturbations, differentiating (if applicable), and treating cells, and carry it over to the screen to yield the most robust results.

24. Choose a positive control gene (if possible) that is known to influence levels of the fluorescent reporter. Generate a knockout cell line or treat cells with a drug targeting the positive control protein. Confirm that the expected increase or decrease in fluorescence is detectable by flow cytometry.
25. Measure fluorescence by flow cytometry to validate that a change in fluorescence is detected and to determine the dynamic range of your assay (Figure 4-4C).
    a. In this example, Huh7 cells were treated with 1 μg/mL triacsin C or 100 μM oleic acid to deplete or increase neutral lipid storage, respectively. Cells were treated with 1 μg/mL BODIPY 493/503 to label neutral lipids and fluorescence was measured by flow cytometry. The 10× decrease and 5× increase in fluorescence intensity will be the target dynamic range of fluorescence for this CRISPR screen.

Note: Fluorescence intensity can diminish over time. Incubate cells on ice for multiple hours (as long as the FACS sort will be) and check that fluorescence does not change during sorting. We have not found this to be an issue with GFP-based reporters. If necessary, cells can be fixed prior to FACS to ensure fluorescent marker stability over time.

Note: In some cases, there are no drugs or known regulators to manipulate or validate the system. In the absence of a positive control to validate the fluorescence reporter, it is possible to move directly to the screen.

4.2.4 Prepare sgRNA library

Timing: 3 days

Many genome-scale and small-scale libraries are deposited on Addgene. For our experiments, we used the Bassik Human CRISPR Knockout Library (Addgene # 101926-101934), which is composed of 9 sublibraries, or our custom Human Lipid Droplet and Metabolism Library (Addgene # 191535). Each sgRNA library will need to be amplified and packaged into lentivirus. Alternatively, pre-packaged lentivirus can be purchased directly from Addgene.

Note: Certain biological questions may require genome-wide screens, and others may be more accurately addressed using specialized libraries based on gene function. The number and availability of resources (e.g., cell culture supplies, equipment booking, etc.) also differs drastically between a genome-wide screen and a smaller custom library-based screen. Additionally, CRISPR libraries from different sources may contain a different number of sgRNAs per gene or may work by delivering multiple sgRNAs to individual cells (e.g., one sgRNA on a single plasmid vs. multiple sgRNAs on a single plasmid), which can be a consideration when calculating the amount of time needed to complete a screen. For more information on this subject and for designing a custom CRISPR library, see previous descriptions[198].

26. Follow the Bassik Lab's "Liquid Culture Library Plasmid Re-amp Protocol"[130,196,199].
27. Measure DNA concentration using the Qubit dsDNA HS Assay.
28. For quality control, send the library for deep sequencing by following the "preparing for deep sequencing" step. Measure sgRNA diversity according to step 29 of the main protocol.

4.3 Step-by-step methods details

4.3.1 Making virus, infecting cells, selecting, and growing

Timing: 4 weeks

CRITICAL: Maintaining coverage, or representation of sgRNAs, is extremely important at all stages of screening. Higher coverage reduces potential bottlenecks and background sampling noise[197]. We and collaborators have empirically determined that 200 cells/sgRNA at infection and 1000 cells/sgRNA during selection, growth, and sequencing are sufficient for high-confidence results[200] (Figure 4-5).

1. Plate 7.5×10^6 HEK293T cells into a 150 mm culture plate in 30 mL DMEM + 10% FBS for ~50% confluence 24 h later.
2. After 24 h, transfect HEK293T cells with Mirus LT1 transfection reagent, 8 µg lentiviral packaging vector mix, and 8 µg library lentiviral plasmid at a 3:1 Mirus:DNA ratio.

CRITICAL: To ensure sufficient viral titers are reached, all library and packaging plasmids should be endotoxin-free and the packaging HEK293T cells need to be healthy prior to transfection.

3. Incubate cells for 72 h.
4. After 72 h, collect viral supernatant through a 0.45 µm filter. Use immediately or store at 4°C for up to one week or −80°C for up to six months.

Note: Most pooled CRISPR screens rely on the assumption that all sgRNAs are represented and that there is only one sgRNA per cell. Before infection, viral titer is estimated by serial dilution. Cells should be infected with the volume of virus that results in a 20%–50% mCherry positive population 72 h after infection.

Note: Virus can be concentrated using viral precipitation solution (e.g., ALSTEM # VC100).

5. Plate 10 × 10^6 Huh7 cells into a 245 mm culture plate in DMEM + 10% FBS such that cells are at ~80% confluence 24 h later.
6. After 24 h, introduce sgRNA-containing viral medium to the cells in one well with 8 μg/mL polybrene. Incubate for 24 h.

Note: Cells should be infected with an expectation that 20%–50% will express mCherry 72 h post-infection, and the number of infected cells should be at least 200× coverage.

7. After 24 h, remove all media and replace with DMEM + 10% FBS.
8. Trypsinize and re-seed all cells into new plates at ~40%–50% confluence. Expand for another 24 h.
9. After 24 h, begin antibiotic selection by replacing media with DMEM + 10% FBS containing 2 μg/mL puromycin. Replace the selection media every 3–4 days until all control cells have died.

Note: 1000× coverage (e.g., 1,000 cells per sgRNA) should be maintained during selection and throughout the rest of the screening process.

10. Once all the control cells have died, replace media with fresh DMEM + 10% FBS without antibiotic to allow for recovery.
11. Freeze cells at −80°C and store in liquid nitrogen.

Note: We recommend freezing multiple vials of cells at 2000× coverage before phenotypic selection to ensure there will be enough cells for multiple conditions and/or biological replicates.

4.3.2 Antibiotic selection

Timing: 1 week (FACS-based), 2–3 weeks (death-based)

12. Thaw cells in excess (2000× coverage) to prevent loss of coverage if cells die during thawing. Passage after 48 h and grow for another 48 h (96 h total).

CRITICAL: The number of passages and duration of growth can affect cellular phenotypes due to genetic compensation. When performing replicates or using multiple libraries in the same experiment, cells should be grown for the same number of days/passages.

The parameters of the following steps will differ depending on whether the phenotypic selection is fluorescence-based or death-based.

13. Fluorescence-based screen.
    a. Treat cells (if applicable).

b. Trypsinize (if using adherent cells) and collect cells in excess of 1000× coverage in FACS sorting media.

Note: We recommend trypsinizing cells at >3000× coverage before FACS sorting to maintain a buffer in case of technical error and to account for sorting out any non-fluorescent cells. The number of cells that will be collected from cell sorting will be 1000× (500× in each gate). Sort cells and collect high and low fluorescence bins.

Note: The FACS buffer used will depend on the characteristics of the cell line to be sorted. We use phenol red-free DMEM containing 3% FBS and 1% BSA for Huh7 cells.

Note: The size of high-reporter and low-reporter bins affects the quality of screen data. A study[5]. computationally determined that collecting the highest 25% and lowest 25% bins results in the greatest signal-to-noise ratio. However, bin sizes can be altered depending on the biological question[200]. We have collected the top and bottom 30% fluorescence bins[3] and recommend these parameters for FACS-based screens.

c. After sorting, spin cells at 500 × g for 10 min. Carefully aspirate FACS buffer and wash once with PBS. Spin cells again at 500 × g, remove PBS, and store cell pellets at −80°C.

14. Death-based screen.
    a. Trypsinize and collect cells in media containing 10% FBS.
    b. Count cells and seed in 245 mm square TC-treated culture dishes at 10% confluence (8–15 × 10^6 cells, depending on the cell size).

Note: The total amount of cells seeded should be above 1000× coverage. Use a minimum of 60 mL cell culture media containing the drug or vehicle at the desired concentration (determined in *Before you begin*) for each plate.

c. Replace the media and drug/vehicle every 3 days and continue culturing the cells until they are confluent.
d. Repeat steps 14b–c until vehicle control treated cells divide >10 times (doubling cycles).
e. When cells reach >10 doubling cycles, harvest cells by trypsinization and wash once in media containing 10% FBS and once with PBS.
f. Spin cells at 500 × g for 5 min, aspirate PBS, and store cell pellet at −80°C. Each cell pellet should contain cells at >1000× coverage.

4.3.3 Preparing for deep sequencing

Timing: 1 week

To identify the sgRNAs present in each cell population, genomic DNA (gDNA) is extracted from frozen cell pellets and guide sequences are amplified by PCR.

CRITICAL: Cross contamination of libraries poses a huge risk to the integrity of screen results. To avoid contamination, some labs have designated spaces and hoods for these steps. At the very least, it is essential to thoroughly clean workspaces and equipment

(e.g., pipettes, tube racks) with RNase Away (Thermo # 7002PK) or ELIMINase (Decon Labs # 1101) before the experiment and routinely wipe the bench surface and all pipettes during sample processing. Filtered pipette tips are essential. We recommend having a set of designated equipment for DNA processing.

15. Extract gDNA from cell pellets using Qiagen QIAamp DNA Blood Midi Kit (Cat # 51183) according to manufacturer's instructions.

Note: We slightly modified this protocol for increased yield. For the DNA precipitation step, increase the spin time if centrifuging at a slower speed to fully precipitate DNA. Elute with Qiagen Buffer EB (10 mM Tris-Cl, pH 8.5; Cat # 19086) instead of Buffer AE. Spin at 4,500 × g for 5 min. Elute 2–3 times with new Buffer EB each time (do not reload eluate).

16. Measure the gDNA concentration by nanodrop. We typically obtain 100 µg gDNA per 20 × 10^6 cells.

Note: Although measuring DNA by Qubit dsDNA assay is more sensitive and accurate than by nanodrop, we noticed running PCRs based on the concentration of gDNA from the Qubit assay sometimes resulted in a poor amplifying efficiency. Therefore, we recommend using a nanodrop to measure DNA concentration.

17. Amplify the integrated sgRNA (PCR1) with the following reagents and reaction program:

CRITICAL: To make sure the diversity and coverage of sgRNAs is not lost during PCR1, multiple 100 µL PCR reactions are required for screen preparation. Empirically, we recommend 1 PCR reaction for every 2,500 sgRNA in the library (e.g., For a customized library that has 25,000 sgRNAs, at least 10 PCR reactions are needed, and therefore a minimum of 100 µg gDNA is required).

Note: Although this protocol calls for 10 µg of genomic DNA per 100 µL PCR1 reaction, DNA input can be decreased to 5 µg or less if necessary. See *Troubleshooting* section for a brief explanation on why a user may want to decrease the input genomic DNA.

Note: As the amount of genomic DNA collected from cell samples can be limited, especially for FACS-based screens, it is highly recommended to run a single (or "pilot") PCR1 to ensure all conditions are correct and yield an amplified fragment.

18. Pool and mix all amplicons of the PCRs from the same gDNA sample. Add Illumina sequencing indexes with the following reagents and reaction program:

PCR1 reaction master mix

Reagent	Volume (µL)
gDNA template (10 µg)	x
Herculase II polymerase	2
oMCB_1562 (100 µM)	1

oMCB_1563 (100 μM)	1
5× Herculase buffer	20
dNTPs (100 nM)∗	1
ddH_2O	75-x

∗25 nM per dNTP.

PCR1 cycling conditions

Steps	Temperature	Time	Cycles
Initial Denaturation	98°C	2 min	1
Denaturation	98°C	30 s	18 cycles
Annealing	59.1°C	30 s	
Extension	72°C	45 s	
Final extension	72°C	3 min	1
Hold	4°C	∞	

PCR2 reaction master mix

Reagent	Amount (μL)
PCR1 product	5
Herculase II polymerase	2
oMCB_1440 (100 μM)	0.8
oMCB_1439 (100 μM)	0.8
5× Herculase buffer	20
dNTPs (100 nM)	2
ddH_2O	69.4

PCR2 cycling conditions

Steps	Temperature	Time	Cycles
Initial Denaturation	98°C	2 min	1
Denaturation	98°C	30 s	20 cycles
Annealing	59.1°C	30 s	
Extension	72°C	45 s	
Final extension	72°C	3 min	1
Hold	4°C	∞	

Note: Though PCR1 uses 18 cycles, it was empirically determined that 20 cycles for PCR2 resulted in the best signal-to-noise ratio.

Note: Selecting index adapters with diverse sequences for pooled libraries is CRITICAL: for successful sequencing and data analysis. For information on how to optimize the color balance of the index adapters see the “Index Adapters Pooling Guide” published by Illumina.

Note: Only one 100 μL PCR2 reaction is sufficient to achieve sequencing depth.

19. Load PCR products onto 2% TBE-agarose gel.
20. Run the sample at 120 V for 50 min. Excise the brightest band.

Note: The size of the band is expected to be 280 bp but may run higher due to overloading of the gel.

21. Purify DNA products using QiaQuick Gel Extraction Kit (Cat # 28706) according to manufacturer's instructions.

Note: We slightly modified this protocol for increased yield. When dissolving the gel, add 4 volumes Buffer QG instead of 3. For the DNA precipitation step, add 3 M sodium acetate pH 5.2 at a 1:100 ratio. For the wash step, wash with Buffer PE two times instead of once. Elute DNA in Buffer EB, not water.

22. Check DNA concentration by Qubit dsDNA HS Assay. We typically obtain 30 ng/mL DNA.
23. Verify DNA quality using a fragment analyzer. DNA fragments should run as a single band at ~300 bp (Figure 4-7B).
24. If the DNA runs as a single band at ~300 bp without contamination at other sizes, pool equal amounts of DNA from each screen sample so that the final concentration is 3 nM. Send the pooled library for deep sequencing.

Note: The molecular weight of the DNA can be calculated based on the nucleotide sequence.

a. We typically send 50 µL of the pooled library at 3 nM and 30 µL of the Bassik custom sequencing Illumina sequencing primer (oMCB1672_new10gCRKO) at 100 µM. Both are sent in Qiagen EB (10 mM Tris, pH 8.5).

CRITICAL: The pooled library loses diversity after ~26 bp. For the sequencing read, 22–25 cycles single end read is recommended. Alternatively, request the sequencing facility to add 20%–30% PhiX to increase the diversity.

Note: A minimum of 200× coverage is required when choosing a sequencing platform. For example, if a sgRNA library contains 30,000 elements, a pooled DNA library from 2 cell samples and 20% PhiX requires $30{,}000 \times 200 \times 2 \times (100\% + 20\%) = 14.4 \times 10^6$ single-end read. A standard MiSeq v3 has up to 25×10^6 reads, which is enough to sequence this library.

Note: We recommend requesting the sequencing data in the demultiplexed FASTQ format, as demultiplexing separates each barcoded sample reads into individual files.

4.3.4 Analysis of deep sequencing data using casTLE

Timing: 2–5 days, not including any additional time needed by the facility performing the sequencing

Analysis of deep sequencing reads can be performed using a number of statistical frameworks, all of which involve sequence read alignment and gene enrichment calculations to identify hit genes that influence the phenotype of interest. Commonly used pipelines include MAGeCK[201,202], MAGeCK-iNC[203], HiTSelect[204], DeSEQ[205], and RIGER[206]. Here we describe the analysis pipeline for cas9 high-Throughput maximum Likelihood Estimator (casTLE[207]). The casTLE package consists of custom scripts for sequence read alignment using Bowtie, hit gene identification, and quality control and data visualization. CasTLE is built upon an empirical Bayseian framework that combines measurements from multiple targeting reagents (e.g., multiple sgRNAs per gene) to estimate a maximum effect (phenotype) size and an associated p-value by comparing each set of gene-targeting guides to the negative controls. For each gene, casTLE calculates enrichment (casTLE effect) as a median normalized log ratio of counts, with an associated confidence score (casTLE score), which is twice the log-likelihood ratio of the effect. CasTLE can analyze two replicate screens side-by-side, and a combination gene score and effect can then be calculated for each gene. CasTLE also contains plotting scripts, which allow the user to visualize the results as a volcano plot (*see step 31*), plot the distribution of targeting guides relative to negative controls (*see step 36*), graph and calculate guide representation (*see step 30*), and assess reproducibility between samples (*see step 35*).

25. Download and back up raw sequencing FASTQ files.

Note: Many NGS core facilities delete the FASTQ files after a few weeks, so download and back them up shortly after receiving them.

Note: Raw FASTQ files must be unzipped to be opened in a text editor. It is usually unnecessary to view them unless a potential quality issue is detected as the files are large and time consuming to download.

Note: FASTQC can be used for a quality control assessment of FASTQ files (e.g. identification of irregularities, such as overrepresented sequences).

26. Install casTLE version 1.0 and the required modules. We recommend running casTLE on Linux or MacOS.

Note: casTLE scripts were written for python 2.7 and Bowtie version 1. Scripts will need to be updated to run on python 3 or higher.

Note: Install the parallel python module to increase speed of the casTLE analysis (optional but recommended).

Note: Alternatively, casTLE analysis workflow can be run on the new, web-based platform LatchBio (https://latch.bio/).

27. Open Terminal and navigate to the folder containing the casTLE scripts. CasTLE scripts are run from the command line.

Note: All casTLE scripts should be run from the top folder.

28. For screens conducted using sgRNA libraries other than the Bassik Human or Mouse CRISPR Knockout Library (Addgene # 101926-34, # 1000000121-30), create a bowtie index using the casTLE script makeIndices.py.

Note: If using the Bassik Human or Mouse CRISPR Knockout Library, skip this step and proceed to step 29.

```
python Scripts/makeIndices.py <list sequence file> <screen type> <screen type index>
```

List sequence file	The comma-delimited reference library file containing two columns: Element name, element sequence
Screen type	User-chosen name for the screen type (will need this name for the alignment script in step 29)
Screen type index	User-chosen name for the output bowtie index files (.ebwt) in the “Indices” folder

Note: In the event of the error bowtie-build: not found rerun the script with -b <bowtie-build location> at the end of the command. The error indicates that bowtie-build (the bowtie script required for casTLE’s makeIndices.py script) cannot be located, and -b will indicate the location.

29. Align FASTQ sequences to the reference sgRNA library using the casTLE script makeCounts.py.

```
python Scripts/makeCounts.py <file base for FASTQ file> <output file name> <screen type>
```

File base for FASTQ filePath to the raw FASTQ file (can be fastq or the zipped fastq.gz). Output file nameUser-chosen name of the output count file and corresponding record fileScreen typeThe name of the screen type. If using Bassik libraries, the screen type is Cas9-10 (human) or mm-Cas9-10 (mouse). If using a different library, the screen type was named in step 28.

Note: To change the length of the sequencing read to be aligned, include the conditional argument -r [number] in which the number indicates how many base pairs should be used in the alignment. CasTLE’s default read length is 17 base pairs.

Note: If using a library other than the Bassik human or mouse library, the naming scheme for control sgRNAs (as used in the list sequence file) must be indicated. At the end of the argument, include -n [prefix of negative control sgRNAs].

30. Visualize the distribution of elements in each count file using the casTLE script plotDist.py (Fig 4-6A). The output is a .png file containing a plot of elements (x-axis) versus frequency (y-axis).

```
python Scripts/plotDist.py <output file name> <count file >
```

Output file name	User-chosen name of the output file
Count file	Path to the .csv count file generated in step 29

To visualize element distributions from more than one count file (e.g., three counts files), run the following script:

```
python Scripts/plotDist.py <output name> <count file 1> <count file 2> <count file 3> -l Sample1 Sample2 Sample3
```

Where -l indicates sample names to be included in the plot's legend, in order of count files in the command.

Note: If analyzing counts from a specific sublibrary within the Bassik library, indicate the sublibrary with -x [sublibrary]. For example, -x ACOC.

31. Compare sgRNA enrichment between two files (e.g., vehicle vs. treated or GFP high vs. GFP low) using the casTLE script analyzeCounts.py.

```
python Scripts/analyzeCounts.py <count file 1> <count file 2> <output results file>
```

Count file 1	Path to the counts file for sample 1 (e.g., untreated or vehicle treated for death-based screen, low fluorescence population for FACS-based screen)
Count file 2	Path to the counts file for sample 2 (e.g., drug treated for death-based screen, high fluorescence population for FACS-based screen)
Output results file	User-chosen name of the output results file and corresponding record file

The output is a .csv file (and an associated record file) containing 13 columns:

Column	Heading	Description
A	GeneID	Ensembl ID
B	Gene symbol	Gene name
C	GeneInfo	Identifier
D	Localization	GO term
E	Process	GO term
F	Function	GO term

G	Element #	Number of sgRNAs targeting that gene detected
H	casTLE effect	Most likely effect size
I	casTLE score	Confidence in the casTLE effect
J	casTLE p-value	Estimated p-value from the casTLE score. This column will read N/A until the addPermutations.py script is run (step 32)
K	Minimum effect estimate	95% credible interval for the casTLE effect size estimate
L	Maximum effect estimate	95% credible interval for the casTLE effect size estimate
M	Individual elements	Individual element (sgRNA) enrichments. Formatted as <enrichment value> : <element ID>

Note: By default, casTLE removes sgRNAs with fewer than 10 sgRNA counts from the analysis. To change the threshold for removal, include -t [number] at the end of the argument. For example, -t 50 will tell casTLE to remove genes with fewer than 50 counts from the analysis.

Note: The casTLE script plotVolcano.py can be used to quickly visualize the casTLE effect (x-axis) versus casTLE score (y-axis). We recommend generating volcano plots in a program such as GraphPad Prism for publication quality figures (Figure 4-6B).

32. Estimate p-values using the casTLE script addPerm.py and calculate false discovery rate (FDR).

```
python Scripts/addPermutations.py <results file> <number of permutations>
```

Results file	Path to the results file generated in step 31
Number of permutations	User-chosen number of permutations

Note: For publication, we recommend that the number of permutations run is 50× the number of genes in the library. For example, run 150,000 permutations for a library that contains 3,000 genes.

   a. To calculate 10% FDR, sort genes from lowest to highest p-value and use the following equation: =IF([p-value]<0.1×(ROW()-1)/[total # of genes],1,[subsequent row]).

33. Compare screens using the casTLE script analyzeCombo.py. The output file will contain a new, combined casTLE effect and casTLE score for each gene.

```
python Scripts/analyzeCombo.py <results file 1> <results file 2> <output file name>
```

Results file 1	Path to the results file for replicate 1
Results file 2	Path to the results file for replicate 2
Output file name	User-chosen name of the output results file and corresponding record file

34. Estimate p-values for the combined casTLE results using the casTLE script addCombo.py. Calculate false discovery rate (FDR) as described in step 32.

```
python Scripts/addCombo.py <combo results file> <number of permutations>
```

35. Compare casTLE effects and casTLE scores between replicates using the casTLE script plotRep.py (Fig 4-6C-D**)**. The output is two scatter plots (PNG files) with the coefficient of determination (R^2).

```
python Scripts/plotRep.py <results file 1> <results file 2> <output file name>
```

36. Visualize distribution of sgRNAs for genes of interest versus null distribution using the casTLE script plotGenes.py (Figure 4-6E-G).

```
python Scripts/plotGenes.py <results file 1> <gene name 1> <gene name 2>…
```

Note: The output is a cloud plot and a histogram. The cloud plot (top panels) is a scatter plot showing the deep sequencing counts for each element targeting the gene of interest (color scale) along with all the negative sgRNAs (gray). The histogram (bottom panels) is a frequency distribution of the casTLE effect for negative controls (red) versus the gene of interest (blue). Vertical solid lines indicate the individual casTLE effects for each guide, and the vertical dashed line indicates the casTLE effect for that gene. Figures 6E-G shows examples of cloud plots and histograms for hypothetical enriched gene X (Figure 4-6E), depleted gene Y (Figure 4-6F), and unaffected gene Z (Figure 4-6G).

Note: This script also serves as a quality control step by plotting the distribution of negative control sgRNAs, in both the cloud plot and the histogram.

Note: To change the file type, add -f [file type] to the end of the command. For example, to generate SVG files instead of PNG files, the script should end with -f svg, and the output file will be a SVG file.

4.4 Expected Outcomes

If the PCR is successful, a clean, bright band at ~300 bp from PCR2 product should be visible on the 2% TBE-agarose gel. If amplicons from PCR1 are also loaded onto the agarose gel, it is not uncommon if only a very faint band or no band is seen.

For the fragment analysis, 3 peaks are expected, including a lower marker (LM) at 1 bp, an upper marker (UM) at 6,000 bp and a single peak at ~300 bp from the DNA sample (Figure 4-7B).

For successful sequencing, several files in “fastq.gz” and “fastq.gz.md5” format should be generated. The “fastq.gz.md5” file contains a string of numbers and letters called md5 hash, which are identifiers of the corresponding “fastq.gz” file. It is important to check the

md5 hash of each “fastq.gz” file and ensure they are identical to the record in “fastq.gz.md5” files. For a single-read run, one R1 fastq file will be created for each sample. In addition to all files associated with each sample, files named as “undetermined” could also be included. They contain sequences that have not been successfully demultiplexed on the barcode with sufficient accuracy. If PhiX is spiked in, they should also be in the “undetermined” files. Only “fastq.gz” files with the sample name are needed for the analysis.

A successful CRISPR screen should maintain high sgRNA diversity (>0.9), calculated in step 35. If diversity is lower, proceed to the troubleshooting section. CasTLE effects are standardly between 0 and 8 and casTLE scores between 0 and 500. A false discovery rate (FDR) based on casTLE effect or score can be calculated to determine “hit” genes (see step 32). The FDR cutoff will depend on the biological question, whether identifying larger compendiums of moderate- to high-confidence hits or a select few of the highest confidence hits. We use a 10% FDR for the former and a 1% or 5% FDR for the latter.

After identifying hit genes, single gene KOs should be generated to validate effects seen in the CRISPR screen. At least two independent sgRNAs should be used to mitigate false positives. The most effective sgRNAs to use for follow-up studies can be identified from the results files and counts file as well as the cloud and histogram plots made by the plotGenes script (see step 36). In a successful CRISPR screen, single KOs should replicate the effects determined by bioinformatic analysis (see troubleshooting for an explanation on why strong, real hits may not validate as individual KOs).

To further compare results and determine biological significance, data should be uploaded onto a CRISPR screen repository such as BioGRID CRISPR repository, CRISPRbrain, or CRISPRlipid.

4.5 Limitations

Compared to arrayed CRISPR/Cas9 screens, which analyze genetic perturbations independently and can therefore be paired with imaging or metabolomics profiling[208], pooled screens give limited insight into how individual perturbations affect cellular phenotypes besides the one in question. The generation of individual gene knockouts is necessary to validate and expand upon screen results. Although pooled screens are less labor-intensive than arrayed screens, they still require at least one month of cell culture, which incurs a high cost, made higher by using adherent cells and growing them at high coverage. Depending on the question of interest, using suspension cells can lower the time and cost of a genetic screen. And, although proficiency in Python is not necessary for running casTLE commands, a basic understanding of coding is useful for performing bioinformatic analysis. Analytical platforms like LatchBio negate the need for coding experience and make analysis more accessible to researchers of different backgrounds.

False positive and false negative “hits” are possible and must be mitigated at every step of the screening process. False positives can occur when sgRNAs bind off-target sites or

gene expansion causes Cas9 to cleave many times, leading to upregulation of the DNA damage response[209]. False negatives can occur when coverage is low or lost (Figure 4-7C-E**)**, or compensation occurs genetically or arises during the screening process[210,211]. It is therefore necessary to maintain cells at high (1000×) coverage and to grow and passage cell samples for the same length of time to prevent genetic compensation. Performing multiple replicates and using the combination analysis function of casTLE also addresses the problem of false negatives[207].

4.6 Troubleshooting

4.6.1 Problem: Low titer of lentivirus packaged sgRNA library

Potential solution

- Poor DNA quality: Check that the pooled library is pure (260/280 and 260/230 values).
- Issues with HEK293T cells: Cells should be low passage and seeded at the optimal confluence for transfection. Check the viability of HEK cells prior to seeding and aim for over 95% viability.
- Issues with transfection reagents: Double-check that reagents are not expired and/or have precipitated.
- Packaging vector issues: Ensure that the correct packaging vectors are being used (e.g., 2nd versus 3rd generation).
- Filtering through wrong pore size: Virus-containing media should be filtered through a 0.45 µm mesh, not 0.20 µm.
- Insufficient viral production: include a positive control, such as plasmid that has been packaged successfully in the lab.
- If viral titer is still low, concentrate virus using a reagent such as PEG-it Virus Precipitation Solution (System Biosciences # LV810A-1).

4.6.2 Problem: Inefficient PCR or no PCR product

Potential solution

- Ethanol carryover from the genomic DNA extraction can inhibit downstream PCR reactions. Prior to eluting gDNA, incubate columns at 70°C for 10 min to evaporate residual ethanol.
- Decrease the gDNA input to ~5 µg per PCR1 reaction (step 22). Use nanodrop concentrations of purified gDNA instead of Qubit concentrations.
- If samples were successfully amplified but with low efficiency (Figure 4-7A, lane G), increase the number of PCR1 cycles to 19–20 cycles.

4.6.3 Problem: Low percentage of successfully mapped reads

Potential solution

Open the FASTQ from the NGS facility in a text editor and look at the sequences to better understand the problem. NGS sequences may need to be trimmed during the read mapping step (casTLE makeCounts.py command).

4.6.4 Problem: Low library diversity or loss of element representation

Potential solution

Low library diversity often results from (1) problems with the sgRNA library, (2) bottlenecks during the screening process, or (3) issues with deep sequencing preparation.

- The sgRNA library should always be sequenced before the first use to ensure that roughly 90% of guides are present and evenly distributed. If the library is missing more than 10% of elements, it should be re-amplified.
- Bottlenecks can occur during lentiviral packaging of sgRNA library, infection, and passaging.
    - Ensure that library representation will be maintained by transfecting the necessary number of HEK293T cells with enough library DNA.
    - Perform quality control (see steps 27 and 28) on NGS sequences from the initially library-infected cell population to determine whether the bottleneck occurred prior to phenotypic selection.
    - Cells should always be passaged at ≥ 1000× coverage.
- A common limiting step in deep sequencing preparation is the gDNA extraction. When planning the screen, the user should ensure that enough cells can be collected to harvest enough gDNA. We typically collect 1000× cells (1000× number of gRNAs). For example, in a FACS-based screen of a 30,000 sgRNA library, at least 30×10^6 cells should be collected (total).

4.6.5 Problem: Hit genes determined by casTLE are not replicating effects in individual knockout cell lines

Potential solution

Some strong hits are difficult to validate as single knockouts, due to cell non-autonomous effects, viability issues when cultured with other non-KOs, or other influences on the phenotype due to culture conditions that make it difficult to compare to non-targeting controls in separate wells.

- Prior to generating individual knockout cell lines, perform a secondary pooled screen (also known as a batch retest screen) of a custom sgRNA library consisting of significant hit genes and control sgRNAs.
- Culture individual KO cell lines together with non-targeting cells, using different fluorescent markers.

4.7 Materials

REAGENT or RESOURCE	SOURCE	IDENTIFIER
Antibodies		
Cas9 (1:1000)	Abcam	Cat. # ab191468
Bacterial and virus strains		
5-Alpha competent *E. coli* (high efficiency)	NEB	Cat. # C2987H
One Shot™ Stbl3™ Chemically Competent E. coli	Invitrogen	Cat. # C737303
Endura™ ElectroCompetent Cells	Lucigen	Cat. # 60242-2
Chemicals, peptides, and recombinant proteins		
Dulbecco's modified Eagle's medium (DMEM)	Corning	Cat. # 10-017-CV
Phenol-red-free DMEM	Cytiva	Cat. # SH30284.01
PBS, 1× (w/o Ca2+, Mg2+)	Corning	Cat. # 21-040-CV
Fetal bovine serum (FBS)	Gemini Bio	Cat. # 100-500
Bovine serum albumin (BSA)	Sigma-Aldrich	Cat. # A1595
Absolute ethanol (200 proof)	Fisher Bioreagents	Cat. # BP-2818-500
RNase Away	Molecular Bioproducts	Cat. # 21-236-21
ELIMINase	Decon Labs	Cat. # 1101
Puromycin dihydrochloride	Thermo Fisher Scientific	Cat. # A1113803
Blasticidin S HCl	Thermo Fisher Scientific	Cat. # A1113903
O'GeneRuler (100 bp DNA ladder, ready-to-use)	Thermo Fisher Scientific	Cat. # SM1143
6× loading dye	Thermo Fisher Scientific	Cat. # R0611
UltraPure 10× TBE Buffer	Thermo Fisher Scientific	Cat. # 15581-044

Gibco™ Trypsin-EDTA (0.05%), phenol red	Thermo Fisher Scientific	Cat. # 25300062
Gibco™ TrypLE™ Express Enzyme (1×)	Thermo Fisher Scientific	Cat. # 12605010
SYTOX™ Green Dead Cell Stain	Thermo Fisher Scientific	Cat. # 34860
UltraPure Agarose	Thermo Fisher Scientific	Cat. # 16500100
Penicillin-Streptomycin (10,000 U/mL)	Thermo Fisher Scientific	Cat. # 15140122
Qiagen Protease (7.5 AU)	Qiagen	Cat. # 19155
Nuclease-Free Water	Qiagen	Cat. # 129117
Bovine serum albumin (fatty acid free, low endotoxin)	Sigma-Aldrich	Cat. # A8806
Hexadimethrine bromide	Sigma-Aldrich	Cat. # 107689-10G
(1S,3R)-RSL3	Cayman Chemical	Cat. # 19288
Ethylenediaminetetraaceti c acid (EDTA)	Fisher Scientific	Cat # 15575-020
*Trans*IT-LT1 transfection reagent	Mirus	Cat. # MIR 2300
BstXI	New England Biolabs	Cat. # R0113S
BlpI	New England Biolabs	Cat. # R0585S
T4 DNA Ligase	New England Biolabs	Cat. # M0202S
Critical commercial assays		
Herculase II Fusion Enzyme with dNTP Combo (400 rxn)	Agilent	Cat. # 600679
Qiagen QiaAmp DNA Blood Maxi Kit	Qiagen	Cat. # 51194
QIAquick Gel Extraction Kit	Qiagen	Cat. # 28706
HiSpeed Plasmid Kits	Qiagen	Cat. # 12663
Qubit dsDNA HS Assay Kits	Thermo Fisher Scientific	Cat. # 32851

Deposited data		
U2-OS CRISPR Screen Result	Li et al.[2]	CRISPRlipid, http://crisprlipid.org
MDA-MB-453 CRISPR Screen Result	Li et al.[2]	CRISPRlipid, http://crisprlipid.org
Experimental models: Cell lines		
Huh7	Kind gift from Dr. Holly Ramage (University of Pennsylvania)	N/A
U-2 OS Tet-On	Clontech	Cat. # 630919
HEK293T	UC Berkeley Cell Culture Facility	N/A
Oligonucleotides		
sgCherry	Self-cleaving mCherry	GGCCACGAGTTCGAGATCGA
sgSAFE_5784	Safe-targeting guide	AAATTTCATGGGAAAATAG
oMCB1562	PCR-1 Forward	aggcttggatttctataacttcgtatagcatacattatac
oMCB1563	PCR-1 Reverse	ACAtgcatggcggtaatacggttatc
oMCB1439	PCR-2 Forward	caagcagaagacggcatacgagatgcacaaaaggaaactcaccct
oMCB1440-AD002	PCR-2 Reverse with Barcode	aatgatacggcgaccaccgagatctacacGATCGGAAGAGCACACGTCTGAACTCCAGTCACCGATGTCGACTCGGTGCCACTTTTTC
oMCB1440-AD003	PCR-2 Reverse with Barcode	aatgatacggcgaccaccgagatctacacGATCGGAAGAGCACACGTCTGAACTCCAGTCACTTAGGCCGACTCGGTGCCACTTTTTC
oMCB1440-AD004	PCR-2 Reverse with Barcode	aatgatacggcgaccaccgagatctacacGATCGGAAGAGCACACGTCTGAACTCCAGTCACTGACCACGACTCGGTGCCACTTTTTC
oMCB1440-AD005	PCR-2 Reverse with Barcode	aatgatacggcgaccaccgagatctacacGATCGGAAGAGCACACGTCTGAACTCCAGTCACACAGTGCGACTCGGTGCCACTTTTTC

oMCB1440-AD006	PCR-2 Reverse with Barcode	aatgatacggcgaccaccgagatctacac GATCGGAAGAGCACACGTCTG AACTCCAGTCACGCCAATCGA CTCGGTGCCACTTTTTC
oMCB1440-AD007	PCR-2 Reverse with Barcode	aatgatacggcgaccaccgagatctacac GATCGGAAGAGCACACGTCTGA ACTCCAGTCACCAGATCCGACT CGGTGCCACTTTTTC
oMCB1440-AD009	PCR-2 Reverse with Barcode	aatgatacggcgaccaccgagatctacac GATCGGAAGAGCACACGTCTGA ACTCCAGTCACGATCAGCGACT CGGTGCCACTTTTTC
oMCB1440-AD010	PCR-2 Reverse with Barcode	aatgatacggcgaccaccgagatctacac GATCGGAAGAGCACACGTCTGA ACTCCAGTCACTAGCTTCGACT CGGTGCCACTTTTTC
oMCB1440-AD012	PCR-2 Reverse with Barcode	aatgatacggcgaccaccgagatctacac GATCGGAAGAGCACACGTCTGA ACTCCAGTCACCTTGTACGACT CGGTGCCACTTTTTC
oMCB1440-AD013	PCR-2 Reverse with Barcode	aatgatacggcgaccaccgagatctacac GATCGGAAGAGCACACGTCTG AACTCCAGTCACAGTCAACGA CTCGGTGCCACTTTTTC
oMCB1440-AD014	PCR-2 Reverse with Barcode	aatgatacggcgaccaccgagatctacac GATCGGAAGAGCACACGTCTG AACTCCAGTCACAGTTCCCGAC TCGGTGCCACTTTTTC
oMCB1440-AD015	PCR-2 Reverse with Barcode	aatgatacggcgaccaccgagatctacac GATCGGAAGAGCACACGTCTG AACTCCAGTCACATGTCACGA CTCGGTGCCACTTTTTC
oMCB1440-AD016	PCR-2 Reverse with Barcode	aatgatacggcgaccaccgagatctacac GATCGGAAGAGCACACGTCTG AACTCCAGTCACCCGTCCCGA CTCGGTGCCACTTTTTC
oMCB1440-AD018	PCR-2 Reverse with Barcode	aatgatacggcgaccaccgagatctacac GATCGGAAGAGCACACGTCTG AACTCCAGTCACGTCCGCCGA CTCGGTGCCACTTTTTC
oMCB1440-AD019	PCR-2 Reverse with Barcode	aatgatacggcgaccaccgagatctacac GATCGGAAGAGCACACGTCTG AACTCCAGTCACGTGAAACGA CTCGGTGCCACTTTTTC

oMCB1440-AD021	PCR-2 Reverse with Barcode	aatgatacggcgaccaccgagatctacac GATCGGAAGAGCACACGTCTG AACTCCAGTCACGTTTCGCGA CTCGGTGCCACTTTTTC
oMCB1440-AD022	PCR-2 Reverse with Barcode	aatgatacggcgaccaccgagatctacac GATCGGAAGAGCACACGTCTG AACTCCAGTCACCGTACGCGA CTCGGTGCCACTTTTTC
oMCB1440-AD025	PCR-2 Reverse with Barcode	aatgatacggcgaccaccgagatctacac GATCGGAAGAGCACACGTCTG AACTCCAGTCACACTGATCGAC TCGGTGCCACTTTTTC
oMCB1672_new10gCRKO	Illumina Sequencing Primer	GCCACTTTTTCAAGTTGATAACG GACTAGCCTTATTTAAACTTGCT ATGCTGTTTCCAGCTTAGCTCTTAAAC
Recombinant DNA		
lentiCas9-Blast	Addgene	Cat. # 52962
Bassik Human CRISPR Knockout Library	Addgene	Cat. # 101926, # 101927, # 101928, # 101929, # 101930, # 101931, # 101932, # 101933, # 101934
pMDLg/pRRE	Addgene	Cat. # 12251
pRSV-Rev	Addgene	Cat. # 12253
pMD2.G	Addgene	Cat. # 12259
pMCB320	Addgene	Cat. # 89359
Software and algorithms		
Image Lab v6.0.1	Bio-Rad Laboratories	https://www.bio-rad.com/en-us/product/image-lab-software?ID=KRE6P5E8Z
IncuCyte v2020A	Sartorius	https://www.sartorius.com/en/products/live-cell-imaging-analysis/live-cell-analysis-software
CasTLE statistical framework v1.0	Morgens et al.[8]	https://github.com/elifesciences-publications/dmorgens-castle
BowTie 2 v1.1.3.1	Langmead et al.[9]; Langmead and Salzberg[10]	https://bowtie-bio.sourceforge.net/index.shtml
FlowJo v10	BD Biosciences	https://www.flowjo.com/solutions/flowjo
Other		
245 mm square TC-treated culture dish	Corning	Cat. # 431110

96-well flat clear bottom black polystyrene TC-treated microplates	Corning	Cat. # 3904
0.45 μm filter	Thermo Fisher Scientific	Cat. # 158-0045

4.8 Figures

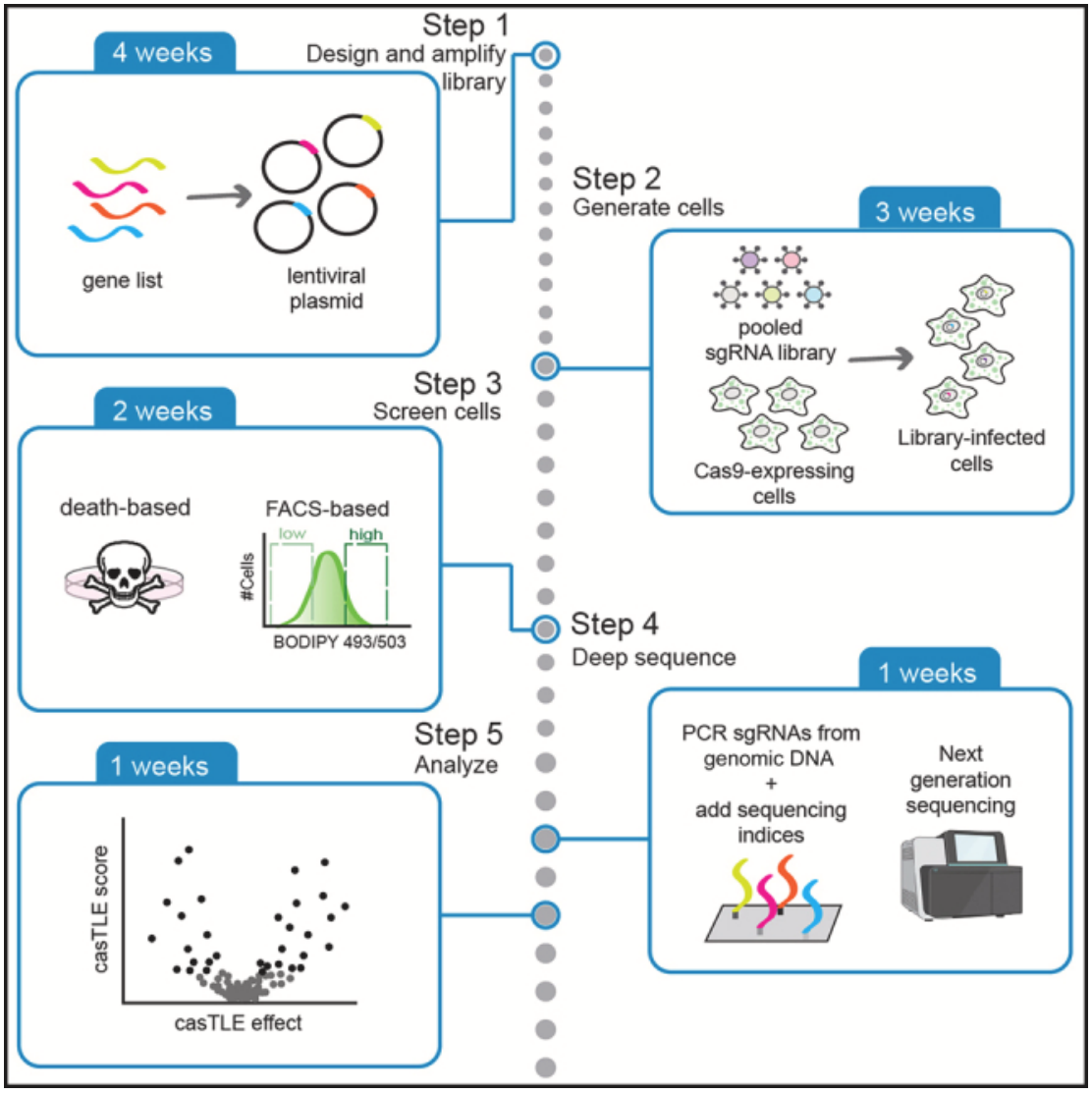

Figure 4-1. Graphical Abstract

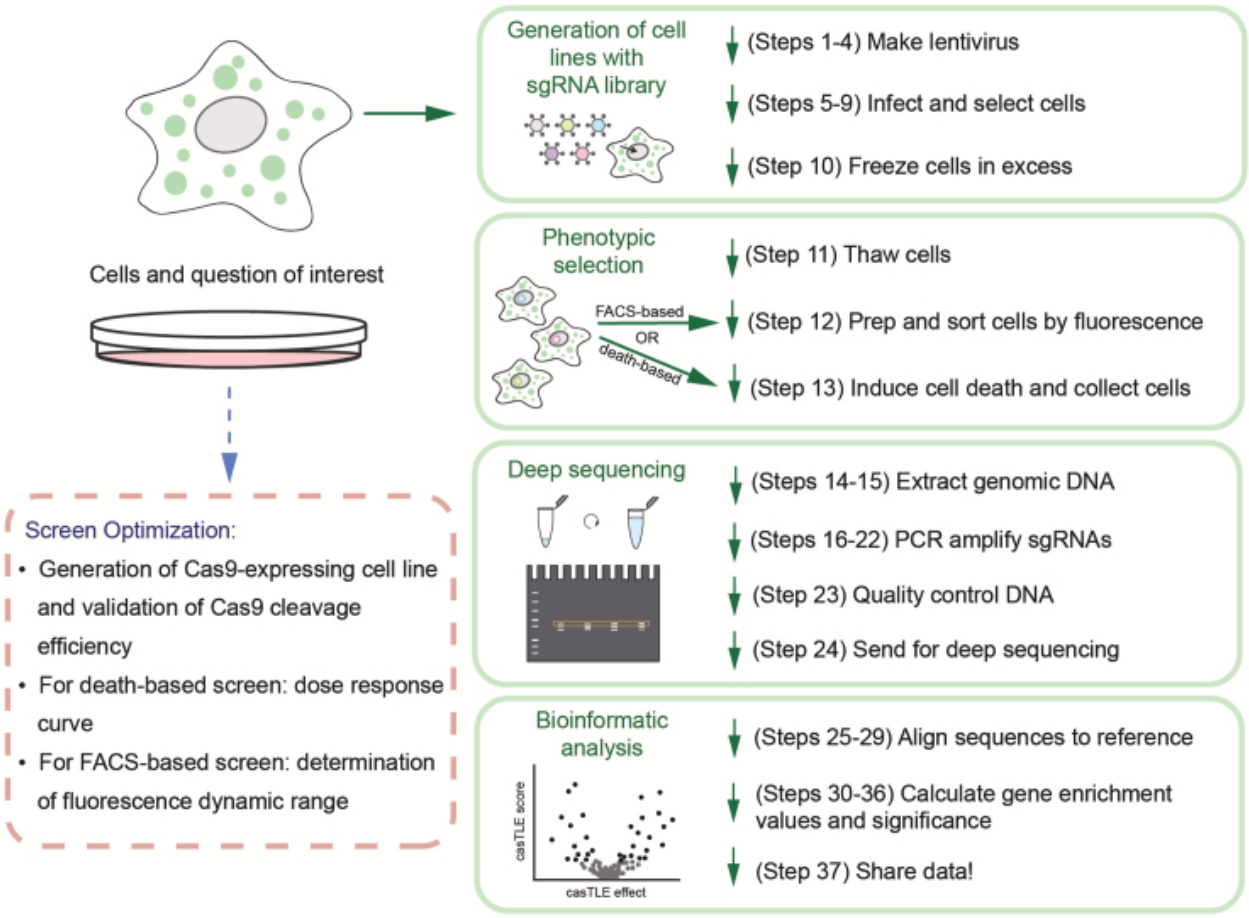

Figure 4-2. Schematic illustrating the major protocol steps for pooled CRISPR screens.

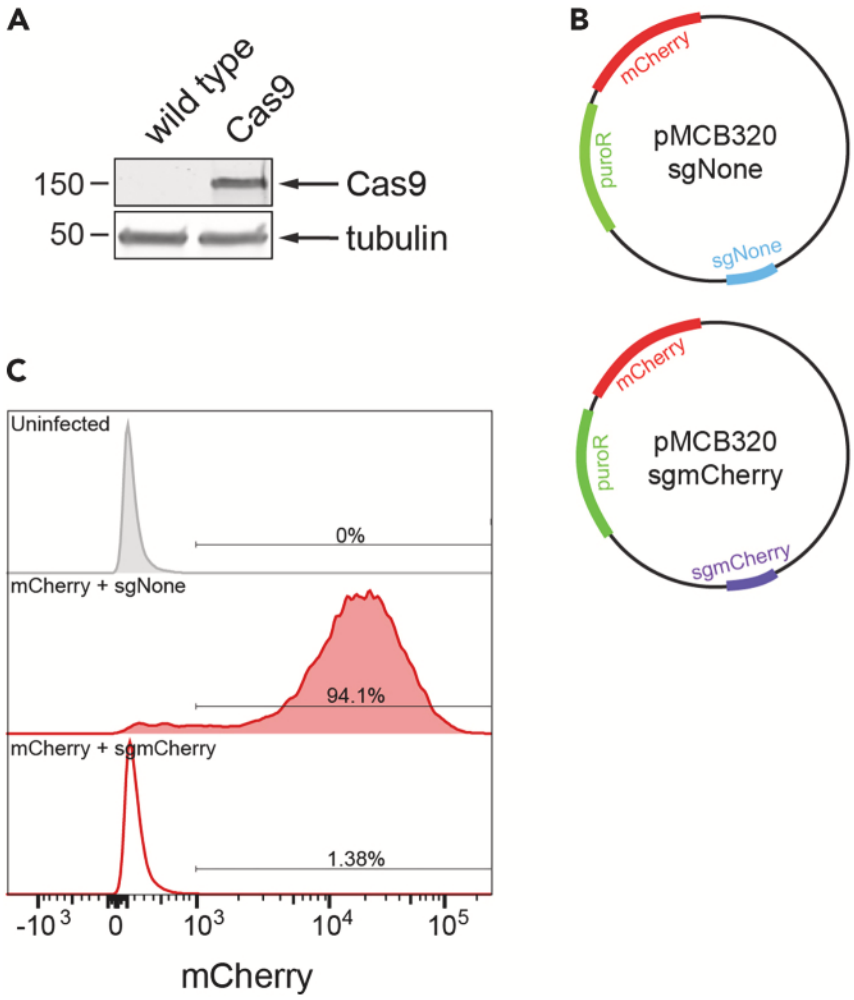

Figure 4-3. Generation of Cas9 stable-expressing cell line.
A) Representative western blot showing the expression of Cas9 in cells. B) Schematic of the mCherry self-cutting system to evaluate Cas9 activity. C) Example of analyzing Cas9 activity with the mCherry self-cutting system. Huh7 cells were infected with lentivirus expressing either sgmCherry or sgNone and selected by puromycin for one week. mCherry expression in cells was examined by flow cytometry.

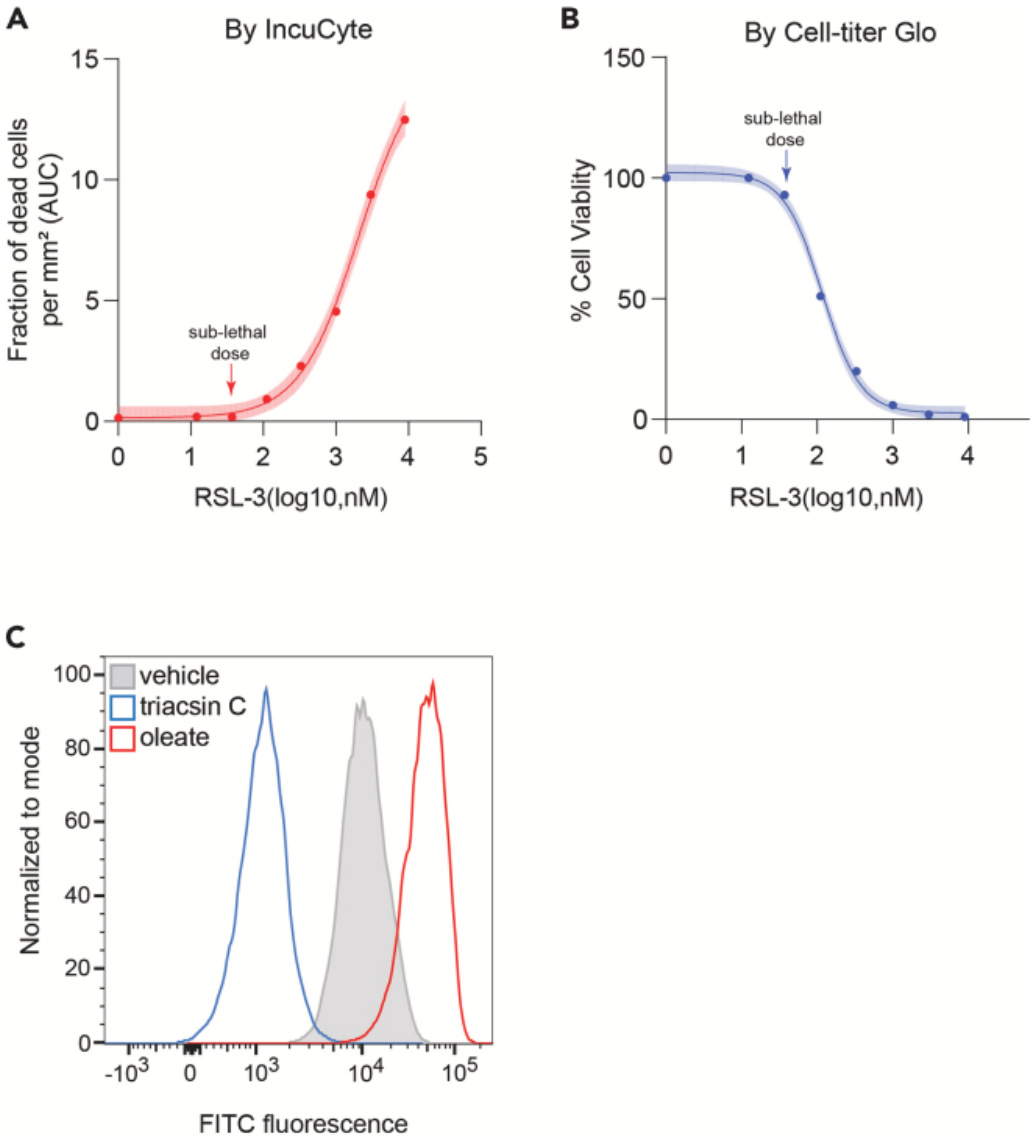

Figure 4-4. Determination of selection strategy for pooled CRISPR screens.
A and B) Characterization of sub-lethal dose of the desired compound for the treatment of cells by IncuCyte (A) or Cell-titer Glo 2.0 assay (B). Shading indicates 95% confidence intervals for the fitted curved and each data point is the average of three replicates. AUC, Area Under the Curve. C) Example of dynamic range of cell populations measured by flow cytometry strategy to optimize the dynamic range of a FACS-based screen.

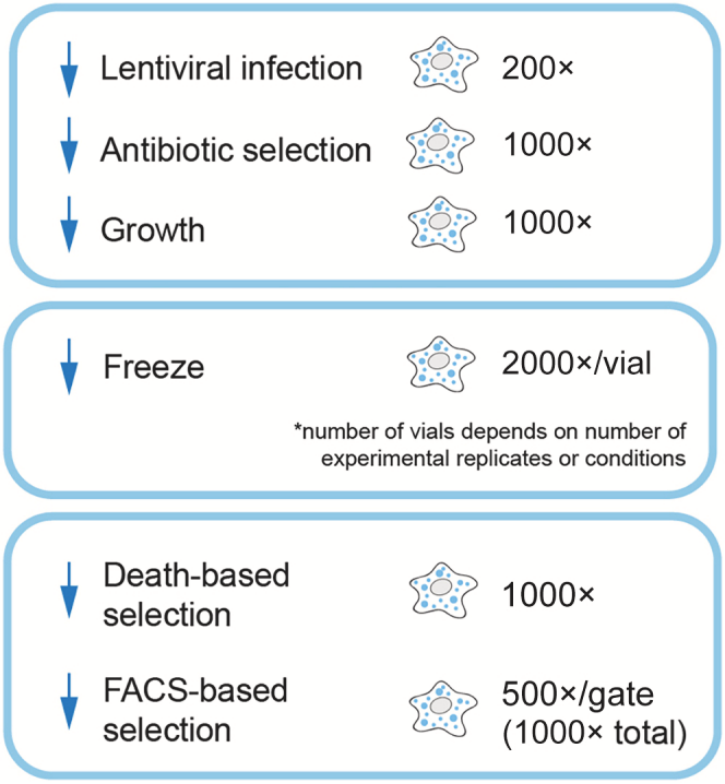

Figure 4-5. Schematic illustrating coverage maintenance at major steps of pooled CRISPR screens.

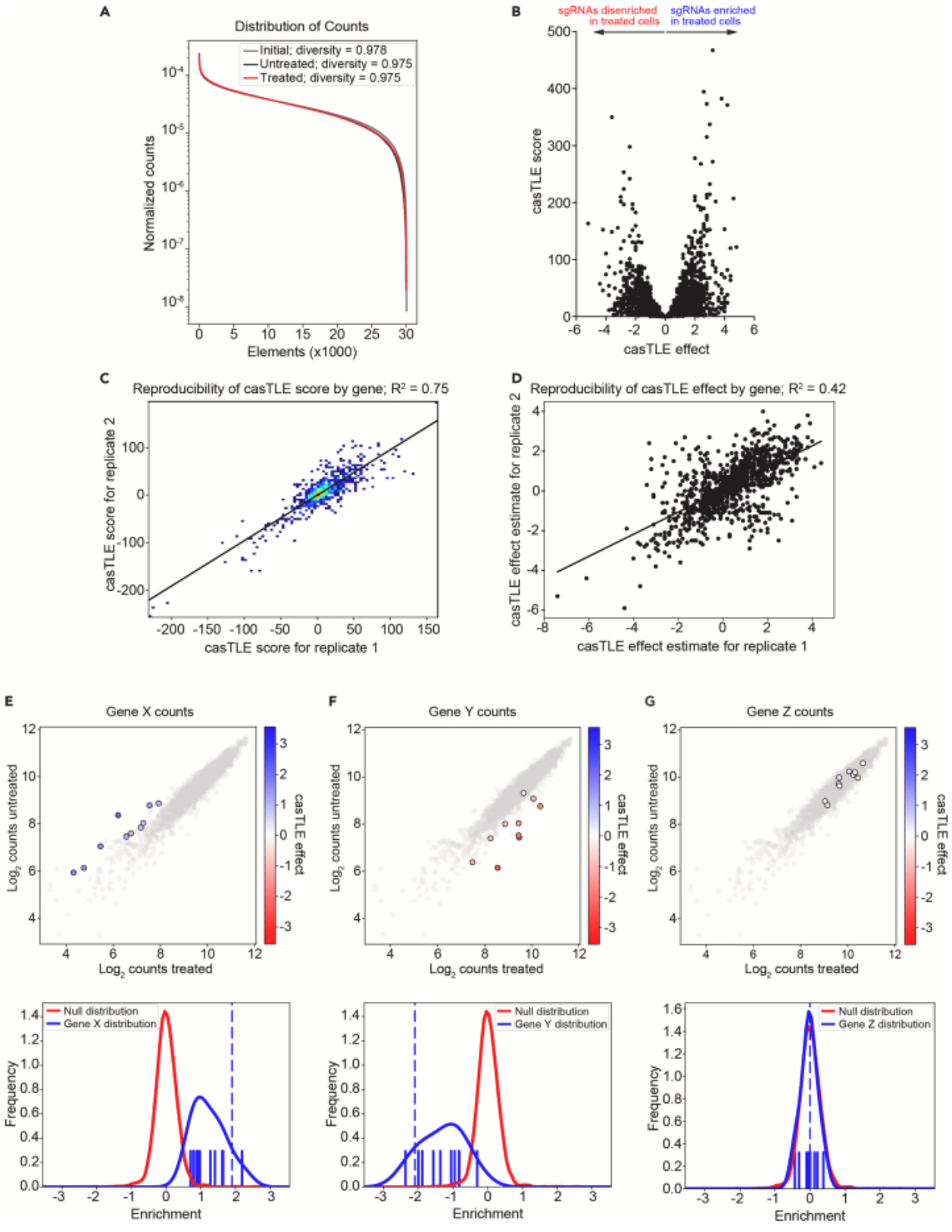
A
Distribution of Counts
Initial; diversity = 0.978
Untreated; diversity = 0.975
Treated; diversity = 0.975
Normalized counts
Elements (x1000)
B
sgRNAs disenriched in treated cells
sgRNAs enriched in treated cells
casTLE score
casTLE effect
C
Reproducibility of casTLE score by gene; R² = 0.75
casTLE score for replicate 2
casTLE score for replicate 1
D
Reproducibility of casTLE effect by gene; R² = 0.42
casTLE effect estimate for replicate 2
casTLE effect estimate for replicate 1
E
Gene X counts
F
Gene Y counts
G
Gene Z counts
Log2 counts untreated
Log2 counts treated
casTLE effect
Null distribution
Gene X distribution
Gene Y distribution
Gene Z distribution
Frequency
Enrichment

Figure 4-6. CasTLE analysis of deep sequencing data.
A) Example output from the casTLE plotDist.py script. Counts for each element were normalized to the total number of counts and diversity was calculated as normalized entropy using the total number of elements to define the max entropy. B) Example volcano plot of casTLE effects versus casTLE scores calculated using the casTLE analyzeCounts.py script. The plot was created in GraphPad Prism. C and D) Reproducibility plots of casTLE scores (C) and casTLE effects (D) generated using the casTLE plotRep.py script. E–G) Example cloud plots and histograms for a hypothetical CRISPR screen showing genes with multiple enriched sgRNAs (E), multiple disenriched sgRNAs (F), or sgRNAs that were neither enriched nor disenriched (G). Cloud plots (top panels) show individual element counts of negative sgRNAs (grey) and sgRNAs targeting the gene of interest (color). Histograms (bottom panels) plot the null distribution (negative sgRNAs; red) and the distribution of sgRNAs targeting the gene of interest (blue), with each solid vertical line indicating the casTLE effect of an individual sgRNA and the dashed vertical line denoting that gene's casTLE effect.

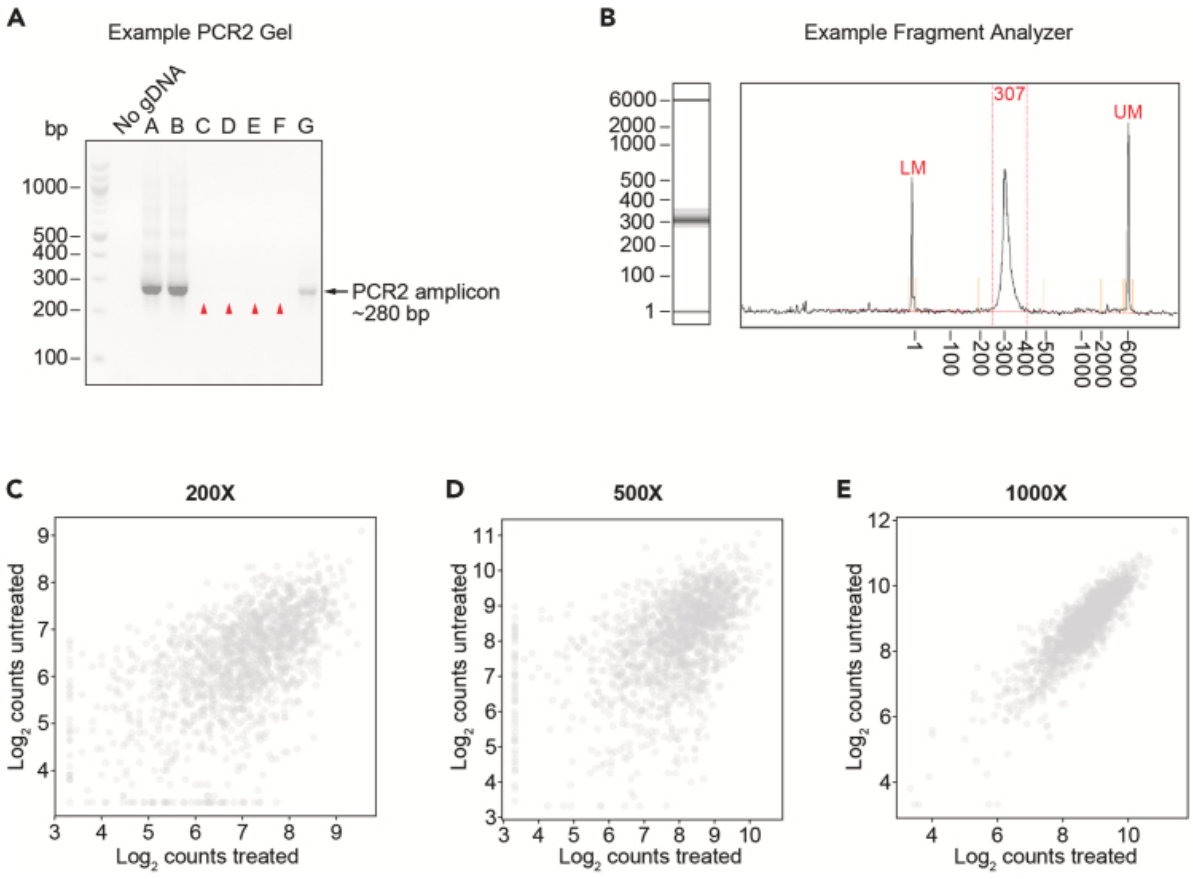

Figure 4-7. Troubleshooting DNA sequencing and analysis.
A) Example 2% agarose-TBE gel with a control lane (no gDNA control) and 7 samples (lanes A-G) following PCR2. Samples A and B were amplified as expected, with strong PCR2 amplicon bands at ~300 bp. Amplification of samples C–G was inefficient, as indicated by a weaker PCR2 band (sample G) or no PCR2 band (sample C-F; red arrows). B) Example DNA quality control of a single sample by fragment analyzer. The DNA sample is highlighted in red with a strong peak ~300 bp. Upper control marker (UM) and lower control marker (LM) bands are also highlighted. C–E) Negative control sgRNA cloud plots generated by the plotGenes script. The same library was sorted at 200× (C), 500× (D), and 1000× (E) coverage. As sgRNA representation increases, the distribution of negative control sgRNAs becomes tighter.

Chapter 5: Perspectives, Questions, and Conclusion

5.1 Perspectives and Questions

Identifying and characterizing new regulators of lipid storage will be hugely impactful for our understanding of cellular lipid homeostasis. Though hundreds of new avenues of research can hopefully arise from the functional genomic screens in Chapter 2, there are many more imminent questions to be explored related to the mechanisms of CLCC1 and IL32.

5.1.1 Defining different pools of neutral lipids

Recent structural and biochemical analyses of seipin have greatly elucidated the physical processes that govern lipid droplet emergence[21,23]. The large ring structure that can adopt multiple conformations is ideal for aggregating neutral lipids within a phospholipid bilayer and shunting them into the cytosol. Interestingly, even though hepatocytes generate large amounts of LDs, seipin is very lowly expressed in the liver[212], highlighting a lack of understanding of lipid flux in hepatocytes. Most research has pointed toward a bidirectional segregation of lipid flux on both sides of the hepatocyte ER—LDs toward the cytosol and lipoproteins toward the lumen—and both must be synthesized at the same time. The model proposed in Chapter 2 shifts this bidirectionality paradigm of lipid flux; lipid-rich precursor particles form in the ER first, and CLCC1 can "flip" a subpopulation into the cytosol while the rest mature into lipoproteins. Though this model answers the important question of why LDs are completely absent in $CLCC1^{KO}$ cells, it does raise more unknowns, specifically, how subpopulations of nascent particles would be distinguished, as well as the structure of CLCC1 and how it can facilitate membrane fusion and "flipping".

This model also indicates a larger need for better terminology surrounding lipid droplets and lipoproteins. Currently, lipoproteins are defined as apoB-containing, MTP-dependent particles generated in the ER lumen and destined for secretion, while lipid droplets are generated passively on the cytosolic-facing side of the ER lumen. However, lumenal lipid droplets can be generated basally or from ER stress[3], sometimes in an MTP-dependent manner[213]. CLCC1 depletion generates MTP-dependent, apoB-positive "lipoproteins" that are trapped within the ER lumen yet may not be deemed lipoproteins if they are never secreted. Concurrent literature has proposed calling these giant ER-enclosed lipid droplets (geLD)[214], which may be appropriate with such a large size—almost 10,000 times bigger than a canonical lipoprotein volumetrically. Yet perhaps the line between the two are blurred, and many nascent lipid particles can be synthesized and interchanged. Future research should employ proteomics and lipidomics to identify and delineate different types of lipid-rich particles in the ER lumen.

This concept applies even more broadly to the question of organelle heterogeneity in Chapter 3. Though distinct pools of ER—rough and smooth—have been delineated for almost a century, research is only currently appreciating the diversity and heterogeneity of other organelles, whether based on size, location, or proteome composition[215–217]. Most efforts to distinguish pools of LDs are focused LD size and localization[218–220]. However, little is known about LD protein heterogeneity besides differential recruitment of the perilipin proteins[220]. We propose a technique similar to lyso-IP[221] to isolate LDs, where GFP-tagged PLIN2 is precipitated on antibody beads, "pulling down" the LD with it. This

technique can be applied to isolate IL32-positive LDs and perform proteins and lipidomics; even more, it is broadly applicable to any protein of interest will be immensely useful for studying subpopulations of LDs. Yet even with this research, the reason as to *why* a cell would desire many types of LDs remains amorphous, indicating a rich and open future for lipid droplet innovation.

5.1.2 Exploring the mechanism of CLCC1

The identification of CLCC1 not only as a major regulator of lipid storage but also a long sought-after homolog of yeast nuclear membrane fusion components is integral for our understanding of organelle biology. There is a longstanding connection between nuclear pore biogenesis and hepatic lipid metabolism through the AAA ATPase torsinA and its cofactors Lull1 and Lap1, though the tie between the two has remained unknown[169,170,222]. CLCC1 has the first mechanism that bridges this gap, where membrane fusion is necessary for NPC biogenesis and LD emergence and growth. It is possible that torsinA recycles CLCC1, and depletion of torsinA would cause CLCC1 to become inactive. Yet it remains unknown if torsinA works in concert with CLCC1 or by a distinctive mechanism. Surprisingly, loss of are other regulators of nuclear membrane homeostasis can cause hepatic steatosis as well[223,224], highlighting the need for more research in this area.

One question that remains is how lipogenesis is upregulated in CLCC1^{KO} cells and liver. SREBP signaling is increased in TMEM41B^{KO} mice[33], accounting for the increase in liver fat even on a chow diet. However, SREBP signaling does not appear to be upregulated under CLCC1 depletion by RNA-Seq or Western blot (data not shown), even though TAG biogenesis is increased (Chapter 2, Figure 2-S4C). It is possible that defects in lipoprotein secretion and lipid sensing feed-back to increase lipid synthesis in an SREBP-independent manner, though how this is achieved is unknown. Another clue may come from the changes in the lipidome of CLCC1^{KO} livers. Preliminary data indicated an increase in PUFA-containing TAGs and PLs in CLCC1^{HepKO} mice (Chapter 2, Figure 2-S5), some of which cannot be generated *de novo* by mammalian cells. This may imply an increase in PUFA uptake or increase in desaturases, which could increase lipid storage, though again, this mechanism is unknown. Challenging mice with high fat or high PUFA diets could help in our understanding of how this happens.

Besides the liver, CLCC1 should be studied in the small intestine, the only other tissue that secretes apoB-containing lipoprotein particles. Since enterocytes do not usually utilize *de novo* lipogenesis to create fats, and they do not sense LDL the same way as the liver, it is possible that the phenotype in the intestine differs from that seen in hepatocytes. Additionally, while our data suggest that CLCC1 depletion does not cause lumenal lipid accumulation in other cell types, other research has shown that CLCC1 depletion manifests as ER stress and neurodegeneration[158,159]. Whether this is due to defects in membrane fusion and nuclear pore biogenesis is unknown, and whether more organs are involved in this pathology is unknown.

Finally, while CLCC1 is very highly conserved across higher eukaryotes, it is important to identify other homologs besides Brl1p / Brr6p in other species. For instance, there are no predicted structural homologs of Brl1p / Brr6p / CLCC1 in plants, though they must also

undergo membrane fusion to insert nuclear pores post-mitotically[225]. Perhaps other types of fusion machinery exist, or other mechanisms of NPC biogenesis will be identified in plants. Interestingly, one of the only known ring protein complexes that promotes membrane fusion is found in plant and algae thylakoid membranes[226], opening the possibility for more ring oligomers functioning membrane fusion across biological realms.

5.1.3 Therapeutic relevance

MASLD is a major global health problem, affecting around 25% of people worldwide with almost no promising therapeutics[227]. It is primarily a comorbidity of metabolic diseases like obesity and type II diabetes, though there are dozens of secondary causes of fatty liver such as alcohol, aging, starvation, hepatitis C infection, environmental toxicity, and genetics[228]. Most therapies for fatty liver are limited to dietary changes or antivirals, though our newfound understanding of lipid flux and directionality at the hepatocyte ER opens new avenues for treating metabolic-related fatty liver. Targeting CLCC1 itself has little therapeutic promise, as loss of it causes fatty liver and overexpression does not decrease lipid levels, and the non-cell autonomous roles could be too essential to be depleted, i.e. preventing nuclear pore formation. However, there is much work to be done finding interacting partners or downstream effectors of CLCC1 that could be targeted. Targeting IL32 is more favorable therapeutically, as its depletion decreases lipid storage, and it is only upregulated during inflammation, making off-targets in healthy patients less likely. Antibodies to IL32 could be promising to test clinically, and their viability would elucidate more of the mechanism of IL32 in the liver. Overall, as our understanding of lipid metabolism in the liver increases, our ability to prevent fatty liver or develop therapeutics coincidingly increases.

5.2 Conclusion

Lipid droplets were first discovered in the 1880s though were long considered inert globs of fat[229], not reaching bona fide membrane-bound organelle status for over a century. Much of the research on lipid droplets since their discovery has focused on their presence or absence in metabolic diseases like obesity and fatty liver disease. Advances in imaging techniques and *in silico* modeling have enhanced our understanding of the biogenesis and breakdown of LDs, yet the field still lacks a mechanistic grasp of when and where LDs are made, as well as the diversity of LDs—across species, across cell types, or within the same cell.

This work elucidates much of the complexity of LD biology. Chapter 1 gives an in-depth overview of our knowledge of lipid flux in and out of LDs: how lipids are synthesized and coalesced within a membrane, how they move into LDs and traverse to other organelles, how they protect against toxicity but provide resources in times of need. In Chapter 2, we used a functional genomics strategy to identify and characterize a novel regulator of lipid flux, CLCC1. We found that depletion of CLCC1 causes gross hepatic steatosis in cells and in mice due to an abundance of lipid-rich particles trapped inside the ER lumen. Surprisingly, we discovered that CLCC1 is the homolog of yeast proteins Brl1p / Brr6p, long known to be involved in nuclear pore biogenesis and not thought to have mammalian counterparts. Using three-dimensional imaging and structural modeling, we predict that CLCC1 and Brl1p / Brr6p form oligomeric rings that interact across the ER or NE lumenal space and mediate membrane fusion, allowing for nuclear pore insertion and lipid droplets emergence into the cytosol.

Chapter 3 focuses on IL32, another novel regulator of neutral lipid storage identified from the genetic screens in Chapter 2. We found that IL32 only localizes to a subset of LDs in liver cells, stabilizing them during infection and inflammation. To better study these subsets of LDs, we developed a protocol to isolate populations of LDs that contain proteins of interest. Finally, Chapter 4 provides a protocol for designing, performing, and analyzing pooled CRISPR screens to answer complicated biological questions, such as the ones demonstrated in this work.

Collectively, this research offers a compendium of genes that regulate LDs across various metabolic conditions, and gives rich, mechanistic understanding of two—CLCC1 and IL32. It underscores the complex characteristics of the LD proteome and the intricate nature of lipid flux, emphasizing the value of investigative approaches like forward genetic screens in uncovering new biological insights.

References

1. Olzmann, J. A. & Carvalho, P. Dynamics and functions of lipid droplets. *Nat Rev Mol Cell Biol* **20**, 137–155 (2019).

2. Farese, R. V. & Walther, T. C. Glycerolipid synthesis and lipid droplet formation in the endoplasmic reticulum. *Cold Spring Harb. Perspect. Biol.* **15**, (2023).

3. Zadoorian, A., Du, X. & Yang, H. Lipid droplet biogenesis and functions in health and disease. *Nat. Rev. Endocrinol.* **19**, (2023).

4. Petan, T. Lipid droplets in cancer. Rev. Physiol. Biochem Pharm.185, 53–86 (2023).

5. Ralhan, I., Chang, C.-. L., Lippincott-Schwartz, J. & Ioannou, M. S. Lipid droplets in the nervous system. *J. Cell Biol.* **220**, (2021).

6. Bosch, M., Sweet, M. J., Parton, R. G. & Pol, A. Lipid droplets and the host–pathogen dynamic: FATal attraction? *J. Cell Biol.* **220**, (2021).

7. Papsdorf, K. Lipid droplets and peroxisomes are co-regulated to drive lifespan extension in response to mono-unsaturated fatty acids. *Nat. Cell Biol.* **25**, (2023).

8. Kumar, A. V. Lipid droplets modulate proteostasis, SQST-1/SQSTM1 dynamics, and lifespan in C. elegans. *iScience* **26**, (2023).

9. Roberts, M. A. & Olzmann, J. A. Protein Quality Control and Lipid Droplet Metabolism. *Annu Rev Cell Dev Biol* **36**, 115–139 (2020).

10. Dumesnil, C. Cholesterol esters form supercooled lipid droplets whose nucleation is facilitated by triacylglycerols. *Nat. Commun.* **14**, (2023).

11. Mahamid, J. Liquid-crystalline phase transitions in lipid droplets are related to cellular states and specific organelle association. *Proc. Natl Acad. Sci. USA* **116**, (2019).

12. Rogers, S. Triglyceride lipolysis triggers liquid crystalline phases in lipid droplets and alters the LD proteome. *J. Cell Biol.* **221**, (2022).

13. Henne, W. M. The (social) lives, deaths, and biophysical phases of lipid droplets. *Curr. Opin. Cell Biol.* **82**, (2023).

14. Sui, X. Structure and catalytic mechanism of a human triacylglycerol-synthesis enzyme. *Nature* **581**, (2020).

15. Wang, L. Structure and mechanism of human diacylglycerol O-acyltransferase 1. *Nature* **581**, (2020).

16. McLelland, G.-. L. Identification of an alternative triglyceride biosynthesis pathway. *Nature* **621**, (2023).

17. Thiam, A. R. & Ikonen, E. Lipid Droplet Nucleation. *Trends Cell Biol* **31**, 108–118 (2021).

18. Walther, T. C., Kim, S., Arlt, H., Voth, G. A. & Farese, R. V. Structure and function of lipid droplet assembly complexes. *Curr. Opin. Struct. Biol.* **80**, (2023).

19. Wang, H. Seipin is required for converting nascent to mature lipid droplets. *eLife* **5**, (2016).

20. Salo, V. T. Seipin facilitates triglyceride flow to lipid droplet and counteracts droplet ripening via endoplasmic reticulum contact. *Dev. Cell* **50**, (2019).

21. Sui, X. Cryo-electron microscopy structure of the lipid droplet-formation protein seipin. *J. Cell Biol.* **217**, (2018).

22. Yan, R. Human SEIPIN binds anionic phospholipids. *Dev. Cell* **47**, (2018).

23. Arlt, H. Seipin forms a flexible cage at lipid droplet formation sites. *Nat. Struct. Mol. Biol.* **29**, (2022).

24. Klug, Y. A. Mechanism of lipid droplet formation by the yeast Sei1/Ldb16 Seipin complex. *Nat. Commun.* **12**, (2021).

25. Kim, S. Seipin transmembrane segments critically function in triglyceride nucleation and lipid droplet budding from the membrane. *eLife* **11**, (2022).

26. Zoni, V. Seipin accumulates and traps diacylglycerols and triglycerides in its ring-like structure. *Proc. Natl Acad. Sci. USA* **118**, (2021).

27. Prasanna, X. Seipin traps triacylglycerols to facilitate their nanoscale clustering in the endoplasmic reticulum membrane. *PLoS Biol.* **19**, (2021).

28. Chorlay, A. Membrane asymmetry imposes directionality on lipid droplet emergence from the ER. *Dev. Cell* **50**, (2019).

29. M'barek, K. ER membrane phospholipids and surface tension control cellular lipid droplet formation. *Dev. Cell* **41**, (2017).

30. Jiang, X. Lack of VMP1 impairs hepatic lipoprotein secretion and promotes non-alcoholic steatohepatitis. *J. Hepatol.* **77**, (2022).

31. Li, Y. E. TMEM41B and VMP1 are scramblases and regulate the distribution of cholesterol and phosphatidylserine. *J. Cell Biol.* **220**, (2021).

32. Morishita, H. A critical role of VMP1 in lipoprotein secretion. *eLife* **8**, (2019).

33. Huang, D. TMEM41B acts as an ER scramblase required for lipoprotein biogenesis and lipid homeostasis. *Cell Metab.* **33**, (2021).

34. Mailler, E. The autophagy protein ATG9A enables lipid mobilization from lipid droplets. *Nat. Commun.* **12**, (2021).

35. Chung, J. LDAF1 and seipin form a lipid droplet assembly complex. *Dev. Cell* **51**, (2019).

36. Castro, I. G. Promethin is a conserved seipin partner protein. *Cells* **8**, (2019).

37. Joshi, A. S. Lipid droplet and peroxisome biogenesis occur at the same ER subdomains. *Nat. Commun.* **9**, (2018).

38. Joshi, A. S., Ragusa, J. V., Prinz, W. A. & Cohen, S. Multiple C2 domain-containing transmembrane proteins promote lipid droplet biogenesis and growth at specialized endoplasmic reticulum subdomains. *Mol Biol Cell* **32**, 1147–1157 (2021).

39. Ferreira, J. V. & Carvalho, P. Pex30-like proteins function as adaptors at distinct ER membrane contact sites. *J. Cell Biol.* **220**, (2021).

40. Santinho, A. Membrane curvature catalyzes lipid droplet assembly. *Curr. Biol.* **30**, (2020).

41. Renne, M. F., Corey, R. A., Ferreira, J. V., Stansfeld, P. J. & Carvalho, P. Seipin concentrates distinct neutral lipids via interactions with their acyl chain carboxyl esters. *J Cell Biol* **221**, e202112068 (2022).

42. Molenaar, M. R. Retinyl esters form lipid droplets independently of triacylglycerol and seipin. *J. Cell Biol.* **220**, (2021).

43. Sołtysik, K. Nuclear lipid droplets form in the inner nuclear membrane in a seipin-independent manner. *J. Cell Biol.* **220**, (2021).

44. Wang, L. Nonalcoholic fatty liver disease experiences accumulation of hepatic liquid crystal associated with increasing lipophagy. *Cell Biosci.* **10**, (2020).

45. Chen, F., Yin, Y., Chua, B. T. & Li, P. CIDE family proteins control lipid homeostasis and the development of metabolic diseases. *Traffic* **21**, (2020).

46. Lyu, X. A gel-like condensation of Cidec generates lipid-permeable plates for lipid droplet fusion. *Dev. Cell* **56**, (2021).

47. Qian, K. CLSTN3β enforces adipocyte multilocularity to facilitate lipid utilization. *Nature* **613**, (2023).

48. Olarte, M.-. J. Determinants of endoplasmic reticulum-to-lipid droplet protein targeting. *Dev. Cell* **54**, (2020).

49. Wilfling, F. Triacylglycerol synthesis enzymes mediate lipid droplet growth by relocalizing from the ER to lipid droplets. *Dev. Cell* **24**, (2013).

50. Song, J. Identification of two pathways mediating protein targeting from ER to lipid droplets. *Nat. Cell Biol.* **24**, (2022).

51. Schrul, B. & Kopito, R. R. Peroxin-dependent targeting of a lipid-droplet-destined membrane protein to ER subdomains. *Nat. Cell Biol.* **18**, (2016).

52. Olzmann, J. A., Richter, C. M. & Kopito, R. R. Spatial regulation of UBXD8 and p97/VCP controls ATGL-mediated lipid droplet turnover. *Proc. Natl Acad. Sci. USA* **110**, (2013).

53. Boeszoermenyi, A. Structure of a CGI-58 motif provides the molecular basis of lipid droplet anchoring. *J. Biol. Chem.* **290**, (2015).

54. Prévost, C. *et al.* Mechanism and Determinants of Amphipathic Helix-Containing Protein Targeting to Lipid Droplets. *Dev Cell* **44**, 73-86.e4 (2018).

55. Chorlay, A. & Thiam, A. R. Neutral lipids regulate amphipathic helix affinity for model lipid droplets. *J Cell Biol* **219**, e201907099 (2020).

56. Wolins, N. E., Brasaemle, D. L. & Bickel, P. E. A proposed model of fat packaging by exchangeable lipid droplet proteins. *FEBS Lett.* **580**, (2006).

57. Kim, S., Swanson, J. M. J. & Voth, G. A. Computational studies of lipid droplets. *J. Phys. Chem. B* **126**, (2022).

58. Schott, M. B., Rozeveld, C. N., Weller, S. G. & McNiven, M. A. Lipophagy at a glance. *J. Cell Sci.* **135**, (2022).

59. Grabner, G. F., Xie, H., Schweiger, M. & Zechner, R. Lipolysis: cellular mechanisms for lipid mobilization from fat stores. *Nat. Metab.* **3**, (2021).

60. Soni, K. G. Coatomer-dependent protein delivery to lipid droplets. *J. Cell Sci.* **122**, (2009).

61. Wilfling, F. Arf1/COPI machinery acts directly on lipid droplets and enables their connection to the ER for protein targeting. *eLife* **3**, (2014).

62. Beller, M. COPI complex is a regulator of lipid homeostasis. *PLoS Biol.* **6**, (2008).

63. Zechner, R., Madeo, F. & Kratky, D. Cytosolic lipolysis and lipophagy: two sides of the same coin. *Nat. Rev. Mol. Cell Biol.* **18**, (2017).

64. Lass, A. Adipose triglyceride lipase-mediated lipolysis of cellular fat stores is activated by CGI-58 and defective in Chanarin-Dorfman Syndrome. *Cell Metab.* **3**, (2006).

65. Kimmel, A. R. & Sztalryd, C. The perilipins: major cytosolic lipid droplet-associated proteins and their roles in cellular lipid storage, mobilization, and systemic homeostasis. *Annu. Rev. Nutr.* **36**, (2016).

66. Granneman, J. G., Moore, H.-. P. H., Mottillo, E. P., Zhu, Z. & Zhou, L. Interactions of perilipin-5 (Plin5) with adipose triglyceride lipase. *J. Biol. Chem.* **286**, (2011).

67. Wang, Y., Kory, N., BasuRay, S., Cohen, J. C. & Hobbs, H. H. PNPLA3, CGI-58, and inhibition of hepatic triglyceride hydrolysis in mice. *Hepatology* **69**, (2019).

68. Yang, A., Mottillo, E. P., Mladenovic-Lucas, L., Zhou, L. & Granneman, J. G. Dynamic interactions of ABHD5 with PNPLA3 regulate triacylglycerol metabolism in brown adipocytes. *Nat. Metab.* **1**, (2019).

69. Sanders, M. A. Endogenous and synthetic ABHD5 ligands regulate ABHD5-perilipin interactions and lipolysis in fat and muscle. *Cell Metab.* **22**, (2015).

70. Yang, X. The G0/G1 switch gene 2 regulates adipose lipolysis through association with adipose triglyceride lipase. *Cell Metab.* **11**, (2010).

71. DiStefano, M. T. The lipid droplet protein hypoxia-inducible gene 2 promotes hepatic triglyceride deposition by inhibiting lipolysis. *J. Biol. Chem.* **290**, (2015).

72. Tseng, Y. Y. Structural and functional insights into ABHD5, a ligand-regulated lipase co-activator. *Sci. Rep.* **12**, (2022).

73. Kulminskaya, N. et al. Unmasking crucial residues in adipose triglyceride lipase for coactivation with comparative gene identification-58. J. Lipid. Res.65, 100491 (2024).

74. Kohlmayr, J. M. et al. Mutational scanning pinpoints distinct binding sites of key ATGL regulators in lipolysis. Preprint at bioRxivhttps://doi.org/10.1101/2023.05.10.540188 (2023).

75. Mayer, N. Development of small-molecule inhibitors targeting adipose triglyceride lipase. *Nat. Chem. Biol.* **9**, (2013).

76. Wunderling, K., Zurkovic, J., Zink, F., Kuerschner, L. & Thiele, C. Triglyceride cycling enables modification of stored fatty acids. *Nat Metab* **5**, 699–709 (2023).

77. Sharma, A. K. & Wolfrum, C. Lipid cycling isn't all futile. *Nat. Metab.* **5**, (2023).

78. Patel, R. ATGL is a biosynthetic enzyme for fatty acid esters of hydroxy fatty acids. *Nature* **606**, (2022).

79. Yore, M. M. Discovery of a class of endogenous mammalian lipids with anti-diabetic and anti-inflammatory effects. *Cell* **159**, (2014).

80. Dierge, E. Peroxidation of n-3 and n-6 polyunsaturated fatty acids in the acidic tumor environment leads to ferroptosis-mediated anticancer effects. *Cell Metab.* **33**, (2021).

81. Schott, M. B. Lipid droplet size directs lipolysis and lipophagy catabolism in hepatocytes. *J. Cell Biol.* **218**, (2019).

82. Chung, J. The Troyer syndrome protein spartin mediates selective autophagy of lipid droplets. *Nat. Cell Biol.* **25**, (2023).

83. Omrane, M. LC3B is lipidated to large lipid droplets during prolonged starvation for noncanonical autophagy. *Dev. Cell* **58**, (2023).

84. Schulze, R. J. et al. Direct lysosome-based autophagy of lipid droplets in hepatocytes. Proc. Natl Acad. Sci. USA117, 32443–32452 (2020).

85. Menon, D. ARL8B mediates lipid droplet contact and delivery to lysosomes for lipid remobilization. *Cell Rep.* **42**, (2023).

86. Herker, E., Vieyres, G., Beller, M., Krahmer, N. & Bohnert, M. Lipid Droplet Contact Sites in Health and Disease. *Trends Cell Biol* **31**, 345–358 (2021).

87. Prinz, W. A., Toulmay, A. & Balla, T. The functional universe of membrane contact sites. *Nat Rev Mol Cell Biol* **21**, 7–24 (2020).

88. Hanna, M., Guillén-Samander, A. & Camilli, P. RBG motif bridge-like lipid transport proteins: structure, functions, and open questions. *Annu. Rev. Cell Dev. Biol.* **39**, (2023).

89. Wong, L. H., Gatta, A. T. & Levine, T. P. Lipid transfer proteins: the lipid commute via shuttles, bridges and tubes. *Nat Rev Mol Cell Biol* **20**, 85–101 (2019).

90. Du, X. ORP5 localizes to ER-lipid droplet contacts and regulates the level of PI(4)P on lipid droplets. *J. Cell Biol.* **219**, (2020).

91. Guyard, V. ORP5 and ORP8 orchestrate lipid droplet biogenesis and maintenance at ER–mitochondria contact sites. *J. Cell Biol.* **221**, (2022).

92. Olkkonen, V. M., Koponen, A. & Arora, A. OSBP-related protein 2 (ORP2): unraveling its functions in cellular lipid/carbohydrate metabolism, signaling and F-actin regulation. *J. Steroid Biochem. Mol. Biol.* **192**, (2019).

93. Wang, T. OSBPL2 is required for the binding of COPB1 to ATGL and the regulation of lipid droplet lipolysis. *iScience* **23**, (2020).

94. Velikkakath, A. K. G., Nishimura, T., Oita, E., Ishihara, N. & Mizushima, N. Mammalian Atg2 proteins are essential for autophagosome formation and important for regulation of size and distribution of lipid droplets. *Mol. Biol. Cell* **23**, (2012).

95. Korfhage, J. L. et al. ATG2A-mediated bridge-like lipid transport regulates lipid droplet accumulation. Preprint at bioRxivhttps://doi.org/10.1101/2023.08.14.553257 (2023).

96. Bersuker, K. A proximity labeling strategy provides insights into the composition and dynamics of lipid droplet proteomes. *Dev. Cell* **44**, (2018).

97. Yeshaw, W. M. Human VPS13A is associated with multiple organelles and influences mitochondrial morphology and lipid droplet motility. *eLife* **8**, (2019).

98. Kumar, N. VPS13A and VPS13C are lipid transport proteins differentially localized at ER contact sites. *J. Cell Biol.* **217**, (2018).

99. Chen, S. VPS13A and VPS13C influence lipid droplet abundance. *Contact* **5**, (2022).

100. Ghanbarpour, A., Valverde, D. P., Melia, T. J. & Reinisch, K. M. A model for a partnership of lipid transfer proteins and scramblases in membrane expansion and organelle biogenesis. *Proc. Natl Acad. Sci. USA* **118**, (2021).

101. Vliet, A. R. ATG9A and ATG2A form a heteromeric complex essential for autophagosome formation. *Mol. Cell* **82**, (2022).

102. Matoba, K. Atg9 is a lipid scramblase that mediates autophagosomal membrane expansion. *Nat. Struct. Mol. Biol.* **27**, (2020).

103. Wang, H. Perilipin 5, a lipid droplet-associated protein, provides physical and metabolic linkage to mitochondria. *J. Lipid Res.* **52**, (2011).

104. Miner, G. E. PLIN5 interacts with FATP4 at membrane contact sites to promote lipid droplet-to-mitochondria fatty acid transport. *Dev. Cell* **58**, (2023).

105. Hariri, H. Mdm1 maintains endoplasmic reticulum homeostasis by spatially regulating lipid droplet biogenesis. *J. Cell Biol.* **218**, (2019).

106. Ouyang, Q. Rab8a as a mitochondrial receptor for lipid droplets in skeletal muscle. *Dev. Cell* **58**, (2023).

107. Najt, C. P. Lipid droplet-derived monounsaturated fatty acids traffic via PLIN5 to allosterically activate SIRT1. *Mol. Cell* **77**, (2020).

108. Nguyen, T. B. DGAT1-dependent lipid droplet biogenesis protects mitochondrial function during starvation-induced autophagy. *Dev. Cell* **42**, (2017).

109. Rambold, A. S., Cohen, S. & Lippincott-Schwartz, J. Fatty acid trafficking in starved cells: regulation by lipid droplet lipolysis, autophagy, and mitochondrial fusion dynamics. *Dev Cell* **32**, 678–692 (2015).

110. Benador, I. Y. Mitochondria bound to lipid droplets have unique bioenergetics, composition, and dynamics that support lipid droplet expansion. *Cell Metab.* **27**, (2018).

111. Freyre, C. A. C., Rauher, P. C., Ejsing, C. S. & Klemm, R. W. MIGA2 links mitochondria, the ER, and lipid droplets and promotes de novo lipogenesis in adipocytes. *Mol. Cell* **76**, (2019).

112. Najt, C. P. Organelle interactions compartmentalize hepatic fatty acid trafficking and metabolism. *Cell Rep.* **42**, (2023).

113. Gallardo-Montejano, V. I. Perilipin 5 links mitochondrial uncoupled respiration in brown fat to healthy white fat remodeling and systemic glucose tolerance. *Nat. Commun.* **12**, (2021).

114. Gallardo-Montejano, V. I. Nuclear perilipin 5 integrates lipid droplet lipolysis with PGC-1α/SIRT1-dependent transcriptional regulation of mitochondrial function. *Nat. Commun.* **7**, (2016).

115. Hong, Z. Mitoguardin-2–mediated lipid transfer preserves mitochondrial morphology and lipid droplet formation. *J. Cell Biol.* **221**, (2022).

116. Kim, H., Lee, S., Jun, Y. & Lee, C. Structural basis for mitoguardin-2 mediated lipid transport at ER-mitochondrial membrane contact sites. *Nat. Commun.* **13**, (2022).

117. Listenberger, L. L., Ory, D. S. & Schaffer, J. E. Palmitate-induced apoptosis can occur through a ceramide-independent pathway. *J. Biol. Chem.* **276**, (2001).

118. Zhu, X. G. CHP1 regulates compartmentalized glycerolipid synthesis by activating GPAT4. *Mol. Cell* **74**, (2019).

119. Piccolis, M. Probing the global cellular responses to lipotoxicity caused by saturated fatty acids. *Mol. Cell* **74**, (2019).

120. Masuda, M. Saturated phosphatidic acids mediate saturated fatty acid–induced vascular calcification and lipotoxicity. *J. Clin. Invest.* **125**, (2015).

121. Volmer, R., Ploeg, K. & Ron, D. Membrane lipid saturation activates endoplasmic reticulum unfolded protein response transducers through their transmembrane domains. *Proc. Natl Acad. Sci. USA* **110**, (2013).

122. Halbleib, K. Activation of the unfolded protein response by lipid bilayer stress. *Mol. Cell* **67**, (2017).

123. Chitraju, C. Triglyceride synthesis by DGAT1 protects adipocytes from lipid-induced ER stress during lipolysis. *Cell Metab.* **26**, (2017).

124. Otten, E. G. Ubiquitylation of lipopolysaccharide by RNF213 during bacterial infection. *Nature* **594**, (2021).

125. Sugihara, M. The AAA+ ATPase/ubiquitin ligase mysterin stabilizes cytoplasmic lipid droplets. *J. Cell Biol.* **218**, (2019).

126. Senkal, C. E. Ceramide is metabolized to acylceramide and stored in lipid droplets. *Cell Metab.* **25**, (2017).

127. Jiang, X., Stockwell, B. R. & Conrad, M. Ferroptosis: mechanisms, biology and role in disease. *Nat. Rev. Mol. Cell Biol.* **22**, (2021).

128. Li, Z., Lange, M., Dixon, S. J. & Olzmann, J. A. Lipid quality control and ferroptosis: from concept to mechanism. *Annu. Rev. Biochem.* (2024) doi:10.1146/annurev-biochem-052521-033527.

129. Yang, W. S. Regulation of ferroptotic cancer cell death by GPX4. *Cell* **156**, (2014).

130. Bersuker, K. The CoQ oxidoreductase FSP1 acts parallel to GPX4 to inhibit ferroptosis. *Nature* **575**, (2019).

131. Doll, S. FSP1 is a glutathione-independent ferroptosis suppressor. *Nature* **575**, (2019).

132. Mishima, E. A non-canonical vitamin K cycle is a potent ferroptosis suppressor. *Nature* **608**, (2022).

133. Jin, D.-. Y. A genome-wide CRISPR-Cas9 knockout screen identifies FSP1 as the warfarin-resistant vitamin K reductase. *Nat. Commun.* **14**, (2023).

134. Danielli, M., Perne, L., Jarc Jovičić, E. & Petan, T. Lipid droplets and polyunsaturated fatty acid trafficking: balancing life and death. *Front. Cell Dev. Biol.* **11**, (2023).

135. Doll, S. ACSL4 dictates ferroptosis sensitivity by shaping cellular lipid composition. *Nat. Chem. Biol.* **13**, (2017).

136. Magtanong, L. Exogenous monounsaturated fatty acids promote a ferroptosis-resistant cell state. *Cell Chem. Biol.* **26**, (2019).

137. Ioannou, M. S. Neuron-astrocyte metabolic coupling protects against activity-induced fatty acid toxicity. *Cell* **177**, (2019).

138. Minami, J. K. CDKN2A deletion remodels lipid metabolism to prime glioblastoma for ferroptosis. *Cancer Cell* **41**, (2023).

139. Bailey, A. P. Antioxidant role for lipid droplets in a stem cell niche of drosophila. *Cell* **163**, (2015).

140. Ralhan, I. Autolysosomal exocytosis of lipids protect neurons from ferroptosis. *J. Cell Biol.* **222**, (2023).

141. Mohammadyani, D. Molecular speciation and dynamics of oxidized triacylglycerols in lipid droplets: mass spectrometry and coarse-grained simulations. *Free Radic. Biol. Med* **76**, (2014).

142. Ferrada, L., Barahona, M. J., Vera, M., Stockwell, B. R. & Nualart, F. Dehydroascorbic acid sensitizes cancer cells to system xc− inhibition-induced ferroptosis by promoting lipid droplet peroxidation. Cell Death Dis.14, 637 (2023).

143. Zou, Y. A GPX4-dependent cancer cell state underlies the clear-cell morphology and confers sensitivity to ferroptosis. *Nat. Commun.* **10**, (2019).

144. Roberts, M. A. Parallel CRISPR-Cas9 screens identify mechanisms of PLIN2 and lipid droplet regulation. *Dev. Cell* **58**, (2023).

145. Mathiowetz, A. J. *et al.* CLCC1 promotes hepatic neutral lipid flux and nuclear pore complex assembly. *bioRxiv* 2024.06.07.597858 (2024) doi:10.1101/2024.06.07.597858.

146. Mejhert, N. The Lipid Droplet Knowledge Portal: a resource for systematic analyses of lipid droplet biology. *Dev. Cell* **57**, (2022).

147. Mathiowetz, A. J. & Olzmann, J. A. Lipid droplets and cellular lipid flux. *Nat Cell Biol* **26**, 331–345 (2024).

148. Schulze, R. J., Schott, M. B., Casey, C. A., Tuma, P. L. & McNiven, M. A. The cell biology of the hepatocyte: A membrane trafficking machine. *Journal of Cell Biology* **218**, 2096–2112 (2019).

149. Van Zwol, W., Van De Sluis, B., Ginsberg, H. N. & Kuivenhoven, J. A. VLDL Biogenesis and Secretion: It Takes a Village. *Circulation Research* **134**, 226–244 (2024).

150. Gluchowski, N. L., Becuwe, M., Walther, T. C. & Farese, R. V. Lipid droplets and liver disease: from basic biology to clinical implications. *Nat Rev Gastroenterol Hepatol* **14**, 343–355 (2017).

151. Dultz, E., Wojtynek, M., Medalia, O. & Onischenko, E. The Nuclear Pore Complex: Birth, Life, and Death of a Cellular Behemoth. *Cells* **11**, 1456 (2022).

152. Hodge, C. A. *et al.* Integral membrane proteins Brr6 and Apq12 link assembly of the nuclear pore complex to lipid homeostasis in the endoplasmic reticulum. *Journal of Cell Science* **123**, 141–151 (2010).

153. Lone, M. A. *et al.* Yeast Integral Membrane Proteins Apq12, Brl1, and Brr6 Form a Complex Important for Regulation of Membrane Homeostasis and Nuclear Pore Complex Biogenesis. *Eukaryot Cell* **14**, 1217–1227 (2015).

154. Zhang, W. *et al.* Brr6 and Brl1 locate to nuclear pore complex assembly sites to promote their biogenesis. *Journal of Cell Biology* **217**, 877–894 (2018).

155. Vitale, J., Khan, A., Neuner, A. & Schiebel, E. A perinuclear α-helix with amphipathic features in Brl1 promotes NPC assembly. *MBoC* **33**, ar35 (2022).

156. Kralt, A. *et al.* An amphipathic helix in Brl1 is required for nuclear pore complex biogenesis in S. cerevisiae. *eLife* **11**, e78385 (2022).

157. Li, L. *et al.* Mutation in the intracellular chloride channel CLCC1 associated with autosomal recessive retinitis pigmentosa. *PLoS Genet* **14**, e1007504 (2018).

158. Jia, Y., Jucius, T. J., Cook, S. A. & Ackerman, S. L. Loss of *Clcc1* Results in ER Stress, Misfolded Protein Accumulation, and Neurodegeneration. *J. Neurosci.* **35**, 3001–3009 (2015).

159. Guo, L. *et al.* Disruption of ER ion homeostasis maintained by an ER anion channel CLCC1 contributes to ALS-like pathologies. *Cell Res* **33**, 497–515 (2023).

160. Xu, S. *et al.* Perilipin 2 and lipid droplets provide reciprocal stabilization. *Biophys Rep* **5**, 145–160 (2019).

161. Najt, C. P., Devarajan, M. & Mashek, D. G. Perilipins at a glance. *Journal of Cell Science* **135**, jcs259501 (2022).

162. Nguyen, K. T. *et al.* N-terminal acetylation and the N-end rule pathway control degradation of the lipid droplet protein PLIN2. *Journal of Biological Chemistry* **294**, 379–388 (2019).

163. Xu, G. *et al.* Post-translational Regulation of Adipose Differentiation-related Protein by the Ubiquitin/Proteasome Pathway. *Journal of Biological Chemistry* **280**, 42841–42847 (2005).

164. Schmid, E. M. *et al.* Size-dependent protein segregation at membrane interfaces. *Nature Phys* **12**, 704–711 (2016).

165. Parlakgül, G. *et al.* Regulation of liver subcellular architecture controls metabolic homeostasis. *Nature* **603**, 736–742 (2022).

166. Fu, S. *et al.* Phenotypic assays identify azoramide as a small-molecule modulator of the unfolded protein response with antidiabetic activity. *Sci. Transl. Med.* **7**, (2015).

167. Nagasawa, M., Kanzaki, M., Iino, Y., Morishita, Y. & Kojima, I. Identification of a Novel Chloride Channel Expressed in the Endoplasmic Reticulum, Golgi Apparatus, and Nucleus. *Journal of Biological Chemistry* **276**, 20413–20418 (2001).

168. Lin, D. H. & Hoelz, A. The Structure of the Nuclear Pore Complex (An Update). *Annu. Rev. Biochem.* **88**, 725–783 (2019).

169. Shin, J.-Y. *et al.* Nuclear envelope–localized torsinA-LAP1 complex regulates hepatic VLDL secretion and steatosis. *Journal of Clinical Investigation* **129**, 4885–4900 (2019).

170. Hernandez-Ono, A. *et al.* Dynamic regulation of hepatic lipid metabolism by torsinA and its activators. *JCI Insight* (2024) doi:10.1172/jci.insight.175328.

171. Amici, D. R. *et al.* FIREWORKS: a bottom-up approach to integrative coessentiality network analysis. *Life Sci. Alliance* **4**, e202000882 (2021).

172. Hein, M. Y. *et al.* Global organelle profiling reveals subcellular localization and remodeling at proteome scale. Preprint at https://doi.org/10.1101/2023.12.18.572249 (2023).

173. Schweke, H. *et al.* An atlas of protein homo-oligomerization across domains of life. *Cell* **187**, 999-1010.e15 (2024).

174. Saitoh, Y., Ogawa, K. & Nishimoto, T. Brl1p – A Novel Nuclear Envelope Protein Required for Nuclear Transport. *Traffic* **6**, 502–517 (2005).

175. Humphreys, I. R. *et al.* Computed structures of core eukaryotic protein complexes. *Science* **374**, eabm4805 (2021).

176. Greenberg, A. S. *et al.* The role of lipid droplets in metabolic disease in rodents and humans. *J. Clin. Invest.* **121**, 2102–2110 (2011).

177. Xu, S., Zhang, X. & Liu, P. Lipid droplet proteins and metabolic diseases. *Biochimica et Biophysica Acta (BBA) - Molecular Basis of Disease* **1864**, 1968–1983 (2018).

178. Listenberger, L. L. Triglyceride accumulation protects against fatty acid-induced lipotoxicity. *Proc. Natl Acad. Sci. USA* **100**, (2003).

179. Vieyres, G. & Pietschmann, T. HCV Pit Stop at the Lipid Droplet: Refuel Lipids and Put on a Lipoprotein Coat before Exit. *Cells* **8**, 233 (2019).

180. Meyers, N. L., Fontaine, K. A., Kumar, G. R. & Ott, M. Entangled in a membranous web: ER and lipid droplet reorganization during hepatitis C virus infection. *Current Opinion in Cell Biology* **41**, 117–124 (2016).

181. Herker, E. *et al.* Efficient hepatitis C virus particle formation requires diacylglycerol acyltransferase-1. *Nat Med* **16**, 1295–1298 (2010).

182. Dias, S. S. G. *et al.* Lipid droplets fuel SARS-CoV-2 replication and production of inflammatory mediators. *PLoS Pathog* **16**, e1009127 (2020).

183. Knight, M., Braverman, J., Asfaha, K., Gronert, K. & Stanley, S. Lipid droplet formation in Mycobacterium tuberculosis infected macrophages requires IFN-γ/HIF-1α signaling and supports host defense. *PLoS Pathog* **14**, e1006874 (2018).

184. Bosch, M. *et al.* Mammalian lipid droplets are innate immune hubs integrating cell metabolism and host defense. *Science* **370**, eaay8085 (2020).

185. Greenwood, D. J. *et al.* Subcellular antibiotic visualization reveals a dynamic drug reservoir in infected macrophages. *Science* **364**, 1279–1282 (2019).

186. Dali-Youcef, N. *et al.* Interleukin-32 Contributes to Human Nonalcoholic Fatty Liver Disease and Insulin Resistance. *Hepatol Commun* **3**, 1205–1220 (2019).

187. Sasidharan, K. *et al.* IL32 downregulation lowers triglycerides and type I collagen in di-lineage human primary liver organoids. *Cell Reports Medicine* **5**, 101352 (2024).

188. Cermelli, S., Guo, Y., Gross, S. P. & Welte, M. A. The Lipid-Droplet Proteome Reveals that Droplets Are a Protein-Storage Depot. *Current Biology* **16**, 1783–1795 (2006).

189. Mejhert, N. *et al.* Partitioning of MLX-Family Transcription Factors to Lipid Droplets Regulates Metabolic Gene Expression. *Molecular Cell* **77**, 1251-1264.e9 (2020).

190. Hasegawa, H., Thomas, H. J., Schooley, K. & Born, T. L. Native IL-32 is released from intestinal epithelial cells via a non-classical secretory pathway as a membrane-associated protein. *Cytokine* **53**, 74–83 (2011).

191. Krahmer, N., Farese, R. V. & Walther, T. C. Balancing the fat: lipid droplets and human disease. *EMBO Mol Med* **5**, 973–983 (2013).

192. Magré, J. *et al.* Identification of the gene altered in Berardinelli-Seip congenital lipodystrophy on chromosome 11q13. *Nat Genet* **28**, 365–370 (2001).

193. Baselli, G. A. *et al.* Liver transcriptomics highlights interleukin-32 as novel NAFLD-related cytokine and candidate biomarker. *Gut* **69**, 1855–1866 (2020).

194. Khor, V. K. *et al.* The Proteome of Cholesteryl-Ester-Enriched Versus Triacylglycerol-Enriched Lipid Droplets. *PLoS ONE* **9**, e105047 (2014).

195. Hayashi, H., Kubo, Y., Izumida, M. & Matsuyama, T. Efficient viral delivery of Cas9 into human safe harbor. *Sci Rep* **10**, 21474 (2020).

196. Li, Z. *et al.* Ribosome stalling during selenoprotein translation exposes a ferroptosis vulnerability. *Nat Chem Biol* **18**, 751–761 (2022).

197. Nagy, T. & Kampmann, M. CRISPulator: a discrete simulation tool for pooled genetic screens. *BMC Bioinformatics* **18**, 347 (2017).

198. Iyer, V. S. *et al.* Designing custom CRISPR libraries for hypothesis-driven drug target discovery. *Comput Struct Biotechnol J* **18**, 2237–2246 (2020).

199. Morgens, D. W. *et al.* Genome-scale measurement of off-target activity using Cas9 toxicity in high-throughput screens. *Nat Commun* **8**, 15178 (2017).

200. Leto, D. E. *et al.* Genome-wide CRISPR Analysis Identifies Substrate-Specific Conjugation Modules in ER-Associated Degradation. *Mol Cell* **73**, 377-389.e11 (2019).

201. Li, W. *et al.* MAGeCK enables robust identification of essential genes from genome-scale CRISPR/Cas9 knockout screens. *Genome Biol* **15**, 554 (2014).

202. Wang, B. *et al.* Integrative analysis of pooled CRISPR genetic screens using MAGeCKFlute. *Nat Protoc* **14**, 756–780 (2019).

203. Tian, R. *et al.* Genome-wide CRISPRi/a screens in human neurons link lysosomal failure to ferroptosis. *Nat Neurosci* **24**, 1020–1034 (2021).

204. Diaz, A. A., Qin, H., Ramalho-Santos, M. & Song, J. S. HiTSelect: a comprehensive tool for high-complexity-pooled screen analysis. *Nucleic Acids Research* **43**, e16–e16 (2015).

205. Anders, S. & Huber, W. Differential expression analysis for sequence count data. *Genome Biol* **11**, R106 (2010).

206. Luo, B. *et al.* Highly parallel identification of essential genes in cancer cells. *Proc. Natl. Acad. Sci. U.S.A.* **105**, 20380–20385 (2008).

207. Morgens, D. W., Deans, R. M., Li, A. & Bassik, M. C. Systematic comparison of CRISPR/Cas9 and RNAi screens for essential genes. *Nat Biotechnol* **34**, 634–636 (2016).

208. Bock, C. *et al.* High-content CRISPR screening. *Nat Rev Methods Primers* **2**, 8 (2022).

209. Sheel, A. & Xue, W. Genomic Amplifications Cause False Positives in CRISPR Screens. *Cancer Discov* **6**, 824–826 (2016).

210. Krshnan, L. *et al.* Regulated degradation of the inner nuclear membrane protein SUN2 maintains nuclear envelope architecture and function. *Elife* **11**, e81573 (2022).

211. Rossi, A. *et al.* Genetic compensation induced by deleterious mutations but not gene knockdowns. *Nature* **524**, 230–233 (2015).

212. Cui, X. *et al.* Seipin ablation in mice results in severe generalized lipodystrophy. *Human Molecular Genetics* **20**, 3022–3030 (2011).

213. Thierer, J. H. *et al.* Pla2g12b drives expansion of triglyceride-rich lipoproteins. *Nat Commun* **15**, 2095 (2024).

214. Wu, L. *et al.* CLCC1 Governs Bilayer Equilibration at the Endoplasmic Reticulum to Maintain Cellular and Systemic Lipid Homeostasis. Preprint at https://doi.org/10.1101/2024.06.07.596575 (2024).

215. Arruda, A. P. & Parlakgül, G. Endoplasmic Reticulum Architecture and Inter-Organelle Communication in Metabolic Health and Disease. *Cold Spring Harb Perspect Biol* **15**, a041261 (2023).

216. Talari, N. K. *et al.* Lipid-droplet associated mitochondria promote fatty-acid oxidation through a distinct bioenergetic pattern in male Wistar rats. *Nat Commun* **14**, 766 (2023).

217. Yu, Y. *et al.* Organelle proteomic profiling reveals lysosomal heterogeneity in association with longevity. *eLife* **13**, e85214 (2024).

218. Thiam, A. R. & Beller, M. The why, when and how of lipid droplet diversity. *J Cell Sci* **130**, 315–324 (2017).

219. Ventura, A. E. *et al.* Cell lipid droplet heterogeneity and altered biophysical properties induced by cell stress and metabolic imbalance. *Biochimica et Biophysica Acta (BBA) - Molecular and Cell Biology of Lipids* **1868**, 159347 (2023).

220. Majchrzak, M. *et al.* Perilipin membrane integration determines lipid droplet heterogeneity in differentiating adipocytes. *Cell Reports* **43**, 114093 (2024).

221. Abu-Remaileh, M. *et al.* Lysosomal metabolomics reveals V-ATPase- and mTOR-dependent regulation of amino acid efflux from lysosomes. *Science* **358**, 807–813 (2017).

222. Rampello, A. J., Prophet, S. M. & Schlieker, C. The Role of Torsin AAA+ Proteins in Preserving Nuclear Envelope Integrity and Safeguarding Against Disease. *Biomolecules* **10**, 468 (2020).

223. Peng, Y., Tang, Q., Xiao, F. & Fu, N. Regulation of Lipid Metabolism by Lamin in Mutation-Related Diseases. *Front. Pharmacol.* **13**, 820857 (2022).

224. Östlund, C., Hernandez-Ono, A. & Shin, J.-Y. The Nuclear Envelope in Lipid Metabolism and Pathogenesis of NAFLD. *Biology* **9**, 338 (2020).

225. Evans, D. E., Shvedunova, M. & Graumann, K. The nuclear envelope in the plant cell cycle: structure, function and regulation. *Annals of Botany* **107**, 1111–1118 (2011).

226. Saur, M. *et al.* A Janus-Faced IM30 Ring Involved in Thylakoid Membrane Fusion Is Assembled from IM30 Tetramers. *Structure* **25**, 1380-1390.e5 (2017).

227. He, Q.-J. *et al.* Recent advances in age-related metabolic dysfunction-associated steatotic liver disease. *World J Gastroenterol* **30**, 652–662 (2024).

228. Kneeman, J. M., Misdraji, J. & Corey, K. E. Secondary causes of nonalcoholic fatty liver disease. *Therap Adv Gastroenterol* **5**, 199–207 (2012).

229. Coleman, R. A. The “discovery” of lipid droplets: A brief history of organelles hidden in plain sight. *Biochimica et Biophysica Acta (BBA) - Molecular and Cell Biology of Lipids* **1865**, 158762 (2020).